Growth and Characterisation of Site-Controlled InAs/InP Quantum Dots by Droplet Epitaxy in MOVPE

Young In Na

A thesis submitted in partial fulfilment of the requirements for the degree of
Doctor of Philosophy

The University of Sheffield

Faculty of Engineering

Department of Electronic and Electrical Engineering

November 2021

Abstract

InAs/InP quantum dots were grown by droplet epitaxy via metal-organic vapor phase epitaxy (MOVPE). Their structural and optical properties on a planar substrate were extensively investigated. Indium droplets were formed through pyrolysis of trimethylindium and by controlling parameters such as deposition temperature, flow rate and growth interrupt, the density and size of droplets could be manipulated to form optically active quantum dots (QDs) in the 1550nm telecom emission band. After optimising the conditions for QD formation on planar substrates, site-control of the QDs was investigated. The major emphasis of this work and its findings is the deterministic positioning of QDs through the precursor process of positioning of indium droplets within ex-situ fabricated nanohole arrays. Using electron beam lithography and dry etching, nanohole arrays were fabricated, which served as favourable nucleation sites for droplets and subsequently QDs through the process of arsenic crystallisation. Following nanohole fabrication, extensive optimisation of the surface cleaning procedure and buffer growth were developed to reduce impurity levels and obtain high quality QDs. The spatial arrangement of droplets deviates from randomness when the patterned substrate is employed as a template for growth. This is a new method to site-control QDs by deterministic positioning of droplets in droplet epitaxy.

Acknowledgements

First and foremost, I'd like to thank the University of Sheffield for funding my project. I am very grateful to my supervisor, Professor. Jon Heffernan, for giving me the opportunity to work in his research group. His knowledge, understanding, gracious guidance and support made it possible for me to work throughout my PhD. I would also like to thank my second supervisor Dr. Ian Farrer for all his advice and encouragement.

I have been very lucky to work with many amazing and wonderful people in our research group. This thesis becomes a reality thanks to the generous support and assistance of many individuals. I would like to express my sincere gratitude to each and every one of them. Dr Elisa M. Sala deserves special recognition for growing all the samples; without her, none of this work would have been possible. Thank you very much to Dr. Charlotte Ovenden for all of your help and advice in every aspect over the years. Thank you to Dr. Nasser Babazadeh for sharing his time and assisting me with fabrication processes. Thank you also to Dr. Aristotelis Trapalis and Max Godsland for the µPL measurements.

I would like to thank my mom and brother. Thank you for always being there for me through thick and thin. Without you, none of this would have been possible. Thank you for always supporting me.

Finally, I thank GOD for his Almighty who gives me strength and allows this to happen.

List of Publications

Associated publication

E. M. Sala, <u>**Y. I. Na**</u>, M. Godsland, A. Trapalis, and J. Heffernan, "InAs/InP Quantum Dots in Etched Pits by Droplet Epitaxy in Metalorganic Vapor Phase Epitaxy," *Phys. Status Solidi - Rapid Res. Lett.*, vol. 14, no. 8, Aug. 2020, doi: 10.1002/pssr.202000173.

Paper in progress

E. M. Sala, M. Godsland, <u>**Y. I. Na,**</u> A. Trapalis, and J. Heffernan, "Droplet Epitaxy of InAs/InP Quantum Dots via MOVPE by using an InGaAs interlayer," accepted for publication in Nanotechnology.

Poster

E. M. Sala, <u>**Y. I. Na**</u>, M. Godsland, A. Trapalis, and J. Heffernan, Droplet epitaxy of InAs/InP quantum dots in MOVPE at the telecom C-band, Quantum Dot 2020 (QD2020), Munich, 2020

Abbreviations

AFM	Atomic Force Microscopy
DE	Droplet Epitaxy
EBL	Electron-Beam Lithography
FSS	Fine-Structure Splitting
GRI	Growth Interruption
ICP	Inductively Coupled Plasma
MBE	Molecular-Beam Epitaxy
ML	Monolayer
MOVPE	Metal-Organic Vapor Phase Epitaxy
PL	Photoluminescence
QD	Quantum Dot
QKD	Quantum Key Distribution
RIE	Reactive Ion Etching
SCCM	Standard Cubic Centimetres per Minute
SCQD	Site-Controlled Quantum Dot
SEM	Scanning Electron Microscopy
SIMS	Secondary Ion Mass Spectrometry
S-K	Stranski-Krastanov
TEM	Transmission Electron Microscopy
TMIn	Trimethylindium

Table of Contents

1 Introduction

The speed of a classical computers is determined in large part by the number of transistors in its central processing unit (CPU). For over a half a century, computing performance has increased exponentially as the number of transistors able to fit on a microchip of a given size doubles approximately every two years, as predicted by Moore's Law [1]. However, this trend cannot last; as transistor sizes shrink, they will eventually encounter hard physical limits that cannot be bypassed, and issues such as quantum tunnelling effects that can cause current leakage [2]. A quantum computer is a potential alternative [3]. It uses qubits, the quantum mechanical analogue of the regular bits that encode information in a classical computer. Qubits behave very differently to classical bits. In a classical computer, a bit can only be in one of two states, typically 0 or 1, but a qubit in a quantum computer can exist in a state of both 0 and 1 at the same time, something called superposition. In theory, they allow the computer to carry out certain kinds of calculations exponentially faster than a classical computer by taking advantage of this superposition phenomenon. The potential for quantum computers to employ Shor's algorithm for integer factorisation is a quintessential example. It is a killer application of quantum computers as an algorithm that can make public-key cryptography schemes useless. A single semiconductor quantum dot (QD) is one candidate for the development of solid-state qubits [4]; of particular relevance to this thesis is their ability to serve as single photon sources which can be manipulated in quantum photonic devices.

In addition, for quantum communications networks, such as for quantum key distribution (QKD) [5], InAs/InP QD systems are of particular interest as they emit photons in the low-loss fibre telecom window around 1550 nm [6]. InAs/InP QDs produced via the Stranski-Krastanov mode have been extensively explored but, due to the small lattice mismatch between the two materials, asymmetric dashes are often produced which results in large FSS (fine-structure splitting) [7], [8]. FSS comes from the asymmetry in the QD wave function produced by changes in crystal strain and composition, as well as the elongated-shape of the QD which is a

natural outcome of the S-K growth mode [9]. One approach to producing QDs with small FSS is to use an alternative epitaxy technique called droplet epitaxy (DE) [10], [11]. Because DE QDs are not formed by strain, their shape is less elongated and can be used to improve the overall single photon emission properties of these dots. A recent paper [10] has indeed shown a 72% improvement in symmetry from DE QDs compared to S-K QDs.

On the other hand, randomly distributed QDs lower the device yield of photonic devices and, in general, to consider the industrial scale-up of QD-based devices some degree of deterministic control of the positions of QDs on a wafer is required. Epitaxy of QDs, such as S-K or DE nucleation produce randomly distributed QDs over the wafer [12]. Although there have been many research results produced from randomly placed QDs, producing photonic devices that require a single photon source to be in a certain position and to emit at a specific wavelength at high yields remains very challenging [13], [14]. Growth of so called 'site-controlled QDs' can therefore greatly reduce fabrication challenges in the production of scalable quantum circuits.

Site control of S-K QDs, via both molecular-beam epitaxy (MBE) and metal-organic vapour phase epitaxy (MOVPE), has been studied widely. However, site control of droplets followed by crystallisation into dots has not been done using MOVPE, which is the industry-favoured growth mode. Therefore, this thesis is focused on the development and implementation of the processes required to produce site-controlled InAs/InP QDs via droplet epitaxy using MOVPE. The scope of the thesis concerns the development of InAs/InP QDs growth method, suitable for the applications above, via droplet epitaxy using MOVPE, and their positioning on pre-patterned substrates. Controlling the QD position is done so as to allow integration into on-chip waveguide devices, and to increase the level of control over the properties of individual QDs; with the aim that this could eventually aid mass production of qubit devices.

This thesis is divided into six chapters, including the introduction and conclusion. Chapter 2 will give relevant background knowledge concerning III-V semiconductor quantum dots, droplet epitaxy, the MOVPE epitaxial growth technique, and a more detailed overview of droplet epitaxy via MOVPE. Chapter 3 describes the methods for the fabrication of nanohole arrays, the growth of droplets and QDs with DE via MOVPE, and characterisation techniques. In chapter 4, droplet formation, the crystallisation of these droplets and optimisation process for this on planar substrate will be discussed. In Chapter 5, the development of site-controlled droplets and QD growth on pre-patterned nanohole arrays will be presented. Finally, the thesis

will conclude with a summary of the project, with directions for future work proposed in Chapter 6.

2 Background

The increase in scholarly attention to low-dimensional quantum structures and their applications was covered in the introduction chapter, along with the scope of this thesis. This chapter gives an introduction to the background of III-V semiconductor systems, epitaxial quantum dots (QDs), and the site-control method. Firstly, the material properties of III-V semiconductors, including their crystal structures and the crystallographic planes, will be discussed. Secondly, the physical fundamentals of low-dimensional structures and their properties will be explained. Thirdly, two epitaxial growth techniques to grow self-assembled quantum dots, namely the Stranski-Krastanov (S-K) growth and droplet epitaxy, will be described. Lastly, previous studies on pre-defined QD formation on nanohole-patterned templates will be presented.

2.1　Compounds Semiconductors and Crystal Growth Techniques

2.1.1　III-V compound semiconductors

Compound semiconductors, unlike single elements such as silicon, are made up of two or more different kinds of atoms. III-V semiconductors refer to compounds comprised of one or more elements from the Group III (e.g. Al, Ga, In) and from the Group V columns (e.g. P, As) of the Periodic Table. Compound semiconductors are gaining traction as key materials for optoelectronic applications due to their optical and electrical characteristics, namely their light emission properties and high electron mobility [15]. Over the last two decades, compound semiconductors have been used for devices such as amplifiers and light-emitting diodes (LEDs) [16]–[18]. More recently, they have been used for lasers for optical storage, and fibre communications for the Internet [19]. Lately, vertical cavity surface emitting lasers (VCSELs) [20] are being used for 3D facial recognition, and a new generation of micro-displays is being developed based on micro-LEDs [21]. There is now also an emerging market for quantum devices, for use in quantum computing and communications [4], [22], [23]. Although the

market for compound semiconductors is much smaller than the dominant market for silicon in electronics, a significant amount of work is nevertheless being done on these materials.

2.1.2 Zinc blende structure

A sphalerite or zinc blende structure is the most common crystal structure for III-V compound semiconductors, including InP and InAs [24]. Figure 2-1 shows the cubic unit cell of a zinc blende structure. The small yellow spheres represent Group V element atoms (e.g. As/P), whereas the large grey spheres indicate Group III element atoms (e.g. In). A sphalerite structure is exactly the same as a diamond structure except that it consists of two different types of atoms while a diamond structure is composed of a single type of atom. Each atom type forms a face-centred cubic (FCC) in which each atom is bounded by four atoms of the opposite kind.
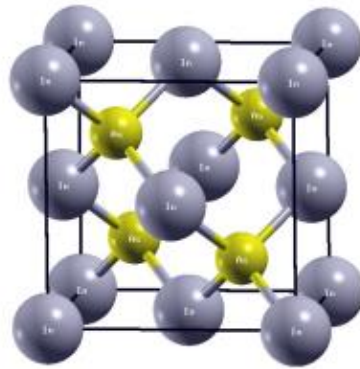
Figure 2-1 Three-dimensional unit cell for the zinc blende structure [25]

The III/V system that is of interest to this thesis is InAs QDs on InP. It is a highly appealing material system for fibre-based quantum network applications because they emit in the C-band [26]–[29]. Wavelengths in the C-band (1530-1565 nm) are noteworthy because they have the lowest attenuation in optical fibres, making the band attractive for long-wavelength optoelectronic devices [30]. The lattice constants, a term which refers to the length of the unit cell, are a = 5.8687 Å and 6.0583 Å at 300 K for InP and InAs, respectively. This leads to a lattice mismatch of ~3.2%, which is a relatively small value for S-K epitaxy.

2.1.3 Crystallographic planes

In this work, n-type (sulphur-doped) InP (100) substrates were mainly used. Miller indices are used to indicate directions and planes. Figure 2-2 shows a standard n-type InP (100) substrate,

with the two natural cleavage directions along the $[0\bar{1}1]$ and $[0\bar{1}\bar{1}]$ directions indicated. In relation to the wafer surface, the primary flat has a certain crystal orientation, while the secondary flat denotes the wafer's crystal orientation and doping. Its location relative to the primary flat varies depending on the type of doping.
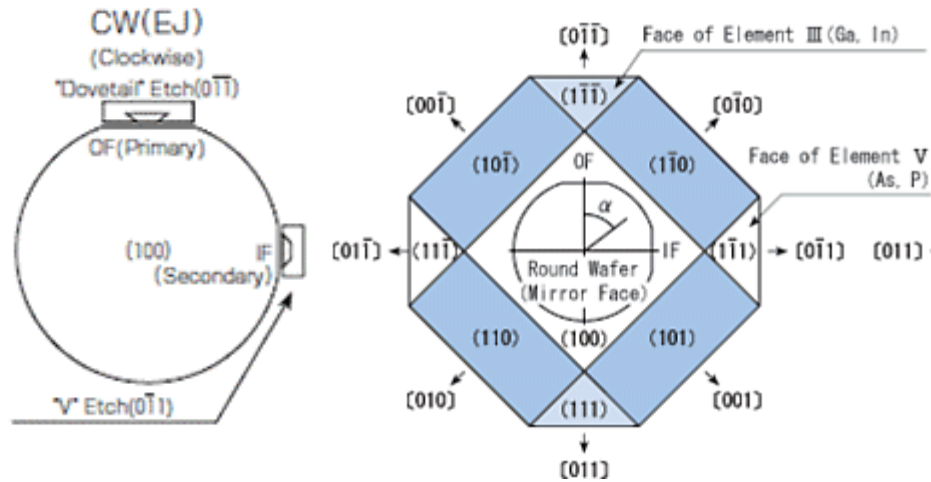

Figure 2-2 A (100) oriented InP wafer (left), and a planar representation of the cubic form (right) [31]

2.2 Low-dimensional Quantum Structures

Over the last few decades, there has been a significant amount of interest in low-dimensional semiconductors such as quantum wells, quantum wires, and quantum dots. Progress in epitaxial growth techniques, such as MBE and MOVPE, have accelerated the development of such low-dimensional quantum structures, where growing semiconductor structures and controlling their dimensions with atomic-scale precision have become possible. In quantum wells, the movement of carriers (i.e. electrons and holes) are restricted to a single plane. Quantum wells can be fabricated by sandwiching a material with a narrow bandgap between two layers of a wider bandgap material. The structure of a quantum well has been extensively researched and is now well understood. Quantum well lasers could have low threshold current densities whereas, in bulk materials, lower energy states should be filled up to reach the required energies for lasing to occur. Further reducing the dimensionality to quantum wires and quantum dots confines the carriers to a space where two or all three dimensions are restricted, respectively. The effects of quantum confinement can be observed only if the dimension of the material is comparable to the order of the carrier's de Broglie wavelength. The de Broglie wavelength is [32]:

$$\lambda = \frac{h}{p} = \frac{h}{\sqrt{3m_{eff}kT}} = \frac{1.22nm}{\sqrt{E_{kin}/[eV]}} \qquad (2.1)$$

Where p is the momentum, h is the Planck constant, m_{eff} is the effective mass of the carriers, and E_{kin} is the kinetic energy.

Therefore, considering the typical values of the effective mass of the electron (or hole) and the working temperatures, the space in a low-dimensional semiconductor can be restricted to a few nanometres.

In addition, the dimensionality of the semiconductor affects the form of the density of states, through confinement. Quantum confinement causes carriers to be strongly quantised and to possess discrete energy values whereas bulk structures are classical in nature, with continuous energy levels and gaps. The density of states (DOS) describes the number of allowed energy states within a structure, providing carrier concentration information and spatial confinement information. The reduction of the dimensionality of a system results in a strong modification to the system's DOS [33]. Figure 2-3 shows the DOS of materials with decreasing dimensionality and decreasing degrees of freedom.
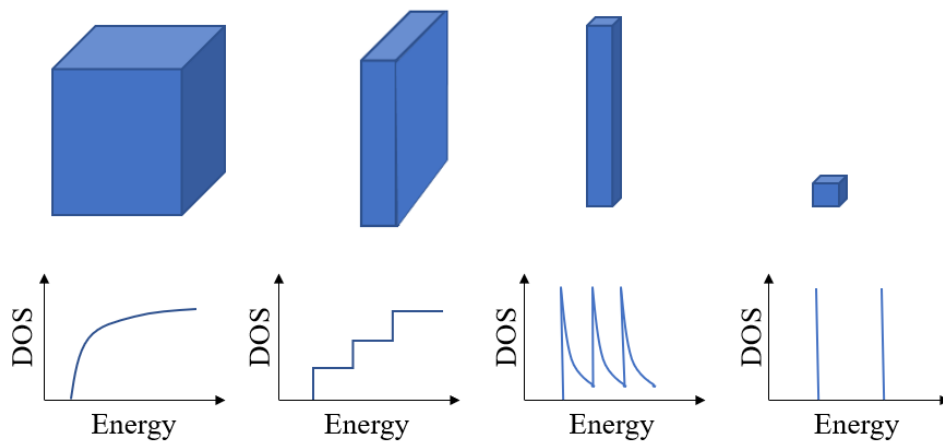

Figure 2-3 Schematic of the effects of electronic confinement on the density of states for: (a) a bulk structure, 3D (b) a quantum well, 2D (c) a quantum wire, 1D (d) a quantum dot, 0D [33]

Three-dimensional systems (bulk systems) have continuous functions, two-dimensional systems (quantum wells) have step functions, a one-dimensional system (quantum wires) has a

peculiar function, whilst a zero-dimensional system (quantum dots) has the shape of the δ function, in which there are no directions for free motion. In a low-dimensional system, the number of available energy states where carriers may be thermally excited are restricted, resulting in improved thermal stability for laser systems.

QDs are sometimes referred to as artificial atoms due to their discrete spectrum of energy levels [34]. Their unique optical and electrical properties make them of particular interest in modern electronics. They emit light of different wavelengths depending on their size, shape, and material composition. Therefore, it is possible to precisely tune the emitted wavelength by controlling these factors. QDs, owing to their unique properties, are used in many applications such as QD solar cells, light-emitting diodes, lasers, and quantum computers [35]–[38]. In order to make them useful for devices operating at room temperature, QDs should have sufficiently deep localising potential, and high uniformity with low defect levels.

2.2.1 Quantum dot transitions

When sufficient energy is provided, an electron is excited, leaving a hole behind in the valence band. The electron and the hole are attracted to each other by an electrostatic force, creating an electron-hole pair, called an exciton. Biexcitons are made up of two excitons bound in a single complex. When the electron and hole recombine, or in equivalent terms when an exciton relaxes to the ground state, it generates a photon with an energy equal to the energy difference between the two levels.
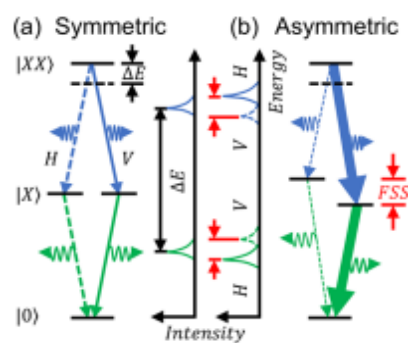

Figure 2-4 A schematic of the energy structures of ideal QDs and practical QDs with FSS. Reprinted with permission from H.-S. Yeo et al., "Control of the 3-Fold Symmetric Shape of Group III-Nitride Quantum Dots: Suppression of Fine-Structure Splitting," *Nano Lett*., **20**, 12, 8461–8468, 2020.Copyright (2020) American Chemical Society. [39]

There are several charge configurations possible within a QD which determine the optical emission spectra. Figure 2-4 shows a schematic of the energy structures of ideal QDs and practical QDs. A biexciton-exciton emission cascade starts with the radiative decay of the biexciton (XX) state by emission of a horizontally (H) or vertically (V) polarised photon. Ideally, the two orthogonally polarised emissions are entangled and energetically indistinguishable. However, for practical QDs, this entanglement is degraded when the exciton states become no longer indistinguishable through fine structure splitting (FSS) between the exciton eigenstates. FSS is a slight energy difference during the transition caused by the interaction between the spin of the electron and the magnetic field produced by the orbital motion of the electron. With a finite FSS, the quantum state of the exciton level will precess between the states of $\pm 1/\sqrt{2}$ ($|{\downarrow}{\Uparrow}\rangle - |{\uparrow}{\Downarrow}\rangle$) and $\pm 1/\sqrt{2}$ ($|{\downarrow}{\Uparrow}\rangle + |{\uparrow}{\Downarrow}\rangle$). QD FSS originates from the asymmetric QD shape and the anisotropic piezoelectric potential. A large FSS could mean photons produced by the QD will not be indistinguishable, complicating any observation of the entanglement. Quantum applications that demand a high level of indistinguishability, such as in quantum computing and quantum key distribution, might suffer as a result of this [40], [41].

2.3 Quantum dot growth

Since the 1980s, a lot of work has gone into realising this three-dimensional confinement structure (i.e. QDs), such as lithographic patterning to etch quantum well structures. Of these, self-organised formations of QDs, which naturally occur during growth of lattice-mismatched materials, have been used conventionally to achieve high quality and dislocation-free QDs. QDs grown via this technique are called strain-induced QDs or QDs grown by the Stranski-Krastanov (S-K) mode [42]. This method begins with the deposition of a strained layer of different to the substrate material on the substrate. After a certain critical thickness, a transition from a 2D layer to 3D islanding growth takes place to relax the strain energy. The 2D layer deposited before the QD formation is called the wetting layer. A relatively high degree of lattice mismatch (~7%) is a prerequisite for this technique.

2.3.1 Growth modes and Stranski-Krastanov quantum dots

The growth modes may be categorised into three types depending on the interaction between the substrate surface and the deposited layer: the Volmer-Weber mode, the Stranski-Krastanov mode, and the Frank-van der Merwe mode [43]. A schematic illustration of these three growth

modes is shown in Figure 2.5. A set of deposition, desorption, and surface diffusion processes take place during growth which determine the morphology of the interface.
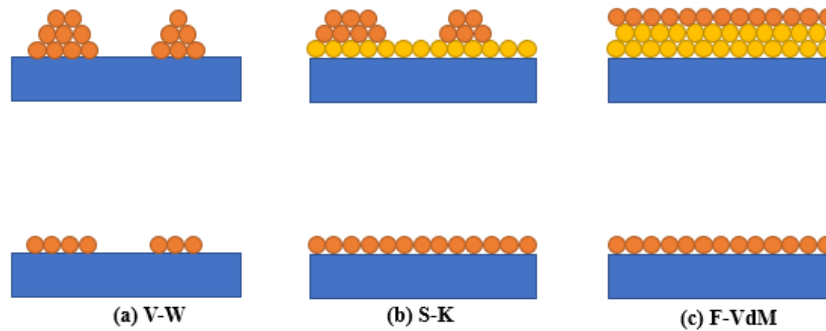

Figure 2-5 Schematic illustration of the three growth modes: (a) Volmer-Weber (b) Stranski-Krastanov (c) Frank-van der Merwe

Firstly, during the deposition process, an atom or molecule of the depositing material arrives on the surface and sticks to the surface atoms. Some of the deposited atoms remain on the surface whilst others leave. The strength of the bonds between the deposited atoms and the surface atoms, which depends on the type of atoms in question or on the local atomic arrangement of the surface, determines the probability of desorption. During the diffusion process, atoms move around to find the most energetically favourable position. The diffusion length can vary depending on the binding energies of the substrate and the temperature.

The relationship between the energies of the two materials' surfaces and the surface energy of the two materials in contact (interface energy) determines the growth mode in lattice-matched systems. When the sum of the surface energy of the epitaxial layer (γ_f) and the interface surface energy (γ_i) is less than the surface energy of the substrate (γ_s), where $\gamma_f + \gamma_i < \gamma_s$, it is energetically favourable for the epitaxial layer to completely wet the substrate, resulting in layer-by-layer growth. This is referred to as the Frank-van der Merwe (F-vdM) mode. In other words, the binding energy in the vertical direction is stronger than that among the deposited atoms in the lateral direction ($E_{Bv} > E_{Bl}$) so that islands of monolayer height merge together before a new layer can nucleate on top of them.

In contrast, in the Volmer-Weber (V-W) mode, which is also called island growth, like its name suggests, interaction with the substrate atoms is weaker than that between the neighbouring atoms in the lateral direction ($E_{Bl} > E_{Bv}$), and so many discrete islands form

without merging into a layer. In other words, when $\gamma_f + \gamma_i > \gamma_s$, it is energetically more favourable to have the substrate surface exposed to the vapour, resulting in the formation of 3D islands. This growth mode is usually observed in strained layers with a lattice mismatch greater than 10%. The former growth mode (F-vdM) is the most used epitaxial growth mode, while the latter growth mode (V-W) can be used to explain phenomena when a metal is deposited on top of a semiconductor.

On the other hand, in a lattice-mismatched material system, growth commences with layer-by-layer growth. The epitaxial layer deforms elastically and generates the strain energy. As the growth continues, the strain energy accumulates and reaches a thickness at which it cannot accommodate more strain elastically. Therefore, it has to find a way to relieve the strain. There are two ways to relax: one is to generate misfit dislocations at the interface; the other is to form 3D islands. The latter is the Stranski-Krastanov mode which is a sort of intermediate case between the two growth modes described above. Deformation then takes place to overcome this lattice mismatch. The S-K mode is the most archetypal way of fabricating self-assembled QDs [44]. Therefore, lattice mismatch is the driving force behind self-organised strain-induced QD formation. Many attempts have been made to reduce FSS in S-K QDs: thermal annealing [45], applying an external strain or electric field [46], and growth on (111) surfaces [47], [48].

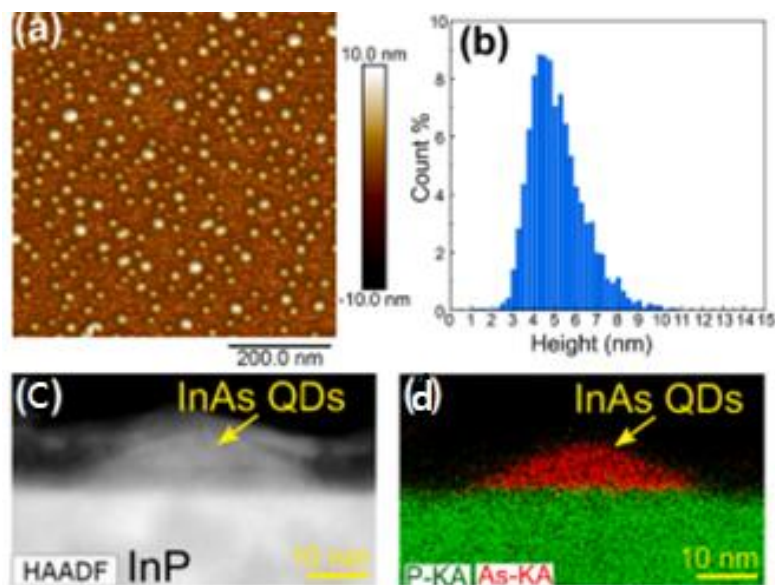Figure 2-6 (a) Atomic force microscopy image (b) height histogram (c) cross-sectional TEM (transmission electron microscopy) image (d) chemical composition by EDS (energy-dispersive X-ray spectroscopy) of InAs quantum dots grown on an InP substrate. Reprinted with permission from S. Hasan, et al., "Encapsulation study of MOVPE grown InAs QDs by InP towards 1550nm emission," J. Cryst. Growth, vol. 557, p. 126010, 2021. [49]

Figure 2-6 (a) shows an AFM image of typical uncapped InAs/InP (001) quantum dots, grown with the S-K growth mode via MOVPE, having a surface density of 2.2×10^{10} cm^{-2}. The QDs have an average width of 40 ± 9 nm and a height of 5.4 ± 1.3 nm. A cross-sectional TEM image of a single dot is shown in Figure 2-6 (c). The image revealed a reduction in the dot height to 2.5 nm caused from the P/As exchange process during capping which enables a near 1550 nm emission wavelength. For S-K QDs, crystal defects can develop as a result of strain relaxation, which have a significant impact on a QD's optoelectronic characteristics. The development of epitaxial growth techniques such as MBE and MOVPE, along with growth optimisation, has allowed for the production of defect-free QDs. By adjusting the growth parameters such as growth temperature, growth rate, and coverage, the size, shape, composition, and density of QDs may be tuned. However, the main constraints of S-K QDs are the presence of the 2D wetting layer, strain-driven intermixing of QDs, and a limited degree of freedom in lattice-mismatched materials. In a heteroepitaxial system in which the compounds are of different groups, intrinsic stress asymmetry is present along the [1$\bar{1}$0] and [110] directions at the interface, as is the case with InAs/InP [8], [50]–[52]. This causes the nanostructures to be elongated along those directions and quantum dashes to develop rather than QDs, which have larger than ideal fine structure splitting (FSS) [9]. Also, size variations and randomly distributed nucleation sites are unavoidable owing to the self-assembly process.

2.4 Quantum dots produced by droplet epitaxy

DE is another method to achieve highly symmetric QDs, resulting in a low FSS. According to [10], the DE QDs are more symmetric with a width to length ratio of 0.91 ± 0.16 while the S-K QDs are elongated toward [110] with the ratio of 0.53 ± 0.13. By employing DE, the symmetry of the QDs is improved by 72% and the FSS was reduced down to one-fourth that of S-K QDs.

Koguchi et al. [53] first experimentally demonstrated the fundamentals of DE via MBE in 1991. The droplet epitaxy mechanism consists of two basic steps. Firstly, a Group III material such as gallium (Ga), indium (In), or aluminium (Al) is deposited, forming metallic nano-sized droplets on the surface via the V-W growth mode, due to their high surface tension. The driving forces behind the droplet formation are the combination of the diffusion process, the minimisation of the surface energy, and Ostwald ripening. Ostwald ripening is a phenomenon in solid or liquid solutions in which small solution particles dissolve and redeposit onto larger

solution particles. Then, the clusters of droplets are crystallised, forming into QDs in the atmosphere of a non-metallic component (usually a Group V material).

The greatest advantage of DE is the flexibility with the choice of substrate material and its orientation. Since QDs grown by DE are not strain-driven, unlike QDs grown via the S-K mode, it offers more choice for the QD material (with lattices matched or mismatched to the substrate). The first QDs by DE demonstrated by Koguchi and his colleagues [53] were an InSb/CdTe system whose lattice constants were nearly the same. Many researchers have used this advantage and demonstrated the growth of QDs on lattice-matched system such as GaAs/GaAs [54] or GaAs/AlGaAs [55]–[57]. In contrast, the growth of QDs on (111) or (011) have since become possible, which has historically been a significant challenge for the S-K growth mode because strain relaxation occurs through the introduction of dislocations rather than QD formation. Later, though, it was accomplished by using tensile strain [58]. Using DE on (111) surfaces, highly symmetric QDs with a vanishingly low fine structure splitting (FSS) were presented by [59]–[61]. The wide variety of substrate orientations available offers benefits for various applications.

In addition, DE allows for the production of various shapes of zero-dimensional quantum structures such as ring-like QDs [62] and concentric quantum double rings (CQDRs) [41], through controlling the lateral diffusion of the metallic components from the droplets. The ability to modify a QD's shape is critical since the shape determines its electronic properties. In [62], the authors observed the shape derivation of GaAs QDs by varying the crystallisation temperature. Ring-shaped QDs were fabricated at high temperatures combined with lower As flux while pyramidal-shaped QDs were fabricated at lower temperatures. This is because, at high temperatures armed with a lack of arsenic, the lateral migration of Ga atoms from the droplets are not completely suppressed. CQDRs produced by DE were first reported by [41]. In the paper, the formation of CQDRs was realised by lowering the As flux during crystallisation. The diameter of the outer ring was affected by the As flux while the diameter of the inner ring was the same as the diameter of the precursor droplet.

Another benefit of DE is the ability to control the wetting layer. For S-K QDs, the thickness of the wetting layer (i.e. critical thickness) cannot be controlled and is determined by the lattice mismatch between the substrate and the deposited material. In contrast, a wetting layer is not necessary to form QDs via DE. However, a 'quasiwetting' layer can be formed as a result of the Group V element intermixing during crystallisation. For DE QDs, the wetting layer

thickness can be manipulated by adjusting the stoichiometry of the substrate surface immediately before Group III element droplets are deposited [63].

On a planar substrate, QD properties, such as density, size, and shape, can be controlled via several growth parameters: growth temperature, indium deposition time, indium flow, growth interruption (GRI), arsine flow, and crystallisation temperature. QD density when produced via DE is dependent on temperature. According to [64], there are two temperature regimes. Under 200°C, the density follows classical nucleation theory and obeys the scaling law with an activation energy of 0.235 eV. On the other hand, over 200°C, the density drastically decreases due to coarsening from Ostwald ripening.

The initial studies into DE were only performed under MBE conditions because a low growth temperature was required to achieve the V-W growth condition. Since MBE uses elemental sources, it can provide a low-temperature environment which offers a high surface tension of a melt. In contrast, this is one of the difficulties in employing droplet epitaxy under MOVPE conditions since the process of decomposition of gaseous sources and the deposition of the material take place at the same temperature. Gaseous sources like metal organic compounds and hydrides have high thermal stability and decompose at relatively higher temperatures. This is why QDs produced by DE via MOVPE have had fewer studies done on them compared to those produced via MBE.

2.4.1 Droplet epitaxy quantum dots via MOVPE

QDs produced by DE via MOVPE have been subject to extensive study only recently. A 2017 paper demonstrated the development of high quality InAs/InP QDs by MOVPE with lower FSS compared to S-K QDs [10]. According to [65], trimethylindium (TMI) in H_2 completely decomposes above 350°C and it decreases with an activation energy of 39.8 kcal/mol and almost vanishes below 250°C. The presence of a substrate, acting as a catalyst, reduces the pyrolysis temperature. For instance, the activation energy is decreased to ~9 kcal/mol on a GaAs substrate, allowing deposition of indium to take place at considerably lower temperatures, down to 100°C. Likewise, GaAs and melted indium surfaces produce a catalytic effect, making arsine more likely to decompose on the surfaces of indium droplets.

Nonogaki et al. [66] demonstrated InAs QDs on InP (011) fabricated by MOVPE using DE. In [67], it was observed that TMIn supply time affects the total amount of supplied TMIn and, in

turn, affects dot formation. AFM and PL measurements confirmed dot formation at 3 monolayer (ML) of TMIn and no dot formation where TMIn < 1.5ML, suggesting the critical coverage for the indium supply to from droplets was between 1.5 and 3ML. The effect of crystallisation temperature was also investigated; a decrease in the size and density of the dots was observed alongside a decrease in the substrate temperature. In addition, the effect of substrate misorientation (from 1° to 4°) on dot density and uniformity was investigated in [68]. At an orientation of 2°, the dots formed most uniformly and symmetrically, and with the highest dot density. On the other hand, the total volume of dots increased with misorientation even though the amount of the supplied In was fixed to 3ML. The authors attributed it to the high density of step edges on the misoriented surface. The weakly bonded phosphorous atoms at the step edges are easily desorbed when In is being supplied, and then exchanged with arsenic atoms during crystallisation, resulting in the increased total In volume.

Ring-shaped QDs produced by DE were fabricated under MOVPE conditions too. A paper by Sormunen et al. [69] discussed the transformation of InAs/InP DE QDs into quantum rings without capping. For an InAs/InP system, which shares the same Group III atom, the transformation is heavily influenced by Group V exchange reactions. The modification of the QD's morphology was realised by thermal annealing in a phosphorus ambient after crystallisation. The driving forces behind this transformation are the combination of As/P exchange and indium adatom diffusion due to elastic strain relaxation.

On the other hand, one of the problems with InAs/InP QDs for device application is the large size dispersion, which causes broad photoluminescence spectra. A study to improve the size homogeneity of InAs/InP QDs produced by DE was also performed by using mesa-structure templates [70]. The size of the QD was controlled by the width of the top surface of the templates and therefore a narrow PL peak was obtained.

Akchurin et al. [71] reported the formation of QD arrays in a InAs/GaAs system under MOVPE conditions. They showed the dependence of droplet size on pyrolysis temperature and suggested a way to reduce this droplet size by thermal treatment. Within a temperature range of 300-400°C, a size reduction of droplets was achieved without changing the droplet composition.

Elemental diffusion from the substrate was also reported in [72]. The authors compared two types of indium droplet sample: one which was immediately cooled to room temperature

following indium deposition and one which was maintained for an additional 8 seconds after deposition at the growth temperature and a cooling down process. The results showed that the one with an 8-second growth interruption showed a larger amount of Ga as the substrate bonds tended to break and alloy with indium droplets at the growth temperature. This is because the decrease in the overall elastic energy of the system suppresses Ga diffusion into the droplets [73]. The authors also observed that diffusion from the substrate was suppressed when they supplied arsine flux.

2.5 Site-controlled quantum dots

Thanks to their unique optical and electrical properties, self-assembled QDs have improved the performance of lasers and optical amplifiers. However, precise site control of QDs is essential for sophisticated quantum communication devices such as single photon sources. Site control of QDs can be achieved by pre-defining the QD nucleation point in various ways which provide low energy regions for preferential nucleation. The substrate can be patterned in a number of ways, including through the use of electron-beam lithography (EBL), focused ion beam (FIB) lithography, local anodic oxidation (LAO), and nanoimprint lithography (NIL). All these processes seek to form a nanohole site, either through (dry or wet) etching of the substrate after patterning a resist; sputtering away the substrate; forming an oxide which can be removed to form the hole; or creating a mould which can stamp a polymer resist prior to etching.

In this thesis, EBL was chosen as the method to pattern the substrate. The substrate was patterned first with an e-beam and then etched (dry or wet) to get a set of nanohole arrays. There is evidence to show that defects and contamination causes inhomogeneous line broadening in PL measurements [74], [75]. Therefore, during fabrication, a cleaning method and various etching methods should be investigated to ensure sufficiently low damage and contamination and thus achieve the highest possible optical quality. This was a major element of the work presented in this thesis. Crystal anisotropy is also a factor to be considered during the growth process, as growth anisotropy tends to elongate the nucleation sites [76]. The quality of the produced QDs can be analysed though the use of photoluminescence (PL) linewidths of single dot emissions or the average linewidth of a set of QDs. Furthermore, the occupancy of nucleation sites, the regularity of QD nucleation in an array of nanoholes, the position at which a QD nucleates in a hole, and emission wavelength can all be used to characterise QD quality.

An attempt to fabricate site-controlled In(Ga)As/ GaAs QDs on nanohole arrays was demonstrated by Huggenberger et al. [77]. The substrate was patterned via e-beams and wet etching. Site-controlled In(Ga)As/GaAs QDs with a linewidth of a single QD emission down to 43 µeV was achieved by MBE. Figure 2-7 shows scanning electron microscope (SEM) images of a regular array of etched nanoholes, and the subsequent growth of positioned S-K QDs.
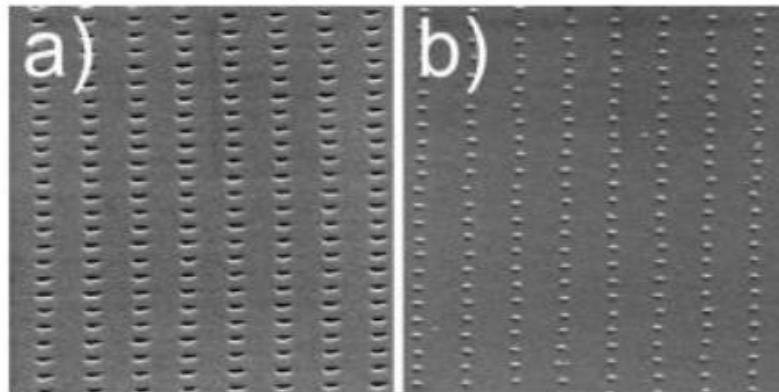

Figure 2-7 SEM images showing (a) a regular array of 100 nm nanoholes with a pitch of 300 nm, and (b) subsequent site-controlled quantum dot (SCQD) growth. Reprinted with permission from A. Huggenberger et al., "Narrow spectral linewidth from single site-controlled In(Ga)As quantum dots with high uniformity," Appl. Phys. Lett., vol. 98, no. 13, pp. 2009–2012, 2011. [77]

Site control of QDs on a nanohole-patterned substrate was also demonstrated by Nakamura et al. [78]. The GaAs (100) substrate was patterned via e-beam lithography (EBL) and reactive ion etching (RIE). The nanoholes were arranged in a square lattice with a diameter of 80 nm, a depth of 25nm, and a pitch of 200 nm; Figure 2-8 shows transmission electron microscopy (TEM) images of the vertical alignment of the laterally ordered In(Ga)As QD arrays stacked on the nanohole arrays. This is because the strain field generated from the underlying QDs causes the vertical alignment.
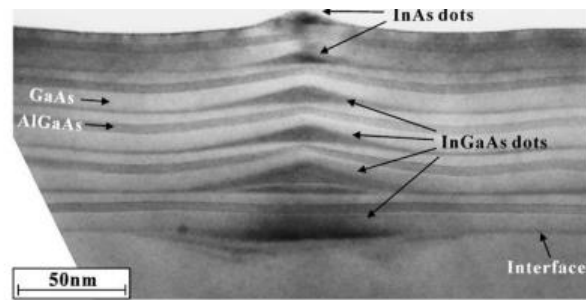
Figure 2-8 TEM image of a single column of stacked In(Ga)As QDs using nanohole array fabricated by EBL and RIE. Reprinted with permission from Y. Nakamura *et al.*, "Vertical alignment of laterally ordered InAs and InGaAs quantum dot arrays on patterned (0 0 1) GaAs substrates," *J. Cryst. Growth*, vol. 242, no. 3–4, pp. 339–344, Jul. 2002, doi: 10.1016/S0022-0248(02)01442-2. [78]

2.6 Summary

In this chapter, the physics background of QDs and their growth techniques was provided and recent work on site-controlled QDs and DE QDs by MOVPE was reviewed. However, so far, no work has been done on site-controlling DE QDs by MOVPE. The novel aspect of the work which will be described in the thesis is site control of the droplets first, followed by crystallisation of QDs by MOVPE.

3 Experimental Methods

In this chapter, the experimental methods that have been used in this project will be described. Firstly, the fabrication processes for micro-holes and nanoholes including patterning, etching, and cleaning will be presented. And then, the principles of MOVPE, the epitaxial technique used for droplet and QD growth, will be described, including the proposed structure of InAs/InP QDs grown via droplet epitaxy and the sequence for their growth. Finally, the techniques for characterising the properties of droplets and QDs or the patterned array of nanoholes will be outlined. Fabrication and characterisation of samples were implemented by the author unless otherwise mentioned in the text. Growths using the Aixtron MOVPE reactor were performed by Dr. Elisa M. Sala.

3.1 Substrate Patterning

3.1.1 Photolithography

Photolithography is a lithography technique which uses ultraviolet (UV) light to prepare the surface of a semiconductor wafer so that a specific pattern can be transferred for subsequent processing steps, such as etching or metallisation. Photolithography is the most extensively utilised method in the microelectronics industry. The resolution limit in standard 365 nm (i-line) UV photolithography is calculated using the following equation.

$$\text{Resolution limit} \sim k \, (\text{constant}) \text{x} \, \sqrt{\lambda h} \qquad (3.1)$$

where λ is the wavelength of exposure, h is the photoresist thickness, and k refers to the diffraction limit value. The constant k is $\sqrt{2}$ in most cases but could be decreased by optimising the exposure to a desired intensity level of UV light [79].

To fabricate holes for site-controlled droplets and QDs, photolithography was used in the first instance in order to get a broad idea of how indium atoms move around the patterned substrate

and whether or not they are trapped in the etched holes. Via this method, the samples were patterned with an array of 1µm holes with a 2.5µm pitch, using the existing mask (Figure 3-1).
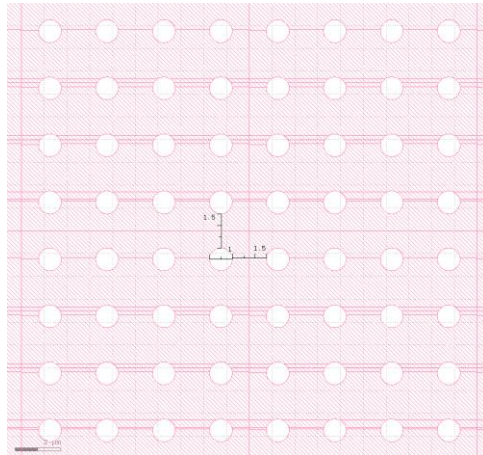

Figure 3-1 Photolithography mask design which consists of 1µm holes with a 2.5µm pitch

Figure 3-2 shows a schematic of the sequence of this nanohole fabrication process. Firstly, three-stage cleaning (with *n*-butyl acetate, acetone, and isopropyl alcohol (IPA)) was performed to remove any impurities and unwanted particles that could have adhered to the surface. Then, the sample was submerged in 1:10 H_3PO_4:H_2O for 2 minutes to de-oxidise the surface. After that, the sample was baked on a 100°C hot plate for 1 minute to desorb any H_2O present on the surface and coated with a photosensitive material called a photoresist. A positive photoresist, SPR350, was spun at 4000 rpm for 30 seconds. This results in a uniform resist film of approximately 1 µm in thickness across the wafer's entirety [80]. After this coating, the sample was baked for 1 minute on a 100°C hot plate to reduce any remaining solvent concentrations on the resist. This soft-baking process serves to improve the resist's adhesion and to increase its stability. Then, the photoresist-covered wafer is exposed to UV light for 27.5 seconds using a mask aligner, with a mask, as depicted in Figure 3-1, and then fitted. This value of 27.5 seconds was ascertained to be the optimum one through careful tests and controls. Anything outside this optimum zone would lead to under exposure or over exposure. For a positive resist, if the resist is underexposed, it remains intact after development. If the resist is overexposed, the window openings in the resist become larger than the mask dimensions. Once the wafer is exposed, the photoresist was developed with MF26A for 1 minute. For a positive resist, the area exposed to the UV light was selectively activated and depolymerised to increase its solubility in the developer, while the unexposed areas remain intact. After the development, the image of the mask was transferred to the photoresist on the

wafer. In the subsequent processing step (in this case etching), this image was transferred to the InP substrate. Figure 3-13 depicts SEM images of fabricated array of holes via this method. Photolithography has an inherent resolution limit due to the wavelength of the light used. However, compared to EBL, it is a timesaving and effective way of patterning the wafer, and so it was chosen for the initial experiment method.
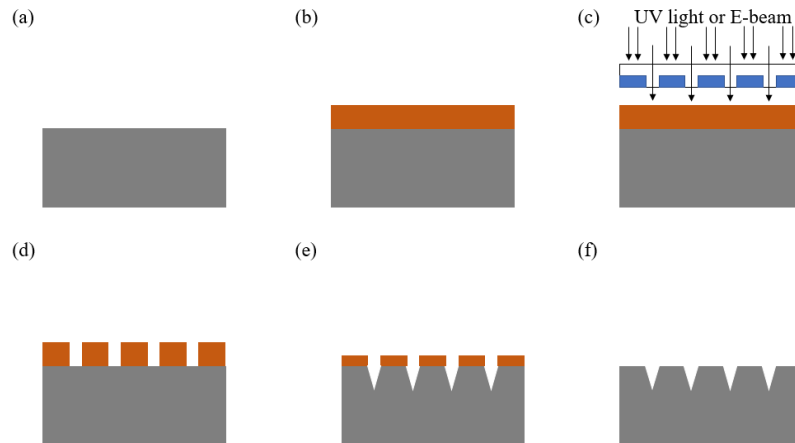

Figure 3-2 A schematic of the nanohole fabrication process sequence: (a) a bare InP (b) the resist is spun onto the sample (c) the resist is exposed to UV light (photolithography) or an electron beam (EBL) (d) areas exposed are dissolved in the developer (e) InP is etched in regions not protected by the remaining resist (f) the resist is removed.

3.1.2   E-beam Lithography

E-beam lithography or electron beam lithography (EBL) is a process similar to that of conventional photolithography but utilising electrons rather than UV light to strike the resist and form the desired pattern. The presence of electrons in the resist alters the properties of the resist material and makes it easy (positive tone) or hard (negative tone) for it to be dissolved in a developing solution. Whereas the resolution of photolithography is limited by the diffraction limit of the UV light used, via EBL, it is possible to create extremely fine features below 10 nm [81]. EBL has become an increasingly popular alternative to photolithography due to its near-atomic resolution capabilities and its versatility in terms of the patterns it can produce since it does not need a mask to block light from coming through.

This work made use of a polymethyl methacrylate resist, CSAR-62, one of the highest resolution resists available. Standard CSAR-62 has a solid content of 13% suspended in Anisole [82]; diluting it with more Anisole at a 1:2 ratio lowers that concentration, giving a

final concentration of 4.33%. This allows the depositing of a thinner film when it is spin-coated. The film thickness is determined by the spin speed as well as the resist concentration. The sample was then coated with an 80 nm layer of resist by spinning the wafer at 4000 rpm for 30 seconds with a resist spinner in the first experiments. Later, because of the need for a thicker mask for etching, the resist was spun at 2000 rpm for 30 seconds, resulting in 100 nm thickness. This allowed the resist to survive and protect the wafer for slightly longer during the etching. The sample was then baked at 180°C for 3 minutes. During this soft-bake, the casting solvent in the resist evaporates and forms a solid film. The sample was then exposed to an electron-beam using the Raith Voyager EBL system.

The nanohole pattern array was designed by the author using Graphic Database System II (GDSII) and is shown in Figure 3-3. It acts like a mask does in photolithography and indicates where to expose the electron beam. The pattern consists of four different drawn sizes (50, 100, 250, 500 nm) and, for each drawn size, five different pitches (0.5, 1, 1.5, 2.5, 4 µm) were tested to determine their effects on site-controlled droplets and QDs in the subsequent growth experiment. In order to find the right dose for each drawn size and pitch, the dose was varied from dose 50 µC/cm^2 to 300 µC/cm^2 in steps of 50 µC/cm^2. Each array of nanoholes with a certain diameter, pitch, and dose was 400×400 µm. The pattern also includes cross alignment marks to ease the characterisation via AFM and PL.
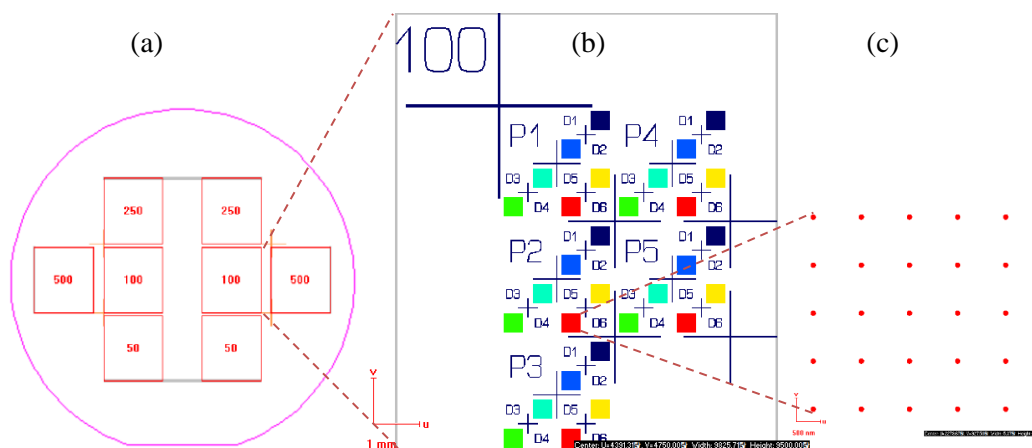

Figure 3-3 Layout of the EBL pattern (a) of a 2-inch wafer. Each square represents the drawn size of the nanohole in nm (b) A zoomed-in image of a square in (a) where pitch and dose are varied. P1 to P5 represents different pitches while different dose is represented in different colour (c) an example of a nanohole array of 100nm diameter and 1µm pitch

For the positive tone resist, the resist polymer was broken down into fragments (bond scission) via exposure to the electron-beam. The polymer may subsequently be dissolved by a developing solution. After this exposure, the sample was submerged in Xylene at 23°C for 1 minute, then rinsed in two beakers of IPA and blow-dried with N_2. The nanohole patterned resist film fabricated via this method would be used as a mask for the subsequent etching process.

For EBL, several factors must be known and specified. When using a positive resist, for a given set of resist circumstances – such as the type of resist and its thickness – the nominal dose is the lowest dosage necessary to assure complete dissolving of the resist in all areas exposed to that e-beam. It is critical that the e-beam penetrates the resist film thoroughly to achieve precise pattern transfer. That is, the resist must be thinner than the beam's energy-determined penetration depth (of electrons) into the resist film. The dose is described with the following equation [24]:

$$D = \frac{I_{beam} * t_{dwell}}{A^2} \qquad (3.2)$$

where I_{beam} is the beam current, t_{dwell} is the dwell time, and A is the step size.

A Raith Voyager EBL system was used in this work. To reduce the patterning time, two different column modes were used: for the alignment marks, a beam voltage of 50 kV in a medium current mode (approx. 2.50 nA) with an aperture of 60 µm was used; for the nanohole arrays, a beam voltage of 50 kV in a low current mode (approx. 0.54 nA) with an aperture of 60 µm was used. A base dose was set to 100 µC.cm^{-2}, which is close to the desired nominal dose. For a given set of resist conditions, six different doses were applied for each array to determine the right dose for the different drawn sizes and pitches. The dose was varied by altering the dwell time or exposure time. For the dose variation, the first nanohole array was exposed to half the nominal dose and each further array was given a 50% higher dose. For the alignment marks, a 500 µm write field was used with a 50 nm step size, a ~985 ns dwell time, and a ~49mm/s beam speed, while for the nanohole arrays, a 500 µm write field was used with a 10 nm step size, a ~180 ns dwell time, and a ~55 mm/s beam speed.

3.2 ICP Etching

The photolithography and EBL processes described in the previous section leave certain selected areas open (in this case the nanohole arrays and alignment marks) and other areas protected with the resist and ready for dry etching of the pattern. Following this patterning process, the pattern needs to be transferred from the resist to the substrate. In this process, the resist acts as a mask during the etching; the open regions are etched while the un-open areas are protected by the remaining resist.

Inductively coupled plasma (ICP) etching a dry etching technique which is performed in a gaseous environment rather than in a solution. There are various benefits of dry etching over wet etching: reproducibility, uniformity, anisotropy, and reduced undercut. In contrast to wet etching, during ICP etching, a plasma, which is an electrically charged gases, produces reactive species that etch material by chemical reaction or physical bombardment in the immediate proximity of the plasma. The resist-masked wafers are loaded into the chamber and a limited amount of reactive gas plasma of one's choice (Ar, Cl_2, and H_2 in this case) is introduced. A radio frequency (RF) source generates ICP power by inducing a magnetic field, which in turn generates an electric field and forms a plasma. The plasma is extracted and accelerated towards the sample with a controlled level of kinetic energy as a result of this power. ICP etching systems are comparable to reactive ion etching systems, except they include a second RF generator that regulate ion energy and density separately. This enables ICP to achieve high plasma densities and consequently high etch rates.
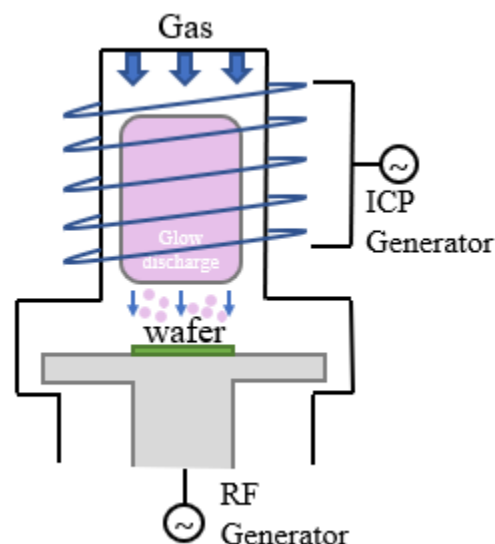

Figure 3-4 A schematic of the ICP chamber

26

Figure 3-4 shows a schematic of the ICP chamber. During etching, the carrier wafer receives an RF bias of 0 to 500 W, while the main coil by the top electrode delivers inductive coil power of 0 to 1000 W into the chamber. This enables faster etch rates, greater profile control, and greater process flexibility while also reducing the amount of material damage [83].

In this work, the etching was performed on a silicon carrier wafer in a load-locked, Oxford Instruments Plasmalab ICP etching system. The sample was placed on a silicon carrier wafer and then physically clamped with a ceramic clamping ring above the RF-biased electrode after being transported to the reactor chamber through a loadlock. According to [84], the wafer carrier material has a significant impact on the surface roughness and etching anisotropy of etched InP samples, even for the same plasma settings. The paper showed that the silicon reaction products in Cl_2-H_2 chemistry play a key role in the etching of InP. The silicon carriers produced smoother etched surfaces as well as highly anisotropic etchings with almost vertical sidewalls. The authors speculated that this positive impact might be due to the large quantity of Si+ or SiClx+ species in the plasma, which arose from the etching of silicon using chlorine. In order to prevent undercutting, a silicon carrier wafer was used throughout the project.

During etching, the electrode temperature was maintained using a mixture of water cooling and regulated resistive heating. Using helium backside cooling, which is thermally linked to the electrode, a low wafer temperature was maintained during the etching. Fomblin oil was used to thermalise the sample to the carrier, allowing the sample temperature to be controlled primarily by the electrode rather than driven by plasma heating.

It is known that the etch profiles and selectivity are dependent and so that can be adjusted and optimised by tuning the settings of some of the process parameters: chamber pressure, RF power, temperature, and gas flow. The etching gases were chosen from the literature while other process parameters including RF power and pressure was investigated through the experiments. The InP etch recipes used in this work and their etch rates are shown in Table 3-1. Two InP etch recipes were developed; one for photolithography and the other for EBL. For former recipe, deep etching was achieved by using a high flow of Ar. The bombardment of Ar increases the etch rate but also increases the surface roughness [85]. For latter recipe, Hydrogen was introduced to precisely control the etch rate by chemically bonding with the Cl_2. Introduction of H_2 also prevents the undercut through passivation. The etch rates were

investigated and established by measuring the etched depth using AFM after ICP etching. It was found that the resist selectivity is 1:2 for both recipes.

According to [86], $Cl_2/H_2/Ar$ allow anisotropic etches to be feasible at slightly higher pressures, up to 4 mTorr. For the recipes, Cl_2 was used as the main etching gas. Cl_2 and H_2 chemically etch the surface while Ar physically removes material. The main parameter controlling the etching mechanism and the sidewall profile is the composition of $Cl_2/Ar/H_2$. A ratio of 2/3/2 offered a balanced chemistry and gave a reasonable etch rate without any undercutting. As etch products, $InCl_x$ and PCl_x are produced by the chemical etching mechanism. $InCl_x$ is less volatile and more difficult to desorb, therefore, the re-deposition of less volatile products ($InCl_x$ in this case) onto the sidewalls creates the slope of the sidewall [87].

Table 3-1 InP etch recipes and the corresponding etch rates

Mask	RF Power (W)	ICP Power (W)	Pressure (mTorr)	Temp. (°C)	Gas Flows (SCCM)	Etch rate (nm/min)
Photoresist (SPR350)	100	250	2	20	Cl2-7, Ar-20	~27
E-beam resist (CSAR-62 1:2)	100	300	3	20	Ar-9, Cl2-6, H2-6	~50

To optimise the process, RF power was varied from 75 W to 200 W while everything else was kept the same. The etch rate of InP as a function of RF power is shown in Figure 3-5. The selectivity to the resists were approximately 1:1 for the photoresist and 2:1 for the e-beam resist.
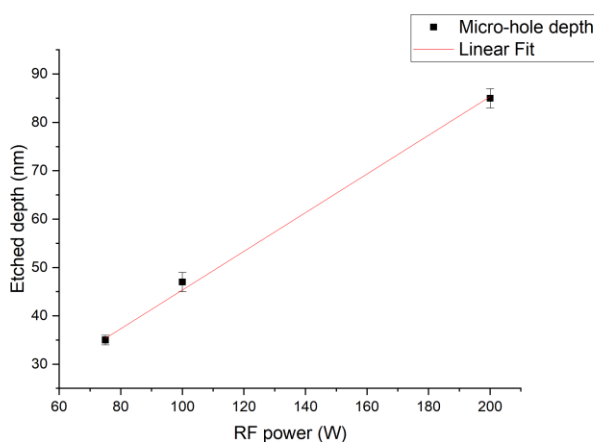

Figure 3-5 Etch rate of InP as a function of RF power

3.3 Substrate Cleaning

The most critical step in the fabrication process is the minimization of defects as it has been shown that defects and contamination cause inhomogeneous line broadening in PL measurements which affect the quality of the dots for Quantum Photonics experiments [75], [88]. The defects created during the processing could degrade the luminescence characteristics by acting as non-radiative recombination centres or charge traps. From the previous studies [88]–[90], it was shown that the presence of the regrowth interface in proximity to the dots (less than 8nm) clearly have an influence in the luminescence. They found that the peak luminescence from the SCQDs is a factor of ten times weaker than that from defect free dots and the broad lie with at low excitation power ranging from 200μeV to >3meV [88]. Therefore, during fabrication, a cleaning method to reduce the damage and contamination down to a low enough threshold was developed to achieve optimised optical quality. After ex-situ cleaning, AFM and surface SIMS were used to check the surface cleanliness. AFM analysis was used to visually evaluate the surface cleanliness for coarse optimisation while SIMS analysis was used to confirm full cleaning at the atomic impurity level.

3.3.1 *Ex situ* cleaning process

After etching, a series of cleaning recipes were tested and a process to remove all contamination including any resist residue from the flat surface and from around the nanoholes was developed. There are three different cleaning procedure to effectively clean and prepare wafers for epitaxial regrowth: solvent cleaning, oxygen plasma ash and acid cleaning. The acid cleaning was always conducted just prior to loading into the MOVPE chamber in order to prevent a native oxide growing. Oxygen plasma ash followed by solvent cleaning and vice versa were tested and compared. It was found that performing solvent cleaning before oxygen plasma ash is the most effective recipe to remove the resist. The successful cleaning procedure used works as follows:

1. Pre-heat Microposit Remover 1165, which is commercially available solvent (99% of 1-methyl-2-pyrrolidinone) for stripping resist, at 100°C on a hot plate for at least 10 minutes
2. Heat the substrate in the remover for 10 minutes
3. Sonicate for 10 minutes at 80°C
4. Rinse in two beakers of room-temperature IPA and blow dry with N_2

5. Perform three-stage cleaning (with *n*-butyl acetate, acetone, and isopropyl alcohol (IPA)) with sonicating for 10 minutes for each solvents at RT

6. Blow dry the substrate with N_2

7. Bake at 100°C on a hot plate for 1 minute to drive off remaining solvent

8. Oxygen plasma ash (RF Power: 100 W) the substrate for 3 minutes to de-scum/clean any resist residue. It removes resist through the reaction process of resist and oxygen with low kinetic ion energy.

9. Dip for 2 minutes in 4:1:100 $H_2SO_4/H_2O_2/H_2O$ to reduce carbon incorporation by removing any organic contamination, surface damage, and the native oxide layer

10. Rinse thoroughly in deionised (DI) water
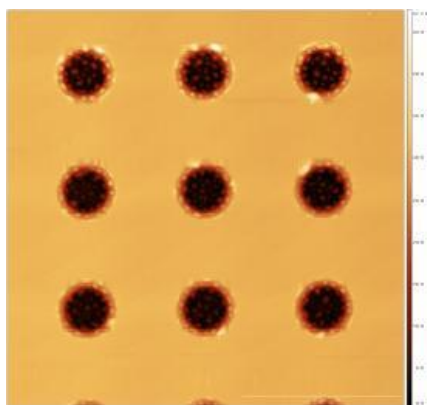
11. Blow dry the substrate with N_2

Figure 3-6 An AFM image of a nanohole-patterned sample with hardened residue around the nanoholes after an unsuccessful cleaning. Oxygen plasma ash performed before solvent cleaning hardened the resist around/inside the nanoholes making it difficult to remove.

Cleaning using the above procedure was required to remove all contamination and residues. Figure 3-6 shows an image of a substrate which underwent an unsuccessful cleaning process, starting when oxygen plasma ashing was performed first. Oxygen plasma ashing before the solvent cleaning hardened the residue and made it more difficult to remove, especially around the nanoholes, even in the following solvent and acid cleaning steps. Figure 3-7 shows AFM images of clean and defect-free nanohole arrays following the *ex situ* cleaning process.
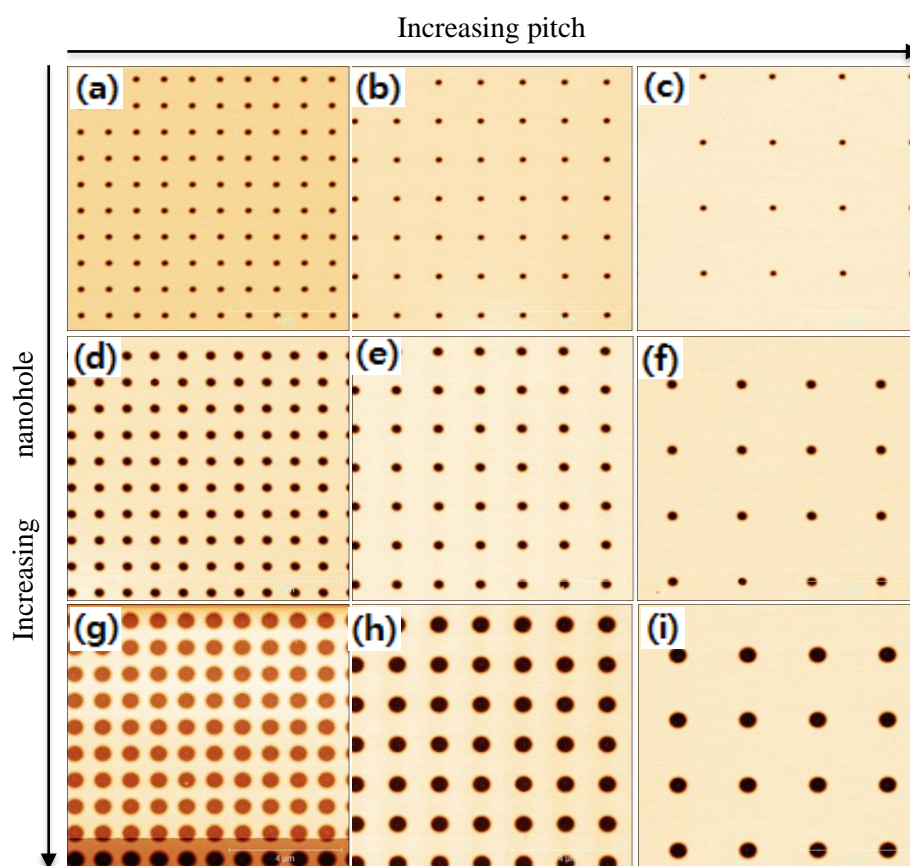
Figure 3-7 AFM images of nanohole arrays after the *ex situ* cleaning process, where nanohole size is increased from 100 nm to 500 nm (top to bottom) while pitch is increased from 1 μm to 2.5 μm (left to right). The scan area is 10 x 10 μm for all.

3.3.2 Secondary Ion Mass Spectrometry (SIMS)

As a highly sensitive surface analysis technique, SIMS is used to identify and quantify atomic and molecular species either on the surface of a solid sample or within it. In SIMS, a beam of primary ion bombards the material to be tested, causing atoms to be ejected and sputtered from the specimen. Part of these detach from the material as secondary ions, which are either positively or negatively charged. A mass-to-charge spectrometer then collects and analyses these sputtered secondary ions. The atomic mass values of the elements are used to identify them, and the number of secondary ions associated with each element is counted to calculate their concentration. Example spectra for the negative and positive modes of bare InP substrate are presented in Figure 3-8. The species present on the surface can be compared by looking at the intensities of each mass before and after the fabrication process. The measurements were

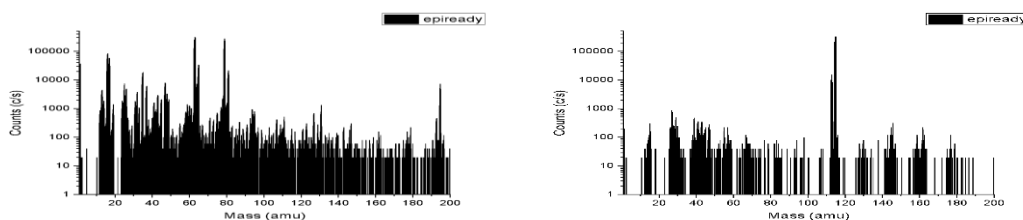performed in collaboration with Dr Aristotelis Trapalis and the data was analysed by the author.

Figure 3-8 SIMS spectra for the negative (a) and positive (b) modes for an n-doped, epiready InP sample

To check the cleanliness of the wafer after nanohole fabrication, the intensity of masses of interest in SIMS spectra has plotted and shown in Figure 3-9. There was a significant increase of sodium and potassium after the fabrication process indicating contamination from moisture or sweat when dealing with the wafer. With the acid cleaning, these peaks are reduced but cannot be completely removed due to their small atomic size. The acid dip also reduced most of the oxide peaks.
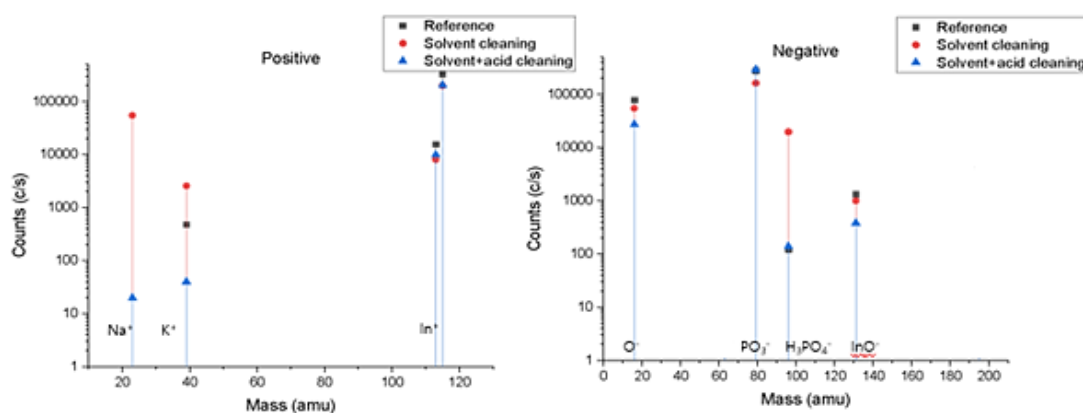

Figure 3-9 SIMS masses of interest for epi-ready (black square), solvent cleaning (red circle), solvent + acid cleaning (blue triangle). Positive spectrum shows nanohole fabrication process increased the contamination of sodium and potassium while negative spectrum shows acid cleaning reduces native oxide.

3.4 Metal-Organic Vapor Phase Epitaxy (MOVPE)

Metal-organic vapour phase epitaxy (MOVPE) is a compound semiconductor-based epitaxial deposition method which utilises chemical reactions in the vapour phase of the metal-organic precursors. MOVPE is also known as metal-organic chemical vapour deposition (MOCVD);

these terms are often used interchangeably. It is a chemical vapour deposition method in which gas-phase precursors approach the vapor-solid interface of a heated substrate to produce crystalline layers [91]. One of the great strengths of MOCVD/MOVPE is its suitability for mass production over other epitaxial technologies, including MBE. It provides not only high speed and low cost but also high-quality epitaxial layers and sharp interfaces with high controllability. Hence, MOVPE tends to be the dominant and most popular growth technique in modern industry, owing to the above advantages.

Technically, the term 'metal-organic material' refers to compounds containing direct metal-carbon bonds such as metal carbonyls or metal alkyls. However, it has broadened to include other metal-containing precursor compounds with metal-oxygen bonds or metal-nitrogen bonds, and even metal hydrides. Typical precursors amongst Group III materials are trialkyl compounds such as trimethylgallium (TMGa), trimethylaluminium (TMAl), or trimethylindium (TMIn), whereas Group V precursors are typically hydride gases, including phosphine (PH_3) and arsine (AsH_3), used as the material in the thin films. In this work, TMIn, PH_3, and AsH_3 have been used as precursors to grow InAs/InP QD system. The simplified chemical reactions during the growth can be written as:

$$In(CH_3)_3 + PH_3 = InP + 3CH_4 \tag{3.3}$$

$$In(CH_3)_3 + AsH_3 = InAs + 3CH_4 \tag{3.4}$$
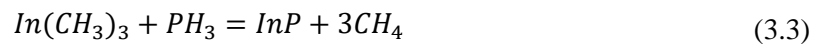
MOVPE processes consist of a set of gas-phase and surface reactions that utilise metal-organic compounds and hydride precursors. The overall reaction of the MOVPE process is illustrated in Figure 3-10. There is a heated layer of gas in vicinity of the substrate called the boundary layer. One significant process during MOVPE deposition is the gas-phase pyrolysis reaction which occurs in this layer [92]. In detail, firstly, precursors evaporate and diffuse into the reactor. Then, these gaseous precursors react near the substrate surface and produce reactive intermediates and by-products. The reactants then go through the process of mass transport to the substrate surface. Some atoms of the reactants are adsorbed onto the surface substrate. Adatom diffusion of surface occurs at growth sites, alongside surface reactions, resulting in the formation of the film. Some of the adsorbed atoms are desorbed once again, transporting the remaining by-products away from the reactor.
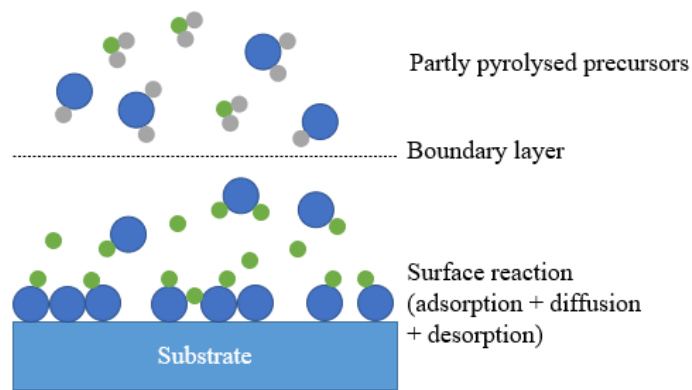
Figure 3-10 Schematic of the epitaxial layer formation process in MOVPE including precursor transport, pyrolysis, and the surface reaction processes [93]

A schematic of a typical MOCVD/MOVPE reactor is shown in Figure 3-11. Wafers are placed on a susceptor, typically made of graphite or molybdenum. The susceptors must have a high thermal conductivity in order to more effectively heat up the substrate to 900 K. They are covered with a special coating to prevent chemical reactions. Since MOVPE is implemented via a chemical reaction, in order to make the chemical reaction take place, it is necessary to have sufficient pressure as well as heat (from the susceptor) to catalyse the decomposition of the gaseous products.
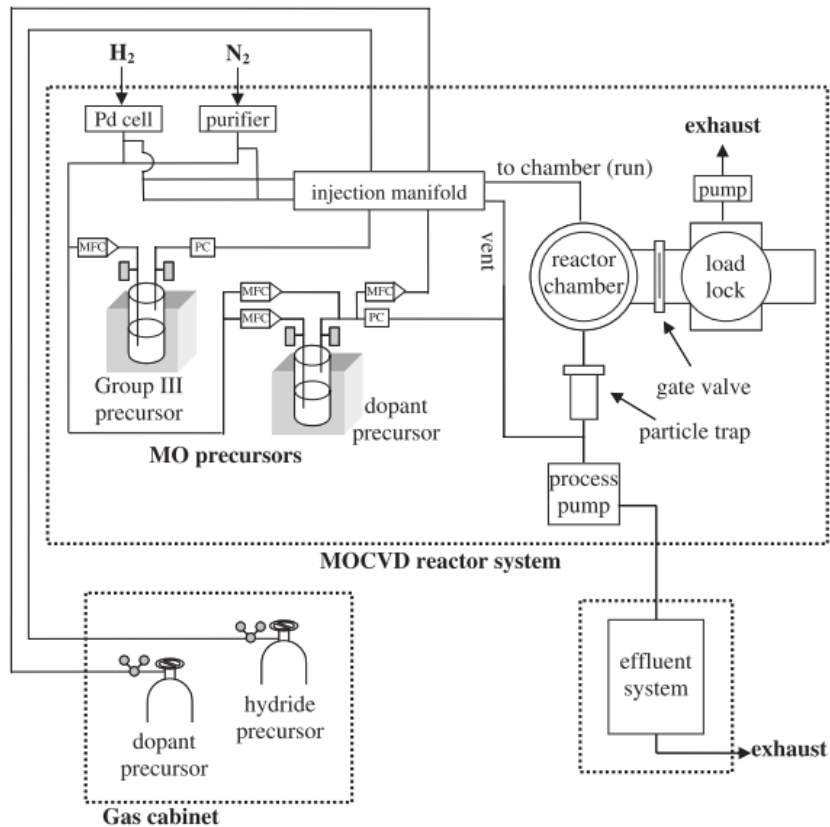
Figure 3-11 Schematic diagram of typical MOVPE reactor [92]

Gas flow into the reactor can be done either in a vertical or horizontal manner; the University of Sheffield possesses both kinds of reactors in the Nanoscience and Technology Building. In a horizontal downstream reactor, direct observation is possible through the window. However, gases are injected horizontally into the reactor which can produce gradients across the wafer and thus a lack of uniformity. On the other hand, for vertical reactors, the gases are injected vertically through uniformly distributed tiny channels on the ceiling of the reaction chamber. Also, there is a rotator under the susceptor operating at 1000 rpm which aids with uniform distribution. For this project, an Aixtron MOVPE machine featuring closed coupled showerhead (CCS) technology with 3x2" wafer capability has been used exclusively to grow the buffers, droplets, and QDs. The MOVPE machine cannot accommodate as many *in situ* characterisation techniques as RHEED (reflection high-energy electron diffraction) in MBE, used to monitor the growth of thin films. Although direct observation is not allowed in vertical reactors, by utilising a laser to probe the substrate surface, it has since become possible to qualitatively assess surface conditions during the growth.

The two main fundamental processes underlying crystal growth are the thermodynamic and kinetic processes. Thermodynamics deals with equilibrium conditions and is the driving force for the overall growth process (feasibility of the reaction), whereas kinetics determines the rates at which the various reaction processes occur. According to [94], quantum dots grown via MOVPE, compared to those grown via MBE, tend to be more uniform and have a lower density at higher temperatures. Ludwig et al. achieved non-positioned QDs with optical linewidths of 1.15 μeV in 2017 [95].
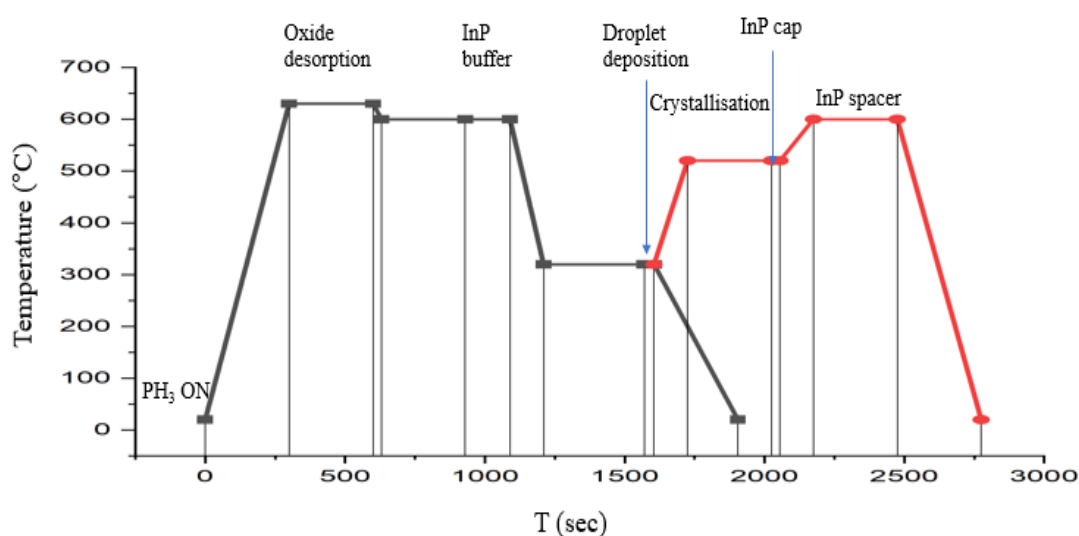

Figure 3-12 Growth sequence of the droplets (black) and QDs (red). Each growth stage is described and correlated with the chamber temperature

Figure 3-12 demonstrates the growth sequence of the droplets and QDs. Growths were performed by Dr Elisa M. Sala in the National Epitaxy Facility in Sheffield. For plain substrate experiments, epi-ready wafers were used therefore no further preparation steps were needed. For patterned substrates, the cleaning steps described in Chapter 3.3.1 were performed prior to loading in the MOVPE chamber. After the wafer was loaded in the chamber, the system was pumped down under N_2 and then the reactor chamber was refilled up to atmospheric pressure. The system was then pumped down again under H_2. Once the reactor pressure reaches 100 mbar, the growth sequence was initiated and the samples were heated to 200 °C when phosphine (PH_3) was introduced to the chamber for sample surface stabilization. The temperature was then further increased to above 630°C for 300 seconds, as measured by an emissivity corrected pyrometer, and left at 630°C for 300 seconds to desorb the native oxide layer. The temperature was then lowered and stabilised to the buffer growth temperature of 600°C. For planar substrates without patterns, a 200 nm InP buffer layer was grown with a

growth rate of 1.2µm/hr and a V/III ratio of 300. The temperature was then lowered and stabilised to the droplet growth temperature (320 °C < T < 400 °C). During the stabilisation, the phosphine flow was cut off to allow the residual phosphine to clear the chamber. Then, indium was deposited, approximately 2ML in total. After the indium deposition, the liquid droplets were given either 60 seconds (for droplet samples) or 30 seconds (for QD samples) to equilibrate. For droplet samples, the substrates were cooled to room temperature and unloaded from the MOVPE chamber. For QD samples, the substrates were heated for the QD crystallisation process under an arsine flow. At 520°C, indium droplets were exposed to the arsine flow and then crystallised into QDs.

For patterned substrates, prior to the patterning process, a 300 nm InP buffer was grown on a bare InP wafer to reduce defect-induced broadening in the growth of SCQDs. Once the nanohole fabrication was finished, the wafer was loaded again into the MOVPE chamber for the droplet or QD growths.

3.5 Characterisation

After the processing and the growth phases, the characteristics of the semiconductor thin films and structures were assessed using various *ex situ* characterisation techniques. No single technique can give an all-encompassing view of every aspect of a particular semiconductor crystal's properties. Therefore, it is necessary to employ complementary knowledge gained from several different techniques in order to fully understand the material. Also, the information gathered from this characterisation is very important to determine if the material being probed is suitable as a particular device component that requires a certain functionality. In this chapter, the semiconductor characterisation techniques that have been used in this project will be briefly reviewed, including SEM and AFM for structural characterisation, and PL for optical characterisation.

3.5.1 Scanning Electron Microscopy (SEM)

SEM is a widely used semiconductor characterisation technique for investigating the physical dimensions of materials and devices. Electrons produced thermionically or through field emission from a tungsten cathode are focused into a very narrow beam by two consecutive condenser lenses. The beam is deflected over the sample surface by two pairs of coils. When the primary electrons collide with the sample, their energy is transferred inelastically to other atomic electrons and the lattice. Part of these electrons leave the surface and are captured by a

detector through variety of random scattering mechanisms. It is usually the secondary electrons that are captured by the detector and they originate from a depth of only a few angstroms. The signal is amplified using a photomultiplier tube amplifier, and the output is utilised to regulate the intensity of a cathode ray tube. SEM can also provide information on the thickness of various layers in a structure by tilting the sample (cross-sectional SEM). Figure 3-13 shows (a) a top view image of a surface of nanoholes fabricated in this work and (b) the nanoholes in cross section with the photoresist on.
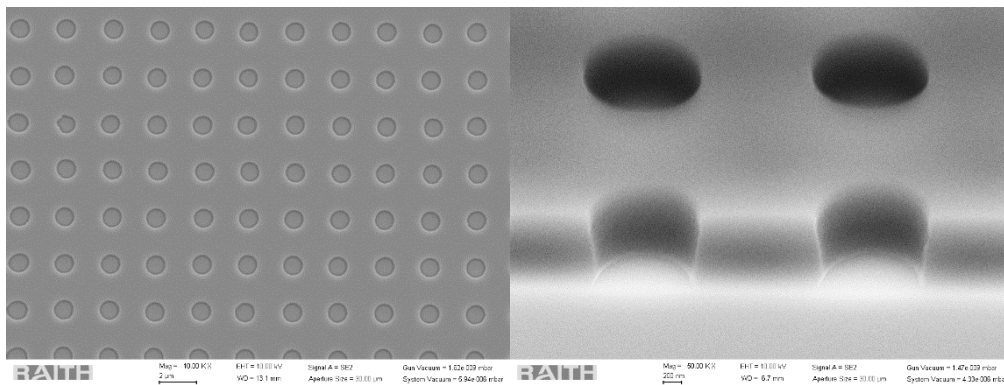

Figure 3-13 (a) Top view of the surface (10 kX) and (b) Cross-sectional SEM image (50 kX) of a nanohole array with the resist on

3.5.2 Atomic Force Microscopy (AFM)

AFM is a kind of scanning probe microscopy (SPM) used to characterise surfaces with high spatial resolution. It is an effective way to study surface morphology without destroying or modifying the object by scanning the object surface using a probe with an extremely sharp tip that has a 2 to 30 nm radius of curvature. Figure 3-14 shows a schematic of an AFM probe and its operating mechanism. An atomic force microscope commonly uses an optical lever to generate a feedback signal. That is, when the tip encounters a particle while scanning the object surface, the degree of bending in the cantilever changes. This causes change in the deflection and so the laser spot position on the position-sensitive photodetectors (PSPD) changes accordingly. This generates an electrical signal to bring the deflection back to the equilibrium position.
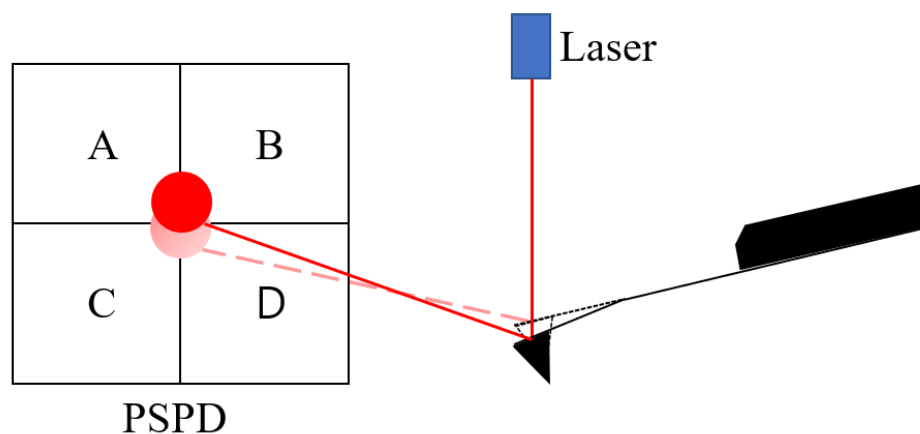
Figure 3-14 Schematic of an AFM tip and its operating mechanism showing the change in laser reflection on PSPD caused by the cantilever deflection

There are two key modes of operation in AFM: contact mode and tapping mode. In contact mode, the probe tip and sample are in perpetual contact during the scan. When the tip encounters a particle, the cantilever is pushed up and vertical deflection increases to generate an error signal. Then, the AFM scanner's z-piezo lifts the cantilever and adjusts vertical deflection to maintain the setpoint. On the other hand, in tapping mode, the tip is oscillated at or near its resonance frequency during the raster scan. When the tip encounters a particle, the amplitude of the cantilever's oscillation decreases. In this mode, the cantilever's oscillation amplitude or phase is used as a feedback signal for imaging. The z-piezo is lifted by feedback and the amplitude returns to the setpoint. In this work, PeakForce Tapping mode, an advanced version of tapping mode developed by Bruker, was used exclusively. In this operational mode, the probe is oscillated well below its resonance frequency so that it can generate a continuous series of force-distance curves where every interaction between the tip and sample can be measured. Therefore, keeping the peak force between the tip and sample constant enables this mode to directly control the tip-sample force at a known low value. Therefore, it is possible to operate with much lower forces, making this operation inherently more stable and gentle on samples.

A Bruker ICON AFM in PeakForce Tapping mode was used with an SNL10 probe. This probe was chosen due to its extremely high resolution owing to its supersharp tip (2 nm radius) and low spring constant (0.35 N/m) and the high sensitivity of the silicon nitride cantilever. The software package NanoScope Analysis v1.50 was used to extract and analyse the data, in addition to the software package Gwyddion.

The AFM can reconstruct the surface morphology and produce a 3D image of the surface topology of the materials with atomic-scale precision. A typical example of a 3D AFM image of the surface of InAs/InP QDs grown via droplet epitaxy in MOVPE is shown in Figure 3-15, below.
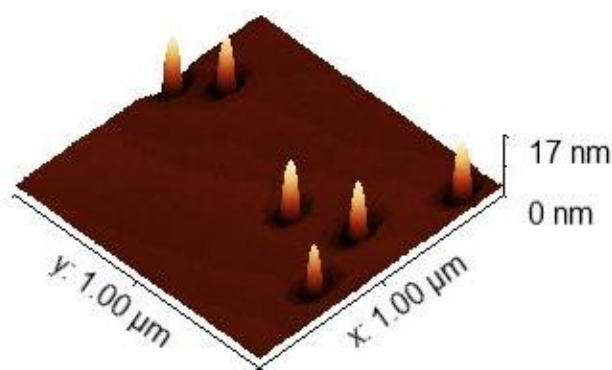

17 nm

0 nm

y: 1.00 μm

x: 1.00 μm

Figure 3-15 A 3D AFM image of InAs/InP QDs grown via MOVPE droplet epitaxy

A closed loop positioning stage, called the Programmed Move function, enables reproducible movements to a set of specific locations on the sample using memorised coordinates. This function is particularly useful for monitoring changes in surface and individual nanohole profiles at each stage of the process. The stage will move to each location in sequence, relative to the current origin. To scan the same area for comparison at different stages, alignment marks were integrated into the sample design and, for every scan, it was restored to the original point of origin to identify the same regions on the sample.

3.5.3   Photoluminescence (PL) Spectroscopy

Photoluminescence (PL) spectroscopy is a contactless and non-destructive technique for determining the optical characteristics of semiconductor materials. This method uses a mechanism called photo-excitation in which light focused upon a sample is absorbed. With the extra energy generated by photo-excitation, electrons can hop to excited states. The surplus energy is lost in various ways when these electrons return to their equilibrium states. Emissions of light with energies equivalent to the energy difference between the equilibrium and excited states is one way in which this energy is lost. This generated light is collected and focused by a photon detector after which it travels through a spectrometer.

PL spectra may provide a lot of important information, such as bandgap determination, impurity levels and defect identification, and information about the recombination process and material quality. In semiconductors, the most common radiative transfer occurs between the conduction band and the valence band. This is generally shown as the peak wavelength of PL spectra and equals the semiconductor's energy gap. PL spectra may also be used to detect impurity levels and defects. Because localised impurity/defect levels are involved in radiative transitions in semiconductors, the photoluminescence energy associated with these levels may be utilised to detect certain defects.

Recombination is the process through which energised electrons revert to their equilibrium states. During recombination, both radiative and non-radiative processes can occur. The intensity of the PL peak, as well as its dependency on photo-excitation and temperature can be used to determine the main recombination mechanism. PL can also be used to assess a material's quality. A PL spectrum's high intensity and narrow line width (FWHM) show the material's quality, whereas the presence of defect-related peaks reveals flaws in the epitaxial layer.

A room-temperature photoluminescence (RTPL) instrument and a micro-photoluminescence (µPL) instrument were used to study the optical properties of the QDs. An RTPL instrument was used to generate maps of many characteristics of the full wafers by measuring optical luminescence emissions from the samples at room temperature. All samples were measured sequentially with the same settings, using an excitation HeNe laser at 645 nm with a power density of ~85 Wcm^{-2} and an InGaAs detector whose detection range extends up to 1650 nm. However, at room temperature, carriers can thermally escape to higher energy levels resulting in other peaks. Also, at room temperature, there is an expectation of a strong reduction in the intensity of the PL signal due to there being sufficient energy to reach non-radiative recombination centres.

For a more detailed analysis, a µPL instrument was used to get clearer readings from individual QDs. At low temperatures, carriers are effectively frozen allowing the lowest energy state to be clearly observed. For the measurements, the samples were first cleaved into squares 3-4 nm in size from the centre of the wafer and loaded into the cryostat. Then, the cryostat was purged and pumped to allow nitrogen to flow in. Once the cryostat pressure fell to $1.0 \times 10\text{-}4$ mbar, the cryostat cooled down to 4 K. RTPL and µPL spectra for an InAs/InP QD

sample is shown in Figure 3-16. The µPL measurements were performed in collaboration with Dr Aristotelis Trapalis and Max Godsland.
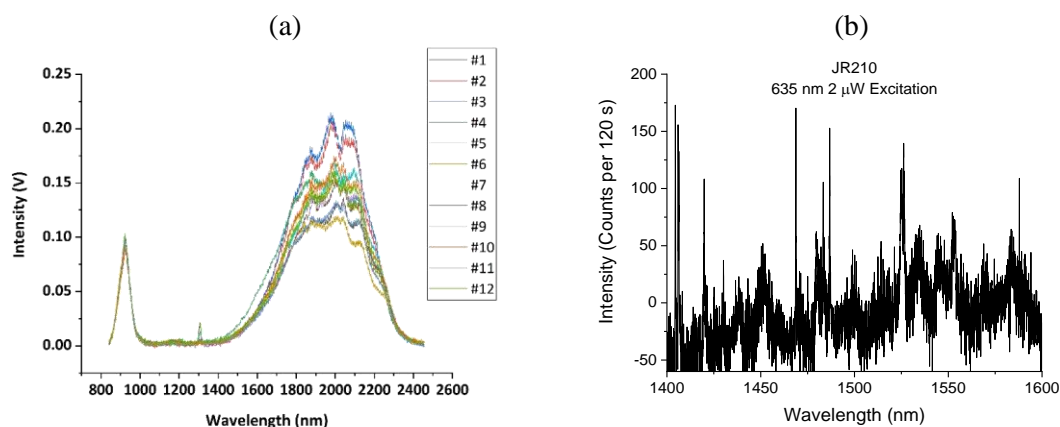

Figure 3-16 (a) RTPL spectra measured in 12 different locations of 2-inch wafer and (b) µPL spectrum of InAs/InP QDs grown via droplet epitaxy showing sharp lines characteristics of emission from individual quantum dots of Figure 3-15

This project has used a confocal μPL set-up, available in the research group a schematic of which is shown in Figure 3-17. The sample is excited and its photoluminescence is collected through the same optical path using confocal microscopy. The measurement set-up additionally includes a white light source and CMOS camera to illuminate and detect the desired position of the sample. The µPL experiment was carried out using a 635 nm laser as an excitation source, and spectrometer with a resolution of 25 µeV. A typical laser excitation power of ~1μW was used and the corresponding power density was calculated to be ~4.5 Wcm^{-2} with the spot size of ~5 μm. The laser beam travels through a neutral density filter to adjust its power. And then, beam splitters directs the beam into the objective, where it is focused on the sample. The photoluminescence from the sample is then collected by the objective and collimated and directed towards the spectrometer with a InGaAs detector. The spectrometer used throughout the project is the SpectraPro SP-2750 from Princeton Instruments which is a 750 mm focal length monochromator/spectrograph. In this study, the acquisition time of 120 seconds and a 1200 lines/mm grating were used.
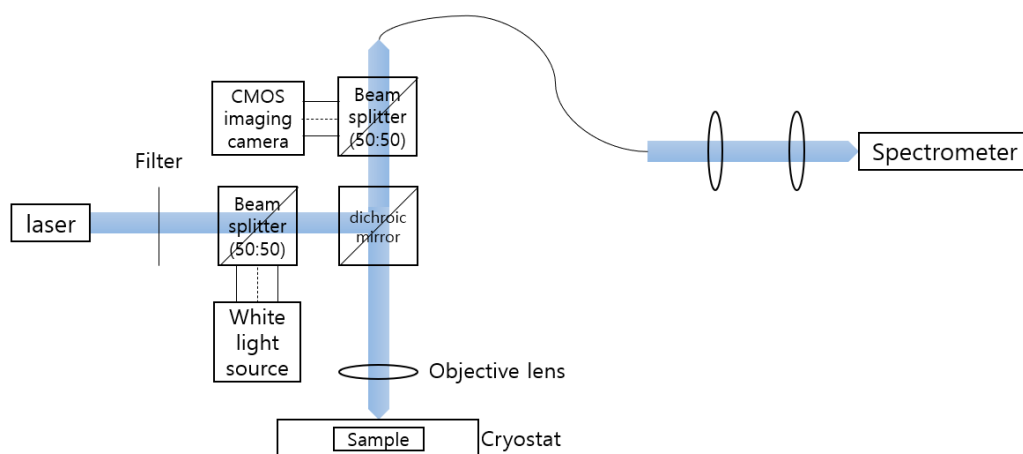
Figure 3-17 . A schematic of the confocal μPL set-up used in this project

4 In droplets & InAs QDs on un-patterned InP

4.1 Indium droplets on un-patterned InP

For QDs, their size and density are the two main factors which affect their optical and electrical properties; their size determines the wavelength of the light they emit, and their density affects the potential applications in devices. High-density QDs are used for lasers while low-density QDs are used for single photon sources. Therefore, it is important to have the ability to control the size and density of dots in the epitaxial process or in whatever fabrication methods are used. One of the advantages of DE is the ability to control the size and density of QDs individually across a large range of values. DE consists of two stages: the formation of a metallic droplet and its subsequent crystallisation into a quantum dot. The first step, the droplet formation, should clearly have an impact on the quality and properties of the final QDs as the formation of the QDs originates from the crystallisation of droplets with controlled growth parameters. Since the droplets on the surface will serve as the Group III localised sources from which the QDs will evolve, it is important to investigate and understand the phenomena occurring during the droplet formation. Experiments to control the size and density of indium droplets – the precursors of QDs – have been done and the results are discussed in this chapter. In this work, four primary means of controlling droplet size and density were investigated: growth temperature, deposition time, metal organic flow rate, and growth interruption (GRI). For each sample, four images of 5 μm^2 AFM images were taken in order to investigate the variation across the wafer. The images produced were then used to measure the average density and size of the droplets. For the measurements, the grain analysis function of the software Gwyddion has been used to extract the characteristics of droplets (density, radii and height etc). This information was cross-checked by counting the number of droplets manually for density measurement and by extracting line profile of a droplet for size

measurement. To analyse the data, mean values were used however standard deviation was extracted and represented as error bars in the graphs. The droplet samples discussed in this chapter were grown following the growth sequence described in Figure 3-12. A list of the samples and their growth parameters are shown in Appendix A.

4.1.1   Temperature series

Temperature during the indium deposition stage was chosen as the first growth condition to be varied because it is considered to be the most influential factor affecting the deposition process due to its effect on decomposition and adatom mobility on the surface. Following the growth sequence in Figure 3-12, a 300 nm thick InP buffer layer was grown at 610°C. The substrate temperature was then reduced down to the indium deposition temperature. JRxxx in the text (with x being a number) refers to the sample number. For this experiment, the substrate temperature was varied between 300°C and 400°C whilst trimethylindium (TMI) was allowed to flow into the reactor chamber and pyrolyse to form liquid indium droplets. Other growth conditions were kept the same: TMIn supply time = 35 s, TMI flow = 20 SCCM, and GRI = 30 s. Even though the indium deposition time and flow were kept the same, the total amount of indium deposited on the substrate may vary depending on the temperature because of its effect on the thermodynamics and kinetics of growth and the strong temperature dependence of TMI pyrolysis in this temperature range. Figure 4-1 shows the decomposition level of TMIn with different carriers.
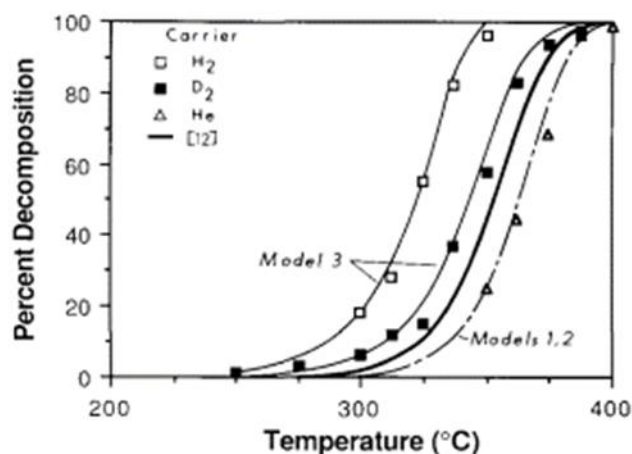

Figure 4-1 Decomposition level of TMIn with three different carriers. Reprinted with permission from N. I. Buchan, C. A. Larsen, and G. B. Stringfellow, "Mass spectrometric studies of trimethylindium pyrolysis," *Journal of Crystal Growth*, vol. 92, no. 3–4. pp. 591–604, 1988. [96]

AFM investigation confirmed this (Figure 4-2). There was no formation of any indium droplets at 300°C; droplets were first observed at 320°C, meaning that the critical temperature for droplet formation is between 300°C and 320°C. It does not necessarily mean that TMI was not pyrolysed at all at this temperature. According to [96], pyrolysis of TMIn in H_2 is complete at or above 350°C and nearly impossible at or below 250°C. Between 250°C and 350°C, the growth rate is limited by the chemical reactions at the interface according to the Arrhenius equation:

$$k = Ae^{\frac{-E_A}{RT}}$$

Where E_A is an activation energy which characterises the chemical reactions.

That is, with H_2, TMI is fully decomposed above 350°C, while below 350°C, the decomposition level decreases with an activation energy of 39.8 kcal/mol. In addition, Akchurin et al. [71] found that the presence of a GaAs surface, acting as a catalyst, lowers the activation energy of TMI decomposition down to ~9 kcal/mol. It should also be noted that the total amount of deposited material and the droplet volume is not always the same because the first few layers of indium are consumed to wet the substrate. After the buffer growth, the substrate is generally terminated with Group V (P) atoms due to their strong binding energy vis-à-vis the substrate. The first ML of deposited indium transforms the surface from the P-rich to the In-rich configuration rather than contributing to the formation of indium droplets [64]. Comparing the surface morphology using AFM images of the InP buffer layer and the surface of JR151 (Figure 4-2), RMS surface roughness was found to increase from 150 pm to 230 pm after the indium deposition at 300°C; this is associated with the surface wetting process.
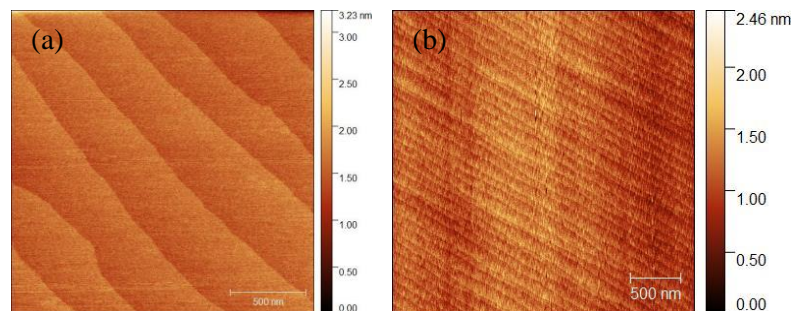

Figure 4-2 AFM image of (a) an InP buffer (2x2 µm) and (b) indium deposition at 300°C (JR151) (5x5 µm). The RMS surface roughness was increased but droplets are not formed at 300°C.

Figure 4-3 shows a series of AFM images of indium droplet samples as a function of deposition temperature. Three samples of indium droplets were grown at three different temperatures (320, 350, 400°C). The images show increasing droplet size and decreasing droplet density as a result of increasing temperature. The droplets grown at 400°C have dimensions of (160±5) nm for the width and (35±2) nm for the height at a density of $7.6*10^7$ cm^{-2} while the droplets grown at 320°C have dimensions of (35±3) nm for the width and (8±1) nm for the height at a density of $2.2*10^9\,cm^{-2}$. On the other hand, the droplets grown at 350°C shows a bimodal distribution with diameters of (130±5) and (70±5) nm and a height of (20±2) and (10±1) nm at a density of $3.0 *10^8$ cm^{-2}. The contact angles of the indium droplets, which represents the wettability of indium on the InP substrate, are 34.9±3.14°, 30.1±6.57°, 24.6±2.07° for temperatures of 320, 350, 400°C, respectively, when measured using AFM. That is, the wettability increases as temperature increases. This decrease in contact angle with increasing temperature is consistent with results demonstrated by Konig et al. [97]. The contact angles obtained in this work are relatively smaller than the values in the literature. This is because the InP surface decomposes and change its stoichiometry during the oxide desorption process.

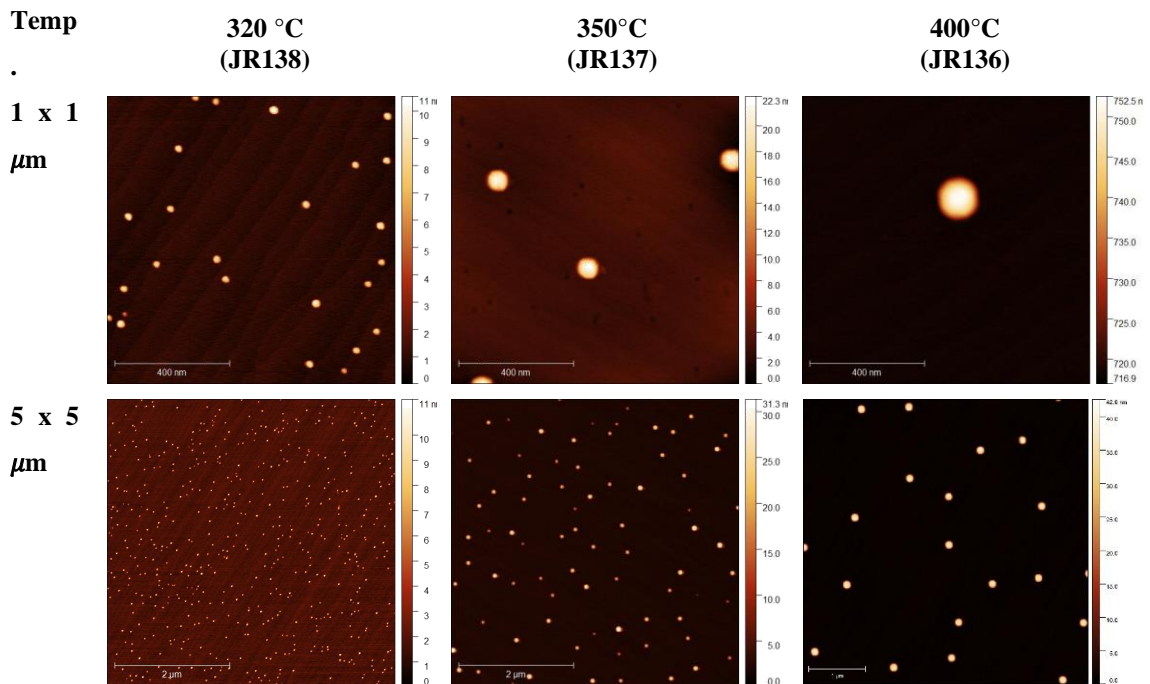| Temp.	320 °C (JR138)	350°C (JR137)	400°C (JR136)
1 x 1 µm			
5 x 5 µm			

Figure 4-3 A series of AFM images of the indium droplet samples showing increased size and reduced density of the droplets by increasing the temperature

Figure 4-4 shows an example of how to measure contact angle of the droplets. Firstly, with the profile command in Gwyddion, XY coordinates of the line profile were extracted and plotted in a graph. The inset shows a zoom for the point where droplet line and the substrate surface meet. It indicates the transition of the slope having each measurement point 2 nm apart. The AFM tip 'SNL10' which has been used throughout the project has a 2nm of radius and a 15° of front angle which can theoretically measure up to 85°. By using the supersharp tip, the level of uncertainty was minimised.
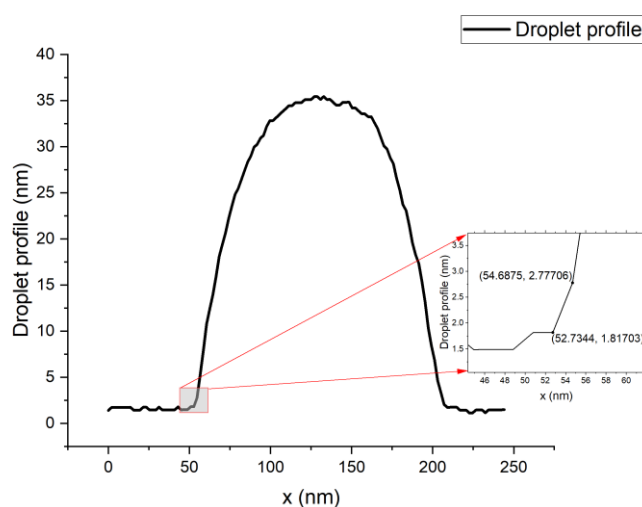
Figure 4-4 A line profile of a droplet with a inset of a zoom at transition point showing the measurement method of contact angle

At or above 320°C, after the first indium ML is consumed to wet the substrate, the surplus indium forms indium droplets on the semiconductor surface via the Volmer–Weber growth mode. Figure 4-5 shows droplet density as a function of temperature, while Figure 4-6 shows droplet size trends versus temperature. The density of indium droplets is highly influenced by the substrate temperature, as previously demonstrated by Lee et al. [98]. With decreasing temperature, droplets get smaller with higher density, while increasing the temperature leads to bigger droplets with lower density. The temperature-dependent surface diffusion coefficients of adatoms can explain the temperature dependence of droplet density and size. At higher temperatures, with the large diffusion length of surface adatoms, the droplets begin to coalesce and merge to form bigger droplets rather than contributing to further depositing of thin films due to the stronger binding energy in the droplet. This drastically reduces the number of clusters.

Thus, the droplet density fell substantially as the substrate temperature increased. At high temperatures, the density of droplets does not follow a classical nucleation scaling law but rather coarsening by Ostwald ripening, as seen in previous work [64]. The driving force behind Ostwald ripening is the surface energy of the particles; thermodynamically, at the same temperature, small particles have a large surface energy per unit mass, while large particles do not. As a result of this difference, the solubility of small particles becomes greater than that of large particles. Hence, large clusters grow at the expense of smaller ones, and causes a

decrease in the total density. In contrast, at low temperatures, the nucleation of a new stable cluster with a number of atoms exceeding the critical size is more likely because the mobility of indium adatom is low. Coalescence only occurs when the diffusion length is of the order of the mean distance between the neighbouring droplets.
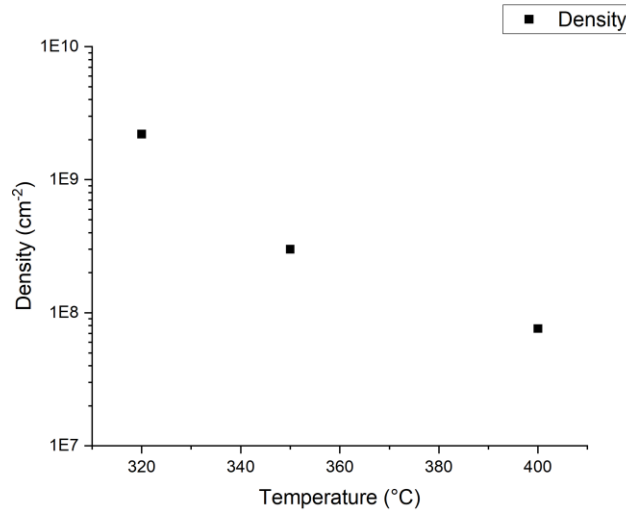

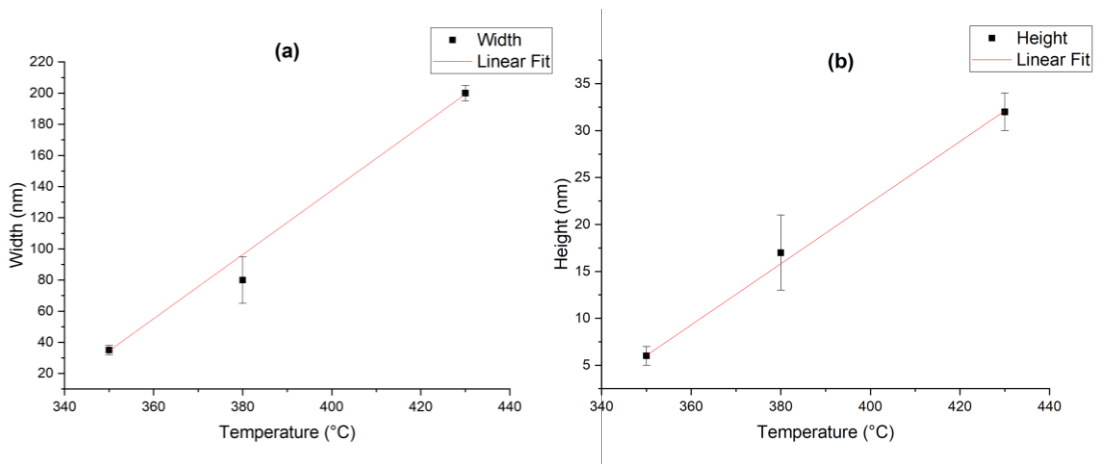Figure 4-5 A plot of indium droplet density as a function of droplet deposition temperature

Figure 4-6 (a) width (b) height of the droplets as a function of droplet deposition temperature (The linear-fit lines are added as a guide to the eye)

Assuming the droplets are oblate spheroids, the volume of a single droplet can be calculated with the values of diameter and height.

$$Volume\ of\ a\ single\ droplet = {}^{2}/_{3}\,\pi * radius^{2} * height$$

With the droplet density, the volume of indium droplets per square centimetre can be calculated.

$$Indium\ droplet\ volume\ per\ cm^2 = single\ droplet\ volume * density$$

The volume of a single droplet varies significantly depending on temperature. There is also a slight decrease in total droplet volume due to the incomplete pyrolysis of indium at low temperatures. In addition, it is possible that the difference in temperature leads to a different phase of In-rich reconstructions and, in turn, differing amounts of indium consumed in wetting the surface. This may provide an explanation for the discrepancies in the literature regarding the minimum amount of indium required to form droplets at the same temperature [98].

Table 4-1 Indium droplet volume calculation at different deposition temperatures

	Averaged volume of single droplet (nm^3)	Indium droplet volume per cm^2 (nm^3/cm^2)
JR136 (400°C)	$6.06*10^5$	$4.60*10^{13}$
JR137 (350°C)	$1.01*10^5$	$3.06*10^{13}$
JR138 (320°C)	$8.40*10^3$	$1.86*10^{13}$

Control over droplet size is critical to engineering the crystallisation process in DE. Large droplets deposited at high temperatures are enlarged during the crystallisation process by adding more material (As), but this creates defects rather than QDs. Figure 4-7 shows the crystallisation of droplets grown at 350°C (a) and 430°C (b) under otherwise identical crystallisation conditions. The crystallisation of the larger droplets at 430°C has led to large InAs crystallites around 800 nm in width and 130 nm in height. Clearly these are not 'quantum dots' since electronic confinement of carriers can only occur if the material dimension is comparable to the order of the de Broglie wavelength. Therefore, the droplet deposition temperature is critical for fabricating desirable QDs. However, the problem here is that with temperature, the density and size cannot be controlled independently. To achieve the low density of QDs required for quantum photonics applications, other growth conditions which control density without affecting the size should be investigated.
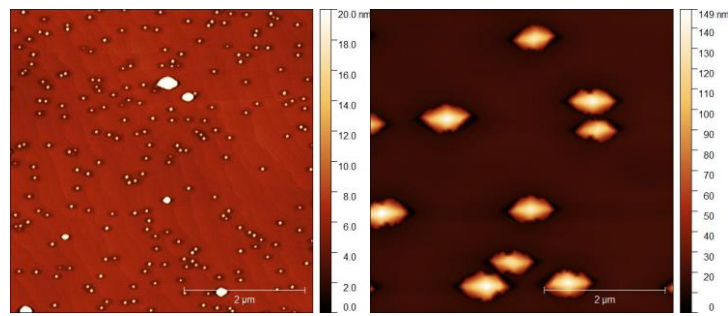
Figure 4-7 AFM images of the crystallised droplets deposited at (a) 350°C and (b) 430°C with the same crystallisation process. Droplets deposited at 350°C are transformed into QDs and droplets deposited at 430°C became large crystallites.

4.1.2 Indium deposition time series

The second growth parameter chosen to be varied is the indium deposition time. Other growth parameters were kept the same, as follows: temperature = 320°C, TMIn flow = 20 SCCM, GRI = 30 s. The indium coverage can be considered to be directly proportional to deposition time indium coverage if the pyrolysis rate is 100% or at least if it does not change with indium accumulation on the surface (for instance, as might occur due to catalysed pyrolysis). Unlike MBE, it is difficult to calculate the exact amount of indium deposited since the sources are alkyls or hydrides which should go through the decomposition process. However, considering a TMIn flow of 20 SCCM and a deposition time of 35 seconds, it is expected that approximately 2ML is deposited in total. The influence of indium deposition time on the density and size of the droplets is shown in Table 4-2 and Table 4-3, which include AFM images of the droplets formed. Indium deposition time was varied from 20 seconds to 40 seconds, with nine specific times, namely: 20, 20.8, 21.5, 22, 22.5, 25, 30, 35, and 40 seconds. From 20 to 25 s, small steps were incorporated as a small change in deposition time leads to a dramatic change in droplet density. No droplet formation was detected at 20 seconds so the critical value for the onset of indium droplet formation is between 20 s and 20.8 s.

Table 4-2 AFM images of indium droplets with different indium deposition times (saturation regime)

Indium time	25 s (JR350)	30 s (JR146)	35 s (JR138)	40 s (JR148)
1X1μm^2				
Density	1.06*10^9 cm^{-2}	2.19*10^9 cm^{-2}	2.22*10^9 cm^{-2}	2.40*10^9 cm^{-2}
Size	Width: ~(31±8) nm Height: ~(7±1) nm	Width: ~(30±5) nm Height: ~(7±1) nm	Width: ~(33±6) nm Height: ~(8±1) nm	Width: ~(33±6) nm Height: ~(8±1) nm

Table 4-3 AFM images of indium droplets at different indium deposition times (exponential increase regime)

Indium time	20.8 s (JR359)	21.5 s (JR358)	22 s (JR360)	22.5 s (JR352)
5X5μm^2				
Density	8.0*10^6 cm^{-2}	2.0*10^7 cm^{-2}	2.0*10^8 cm^{-2}	3.16*10^8 cm^{-2}
Size	Width: ~(60±7) nm Height: ~(13±1) nm	Width: ~(50±3) nm Height: ~(10±1) nm	Width: ~(42±6) nm Height: ~(9±1) nm	Width: ~(44±6) nm Height: ~(8±1) nm

Figure 4-8 shows dependence of the (a) density, (b) width, and (c) height of the droplets as a function of indium deposition time. From 20.8 s to 25 s, there is a dramatic increase in density by two orders of magnitude from $8.0*10^6$ cm^{-2} to $2.40*10^9$ cm^{-2}, whereas both the width and height change by only a factor of two. By further increasing the deposition time, it was found that the droplet density was saturated in between 25 s to 40 s. Droplets in this range have reasonably similar dimensions of ~30 nm in width and ~8 nm in height, and a density of ~$2*10^9$ cm^{-2}.
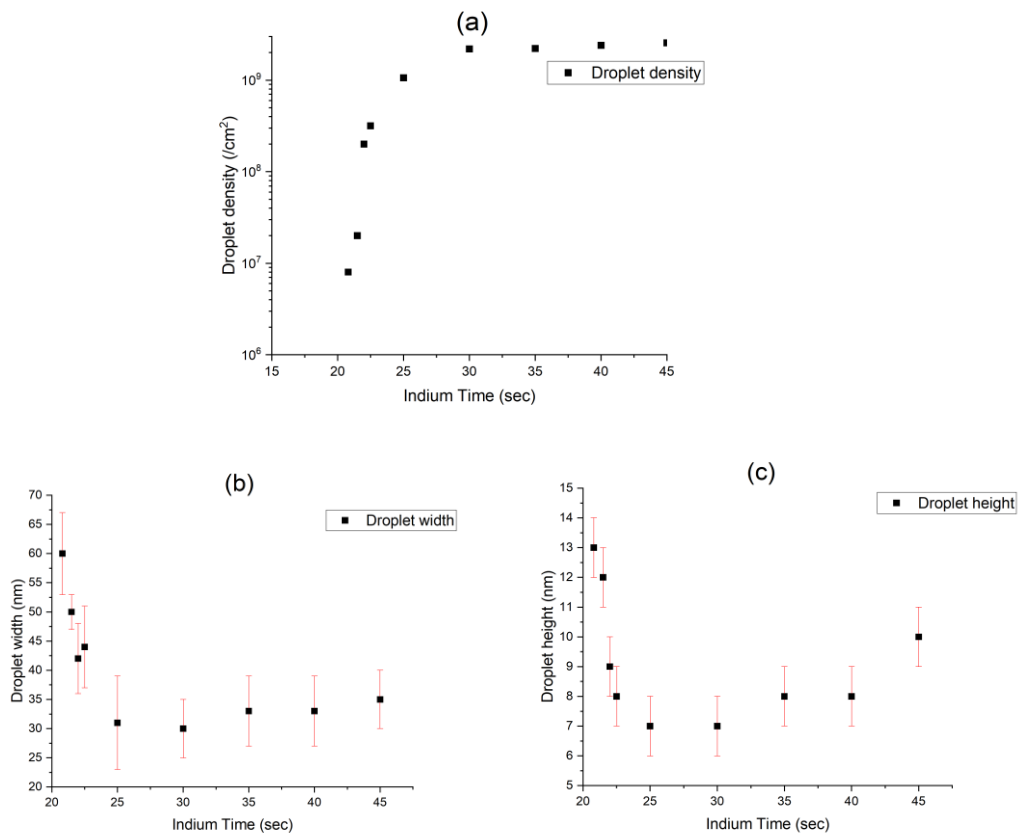

Figure 4-8 Droplet (a) density, (b) width and, (c) height as a function of indium deposition time showing drastic increase in density and decrease in size from 20 to 25 s and the saturation beyond 25 s.

In quantifying the effect of deposition time, the change in density was noted to be bigger than the change in size. We have successfully crystallised the droplets grown with indium deposition times of 22.5, 25, 30, 35 s with an identical crystallisation process. These QDs clearly show single dot emission although their emission wavelengths differ due to the size difference. The crystallisation and their PL emissions will be discussed in a later section.

Figure 4-9 shows the total droplet volume as a function of indium deposition time. From 22s to 40s, the total indium droplet volume increases linearly as the indium deposition time linearly increased. From this, it can be surmised that most of the deposited indium is incorporated to form droplets. However, below 22s of deposition time, the total droplet volume is significantly lower than predicted with the linear fit. It is believed that, in this range, the surface is not homogeneously wet and some of the indium material deposited is still consumed in wetting the surface before forming droplets. At the deposition time of 40 seconds, total indium volume saturates even though indium deposition time is increased. This is because, if too much indium is deposited, the excessive indium material does not incorporate with droplets but is instead "floating" in between. This was confirmed by the observation of large indium arsenide features appear in the holes when crystalising localised droplet.
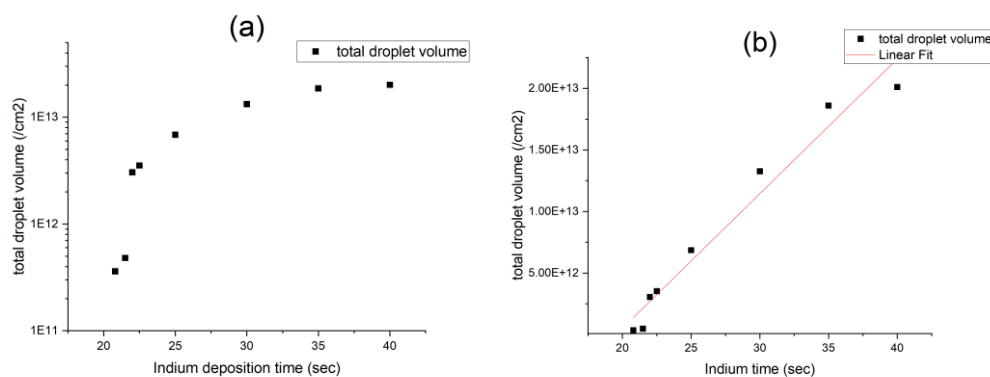

Figure 4-9 Total indium droplet volume as a function of deposition time in log scale (left) and linear (right). Droplet volume per cm^2 was calculated using the equation in page 42.

It is one of the most important aspects of DE to have the ability to individually regulate the size and density of droplets across a large range of values. True independence in the control of density and size cannot be achieved solely by regulating indium deposition time. However, indium flow and GRI are additional parameters by which to control size and density independently, which will be discussed in the next section.

4.1.3   Indium flow series

The third parameter to be varied is indium flow with other growth conditions kept the same: temperature = 320°C, TMIn supply time = 35 s, GRI = 30 s. Figure 4-10 shows AFM images of indium droplets deposited with different indium flows: 10, 20, 65, and 110 SCCM. The figure shows that the droplet density has a very weak dependence on indium deposition flow

while the droplet size is affected. No droplets were formed at 10 SCCM meaning critical indium flow for the formation of indium droplets is in between 10 and 20 SCCM. Figure 4-11 shows the dependence of the (a) density, (b) width, and (c) height of the droplets as a function of indium deposition time. By raising the indium flow, the dimensions of droplets increased linearly from (33±6) to (45±9) nm in width and (8±1) to (13±2) nm in height while maintaining a density level of ~$2*10^9$ cm^{-2}.
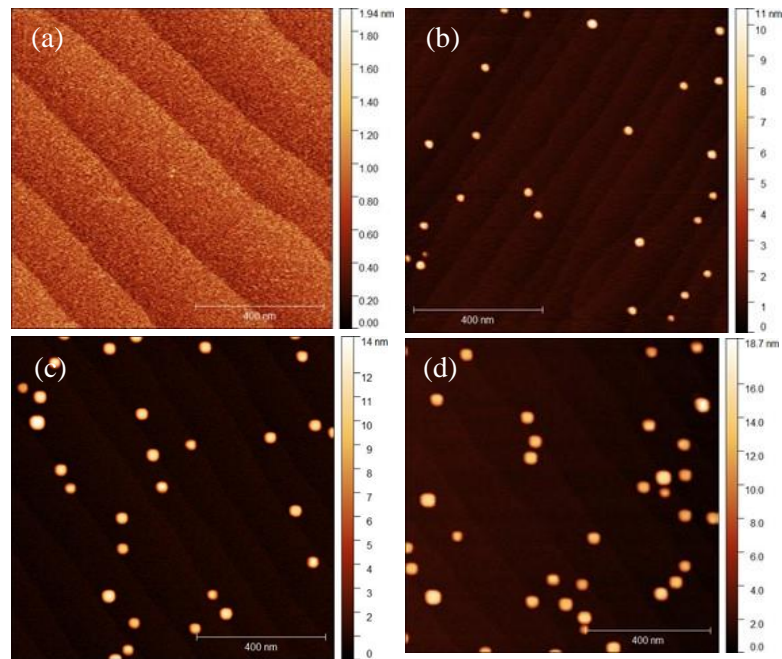

Figure 4-10 AFM images of indium droplets with the indium flow of (a) 10, (b) 20, (c) 65, (d) 110 SCCM. The scan area is 1 x 1 μm for all. No droplet formation is seen at indium flows of 10 SCCM. Droplets start to form from 20 SCCM and their size gets bigger with flow.

This parameter has not been further explored in this project. However, it will be a useful parameter when there is a need to control droplet size without affecting density. By combining the effects of indium deposition time and flow, true independence in the control of the density and size can be achieved. For instance, in future work, droplets can be deposited at a slightly higher temperature with a reduced indium flow. Also, it would be interesting to do the same experiment with a lower indium deposition time. As discussed earlier, the indium already saturates at 35 seconds. Different results could be obtained when it is tested with a lower indium deposition time. By comparing the indium time and flow series, we believe the two experiments are consistent. For example, 35 seconds at 10 SCCM could be considered equivalent to half the time (17.5 seconds) at 20SCCM. In fact, no droplet formation is

observed at 17.5 seconds. However, it has to be confirmed by exploring in the non-saturated regime.
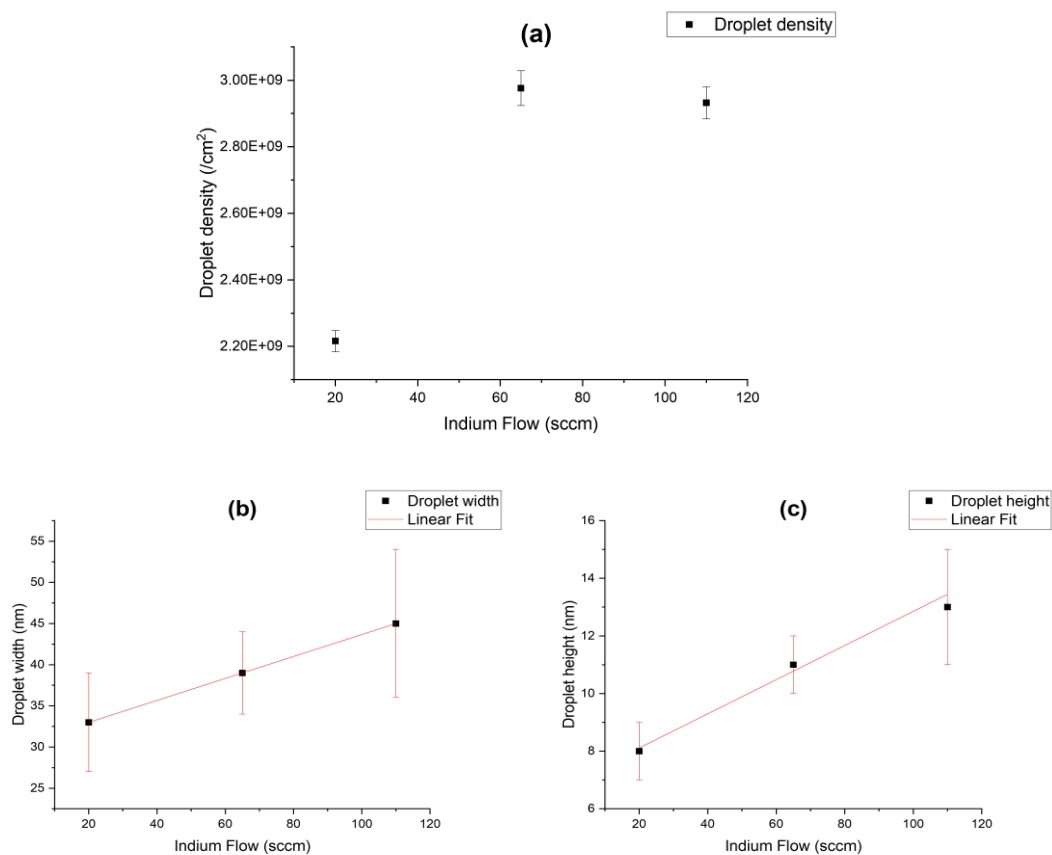

Figure 4-11 Droplet (a) density, (b) width and, (c) height as a function of indium flow. A linear dependence of droplet size and indium flow was found.

4.1.4 Growth Interruption (GRI)

The fourth parameter controlling droplet formation is the growth interruption time (GRI), which refers to the time between droplet deposition and the introduction of arsine for crystallisation. The deposited indium droplets were left at the deposition temperature for different amounts of time (30, 60, and 90 s) while the other growth parameters were kept the same: temperature = 320°C, TMIn supply time = 35 s, In flow = 20 SCCM. The GRI will clearly allow indium atoms to diffuse and attach to an existing stabilised cluster. That is, the longer the GRI is, the more the indium moves around and merges together, forming bigger droplets at lower densities.
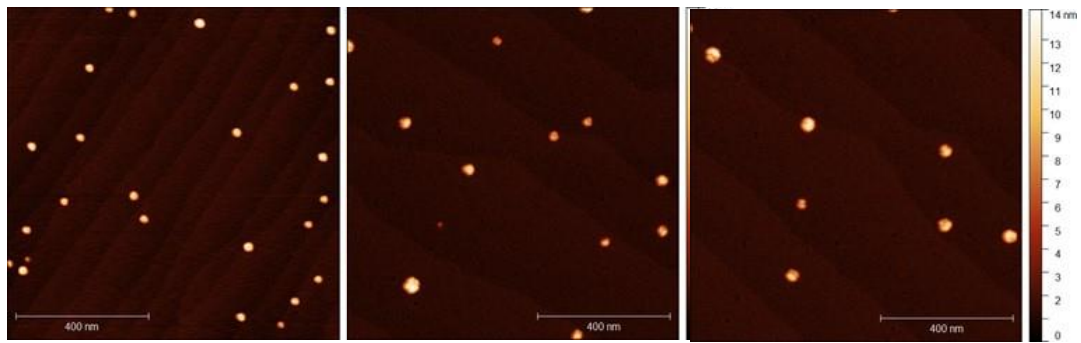
Figure 4-12 AFM images of indium droplets with the GRI of (a) 30 s, (b) 60 s, and (c) 90 s

However, at the same time, a higher GRI accelerates the creation of droplets of different sizes. A possible reason for that is when the transition to In-rich reconstruction is not completed all over the substrate at the same time, due to low indium atom migration length, it could lead to the nucleation of droplets at slightly different moments and, in turn, accelerate more inhomogeneous nucleation, by region. The plot of the size dispersion as a function of GRI is shown in Figure 4-13. The size dispersion is represented as relative standard deviation:

$$Size\ dispersion\ (\%) = relative\ standard\ deviation * 100 = \frac{SD}{mean\ value} * 100$$

With a GRI of 90 s, inhomogeneity in the droplets increases, and the size dispersion significantly increases. In DE, the size dispersion of the indium droplets is an important aspect as the homogeneity of InAs QDs is essentially determined by the dispersion of indium droplets. A large dispersion is an undesirable aspect of droplet formation because a large distribution of droplets gives rise to a large distribution of QDs, in turn resulting in a broad PL emission.
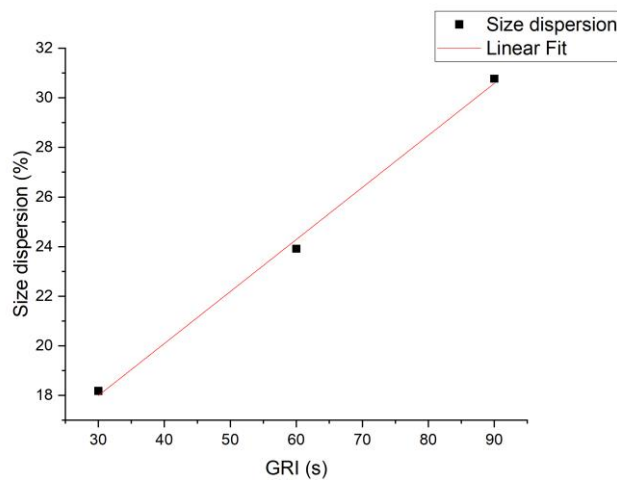

Figure 4-13 Size dispersion of In droplets as a function of GRI with a linear fit

4.1.5   Summary

From the series of experiments presented in this chapter, the effects of each growth parameter on droplet density and size were investigated. From the temperature series, it was found that droplet density and size are strongly affected, and affected simultaneously by temperature. By increasing the temperature, the droplet density decreases while their size increases and this is well understood in terms of the increased diffusion of indium on the surface and the simultaneous presence of Volmer-Weber and Otswald ripening effects. From the indium time series, a strong effect on droplet density was observed but with a limited change in droplet volume. In the range of 22.5-35 s, control of density by two orders of magnitude was achieved while affecting the size very little (a factor of two, only). On the other hand, indium flow was found to manipulate droplet size without affecting density, although we only competed this analysis in the saturation regime of indium deposition time. By using a shorter GRI, it was also then possible to minimise the size dispersion of droplets. Finally, it was found that only droplets grown at 320°C produce QDs emitting at the desired wavelengths around 1550nm. From the experiments indicated, at 320°C, it was found that the maximum density was around $2*10^9$ cm^{-2} whereas the minimum density of $8.0*10^6$ cm^{-2} was achieved by manipulating the indium deposition time. Achieving a low density is important for photonic devices in which the QDs are utilised as a single photon source. Independent control of droplet size can then be obtained by manipulating the indium flow. Lastly, a longer GRI decreases density but creates a multi-modal distribution of droplet sizes at the same time. The GRI was set to 30 seconds to avoid large size dispersion. To sum up, the optimum growth condition to fabricate the InAs QD was determined to be: temp = 320°C, TMIn supply time = 22.5-35 s, In flow = 20 SCCM, and GRI = 30.

4.2   InAs QDs on un-patterned InP

The second step of DE is the crystallisation of the droplets in an atmosphere of arsine. Following droplet deposition, the temperature was ramped up to the crystallisation temperature and stabilised under an AsH$_3$ flow of 24 μmol/min. Subsequently a 'low temperature' InP capping layer was deposited at this same crystallisation temperature. Finally, the temperature was then increased to 600°C to grow a 'high temperature' InP spacer layer to allow for PL emission. There are several important growth parameters which determine the optical properties of QDs: crystallisation temperature, arsine flow, stabilisation time, and capping thickness. With the optimised growth conditions for droplet deposition described in Chapter

4.5, and by manipulating the above growth parameters, the initial optimisation of the crystallisation process was done in collaboration with Dr. Elisa M. Sala. µPL measurements were performed in collaboration with Dr. Aristotelis Trapalis and Max Godsland. In this chapter, the optimisation process will be described briefly, and the structural and optical properties discussed also. Beyond that, further optimisation was achieved by manipulating the indium deposition time, which is a consequence of the knowledge of indium droplet saturation observed in Figure 4-8; this will be discussed in the second chapter. Figure 4-14 shows the droplets before crystallisation and the QDs obtained after crystallisation. Following crystallisation, the density of dots decreased from $2.4*10^9$ cm^{-2} (the original droplet density) to $8.8*10^8$ cm^{-2}. The density decrease is attributed to the longer GRI used for the QD samples. On the other hand, the dimensions increased from (33±6) to (60±5) nm in width and (8±1) to (14±1) nm in height because of the supply of arsine. The InAs QD samples discussed in this chapter were grown following the growth sequence described in Figure 3-12.
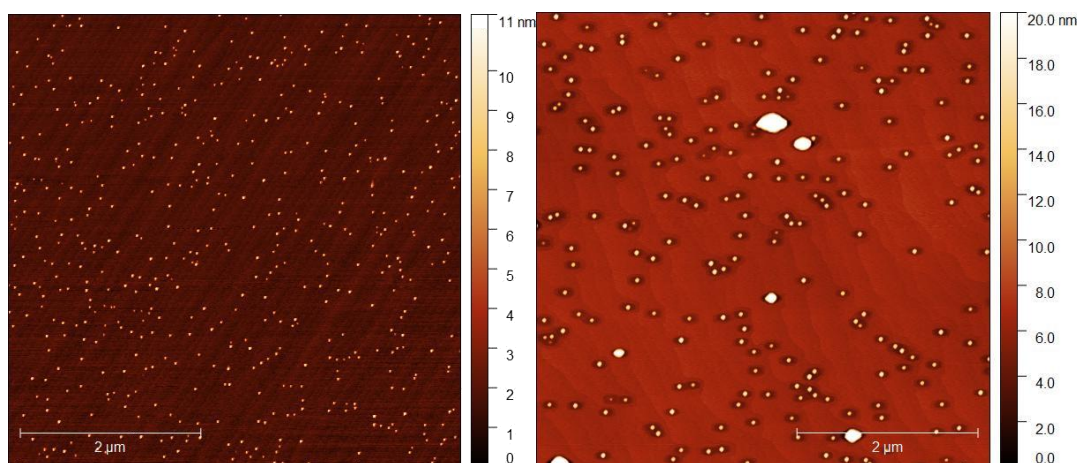

Figure 4-14 (a) Droplets deposited at 320°C with TMIn supply time of 35 s and In flow of 20 SCCM (before crystallisation) and (b) QDs crystallised at 520°C and AsH$_3$ flow of 24 µmol/min with GRI of 60 s

4.2.1 Optimisation of structural and optical properties

For the crystallisation experiments, the droplets were formed under identical growth conditions, as described in Chapter 4.1.5. The droplets prepared accordingly have a diameter and height of 35 nm and 8 nm, respectively, and a density of $2.2*10^9$ cm^{-2}. The effect of crystallisation temperature on QD morphology and their optical properties was explored. Four different temperatures were tested: 480, 500, 520, and 530°C. The other growth parameters were kept constant, namely: AsH$_3$ flow = 24 µmol/min, stabilisation time = 5min, and low

temperature InP capping thickness = 20 nm. Here, the stabilisation time refers to the duration that the crystallisation temperature was maintained under the AsH$_3$ flow. Figure 4-15 shows AFM images of InAs/InP QDs crystallised at different temperatures while Figure 4-16 plots the density and width of the QDs as a function of temperature. For AFM analysis, the samples were cooled down from the crystallisation temperature and taken out from the growth chamber without a capping layer.
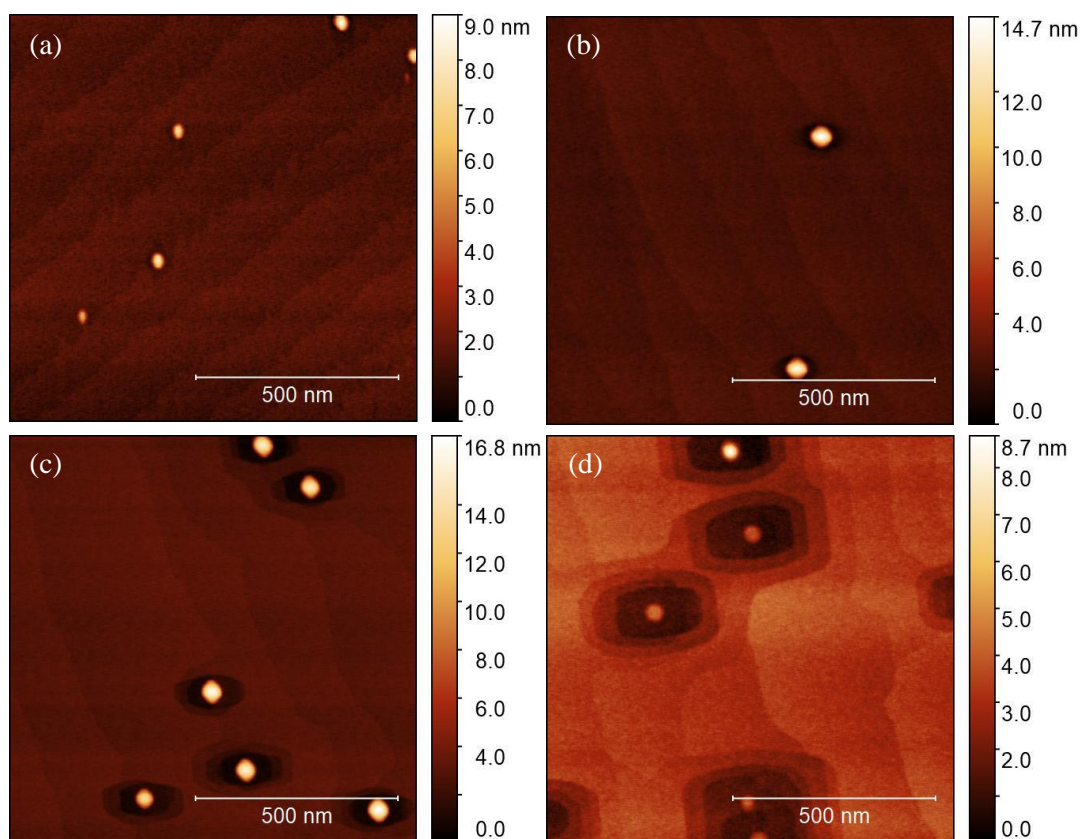

Figure 4-15 AFM images of InAs/InP QDs crystallised at (a) 480°C, (b) 500°C, (c) 520°C, and (d) 530°C

By increasing the crystallisation temperature from 480°C to 520°C, the density of the QDs increased from $4*10^8$ to $9*10^8$/cm^2 while the QD size increased linearly from (45±5) to (60±5) nm in width and from (5±2) to (14±3) nm in height. By further increasing the crystallisation temperature to 530 °C, the density saturated and remains the same as 520°C while the size decreased to (55±5) nm in width and (10±4) nm in height. At high temperature, the InP surface becomes unstable and is easily dissolved due to the absence of a phosphine supply and the In-rich surface configuration after the droplet deposition [99]. By increasing the crystallisation temperature, the dissolved indium atoms contribute to the increase in QD size while the dissolved phosphorous atoms evaporate. However, we postulate that, by further increasing the

temperature from 520°C to 530°C, the indium atoms start to diffuse outward from the droplets. This contributes to the reduction of QD size at 530 °C.
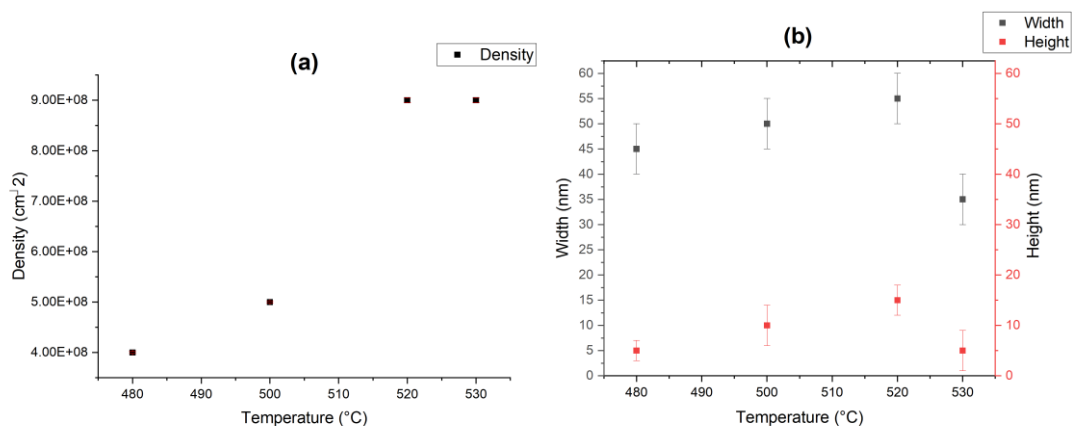

Figure 4-16 The (a) density and (b) size of the QDs as a function of crystallisation temperature

Another distinct feature of this crystallisation process is the etched surface around the dots. Etching was observed from the dots crystalised at or above 500°C. Figure 4-17 shows the cross-sectional profile of a single dot within the etched surface. The etching is attributed to the dissolved indium and phosphorous atoms at high temperature. The area and depth of the locally etched pits was increased by increasing the crystallisation temperature. The etch depth was 1, 2.7, 3.4 nm for temperatures of 500, 520, 530°C respectively. Also, it should be noted that, because of the intrinsic stress asymmetry along the crystallographic directions [0-11] and [0-1-1] at the InAs/InP interface, the etched pits were elongated while the dot itself is symmetric. The width of the etched pit was 130, 165, 205 nm in [0-1-1] direction and 85, 100, 105 nm in the [0-11] for temperatures of 500, 520, 530°C respectively.
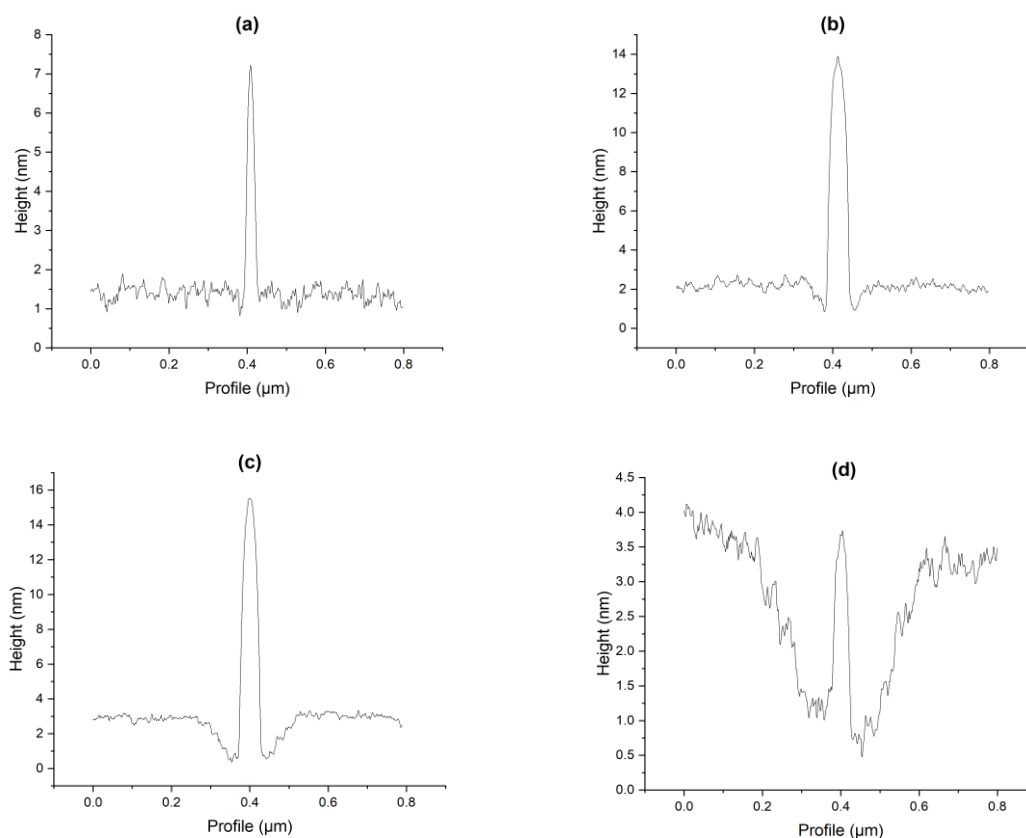
Figure 4-17 The QD profile with the etching as a function of crystallisation temperature by AFM. Droplet etching becomes deeper and broader by the crystallisation temperature.

A quasi-wetting layer

In addition to the formation of dots, the crystallisation process leads to the unintentional formation of a thin quasi-wetting layer comprised of $InAs_xP_{1-x}$, since the InP surface in between the droplets is also exposed to a high flux of pyrolysed arsine. There are similar reports in previous papers on the formation a nonstoichiometric quasi-wetting layer associated with DE. We do not know the precise composition of the InAsP layer but it is estimated from PL and from XSTM (ref. a private communication, R. Raja University of Eindhoven) that it is approximately 30-40% arsenic. The thickness is around 1-2 nm as shown in Figure 4-18 which shows a TEM analysis of the QDs and surrounding layers. According to [100], there is a possible impact on carrier feeding of dots in PL and a possible contribution to coherent noise in single dot emission. However, it should be noted that it is a very thin layer, and in that sense has less of an impact than the thicker wetting layers seen in S-K growth, which is a key advantage of DE.
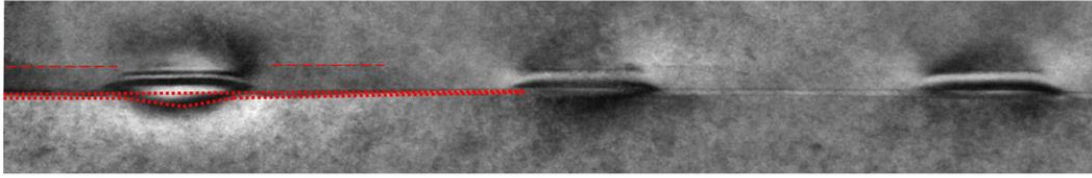
Figure 4-18 A TEM image of buried InAs/InP QDs by DE taken under dark field (002) diffraction conditions. The dotted line indicates the local etching, while the dashed line indicates the capping layer of 20nm. [101]
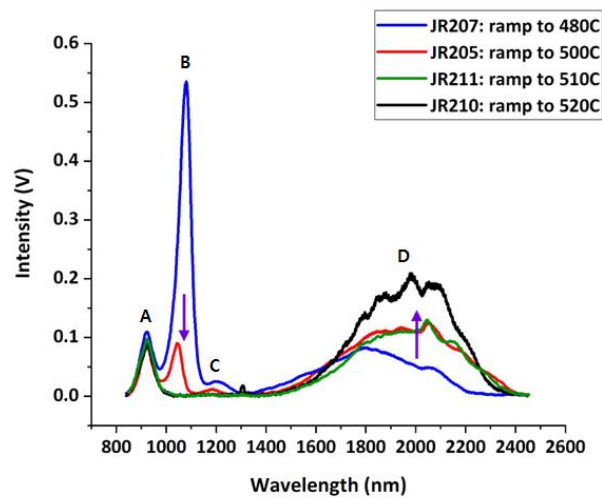

Figure 4-19 RTPL (room temperature photoluminescence) of the QDs crystallised at different temperatures. Emission from 2D layer (band B) decreased and emssion from QDs (band D) increases as the crystallisation temperature increases.

Figure 4-19 shows the room temperature photoluminescence (RTPL) spectra of the InAs/InP QDs crystallised at different temperatures. There are four different emission bands coming from the samples, which are denoted as A-D in the figure. Peak A, at around 920 nm, is ascribed to the InP buffer layer and the broad emission of band D at $\lambda \approx 1600 - 2300$ nm is attributed to InAs QD emission, which has already been demonstrated in previous work [102]. The additional contribution in the 1900-2300 nm range at high growth temperatures corresponds to the QD size increase observed in the AFM investigation. The altered structural properties of the QDs show that the etching magnitude and the emission intensities of the 2D layer are associated with each other. Local etching results in more efficient carrier capture into the QDs. The emission bands B and C at $\lambda \approx 1000$ nm and $\lambda \approx 1200$ nm are believed to be related to the formation of the 2D quasi-wetting layer around the QDs. By increasing the crystallisation

temperature, both peaks are blue-shifted and eventually quenched at 520°C and above. This effect we believe is related to the etching of the surface in proximity to the QDs. As shown in Figure 4-17, the etched surface becomes larger and deeper as a result of increasing the temperature. A gradual reduction in the average thickness of the 2D layer leads to the blue shift in PL and the disappearance of band C from complete etching of this 2D layer around the QDs at the highest temperatures. Note that an expected increase in arsenic incorporation on the InP, i.e. an increase in As concentration in the $InAs_xP_{1-x}$, would lead to a red-shift which was not observed in these experiments. In addition, a higher intensity from band B suggests a more efficient carrier recombination into the QDs.
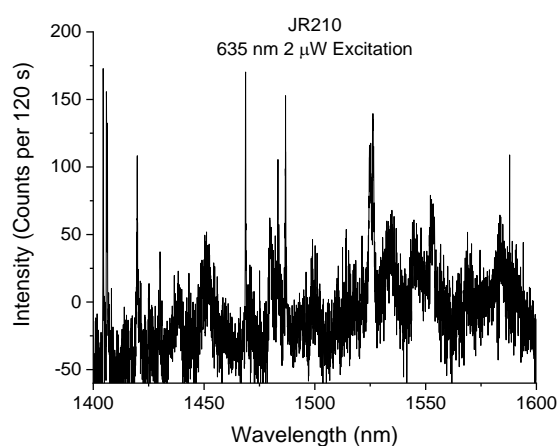

Figure 4-20 μPL spectrum of QDs crystallised at 520°C. The dots are excited at the laser of 9 W/cm².

Single dot emission obtained through low temperature micro-PL was observed from the QDs crystallised at 520°C, as shown in Figure 4-20. Single dot emission was not observed from other samples with higher crystallisation temperatures, indicating the delicate balance of physical properties in the DE process needed for high-quality QDs. It is believed that this is owing to the presence of considerable charge noise which causes to a severe broadening and coalescence of emission peaks. At low temperatures, this is likely due to the effect of the 2D layer acting as an efficient layer for carrier capture. According to [103], the existence of point defects associated with the AsH_3 on the stabilised InP surface may explain the broad emission (as opposed to single dot emission) seen at 530°C. Following a series of experiments employing various crystallisation temperatures, 520°C is thought to be the optimal temperature for droplet crystallisation. The μPL spectra show a broad range of emission linewidths, with some having linewidths of up to 126μeV, however there are many dots with linewidths at the

66

spectrometer resolution of 45 µeV, showing the high quality of dots obtained in these experiments.

4.2.2 Density control and further optimisation

After the initial optimisation, droplet density control was achieved through control of the indium deposition time. Following the results of Chapter 4.1.2, crystallisation of the droplets with a reduced indium deposition time was performed by using the same crystallisation process optimised in Chapter 6.1. Figure 4-21 shows the droplets and consequent QDs at different indium deposition times. A reduction in droplet density from decreasing the indium deposition time leads to a corresponding reduction in QD density. By reducing the indium time from 35 s to 22.5 s, dot density decreased from $9*10^8$ cm^{-2} to $3.2*10^7$ cm^{-2}, while the droplet density decreased from $2.22*10^9$ cm^{-2} to $3.16*10^8$ cm^{-2}. On the other hand, interestingly, from a range of 35 s to 25 s, the QD dimensions decreased while the dimensions of the precursor droplets actually increased. This is thought to be because the number of droplets incorporated to form a dot has decreased, due to the density decrease.

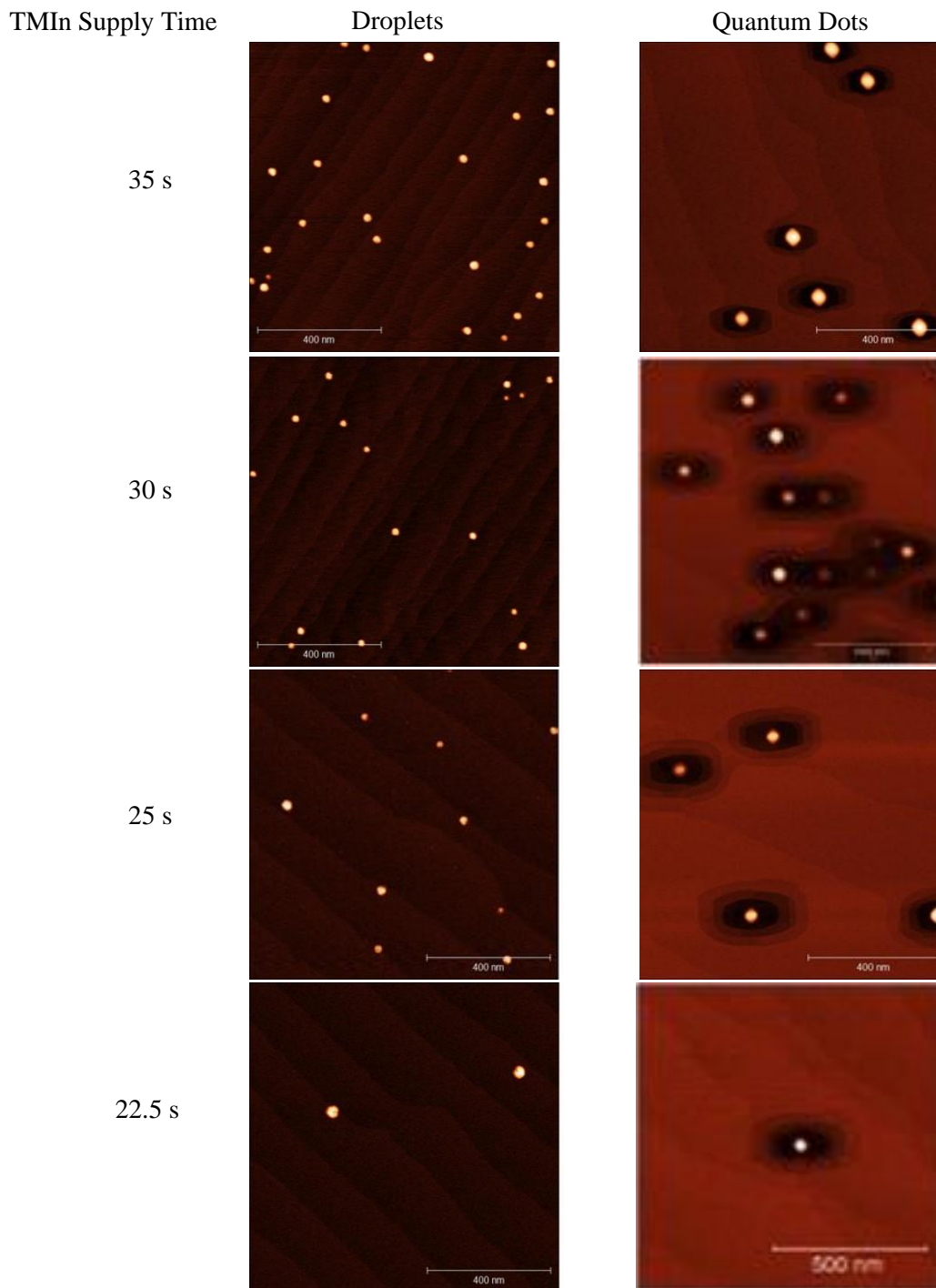| TMIn Supply Time	Droplets	Quantum Dots
35 s		
30 s		
25 s		
22.5 s		

Figure 4-21 Droplets with different indium deposition times (left column) and the consequent QDs (right column). The scan size is 1 x 1 μm for all.

Figure 4-22 shows a cross-sectional profile of a single dot with an etched surface. The area and depth of the locally etched pits increased by reducing the indium deposition time. The depths

are 2.7, 2.7, 3.5, 3.3 nm for times of 35, 30, 25, and 22.5 s, respectively. On the other hand, the width of the etched pits are 200, 262, 345 and 370 nm in the [0-1-1] direction for times of 35, 30, 25, and 22.5 s, respectively.
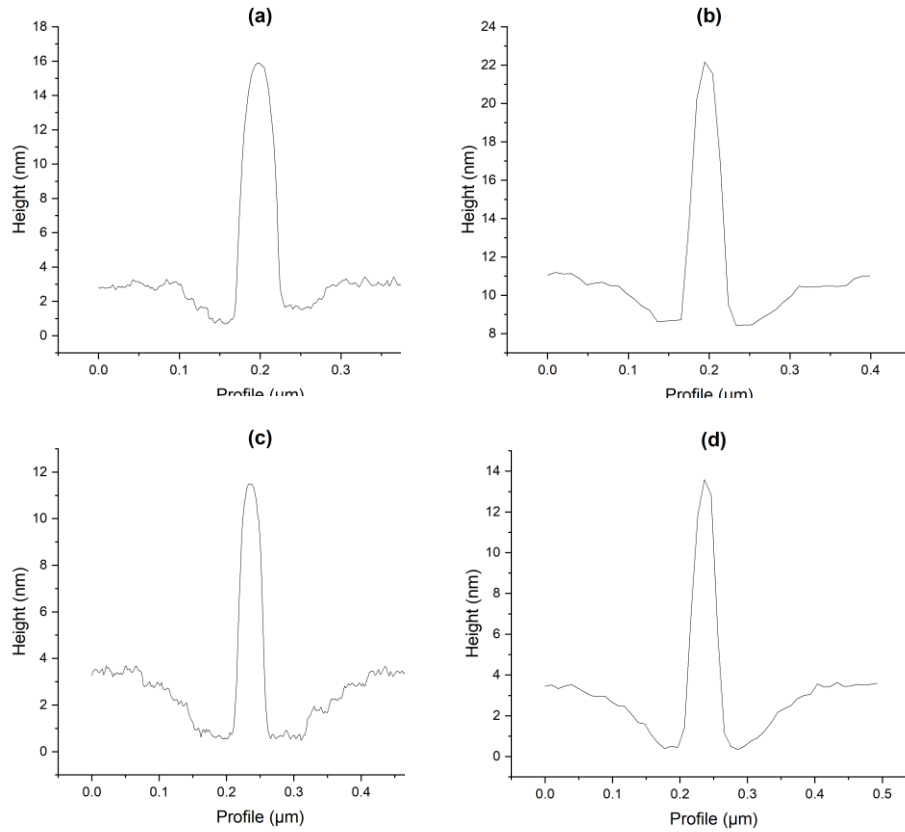
Figure 4-22 Line profile of a QD and its etched surface when indium deposition time is (a) 35 s, (b) 30 s, (c) 25 s, and (d) 22.5 s. The droplet etching gets wider and deeper as the indium deposition time decreases.

A clear correlation between the etching magnitude and improved optical properties has been observed, especially from reducing the indium deposition time from 35 s to 25 s. The linewidth becomes narrower with significantly lower background emissions/noise levels. Due to the consequences of smaller QD formation, the dots do emit at shorter wavelengths. The first column of Figure 4-24 shows a wavelength comparison for indium deposition times of 35 s and 25 s. Most QDs produced with a deposition time of 35 s emit at $\lambda \approx$ 1500-1550 nm, while QDs with a 25 s deposition time emit at 1300-1480 nm. However, the linewidth has been slightly improved. The dots produced via this DE method emit in the 1300 nm and 1550 nm bands, which are both important for telecommunications.

Figure 4-23 µPL results of QDs produced with indium deposition times of 35 s (first row), 30 s (second row), and 25 s (third row). The dots are excited at the laser of 4.5 W/cm². The measurement parameters were kept the same for all.
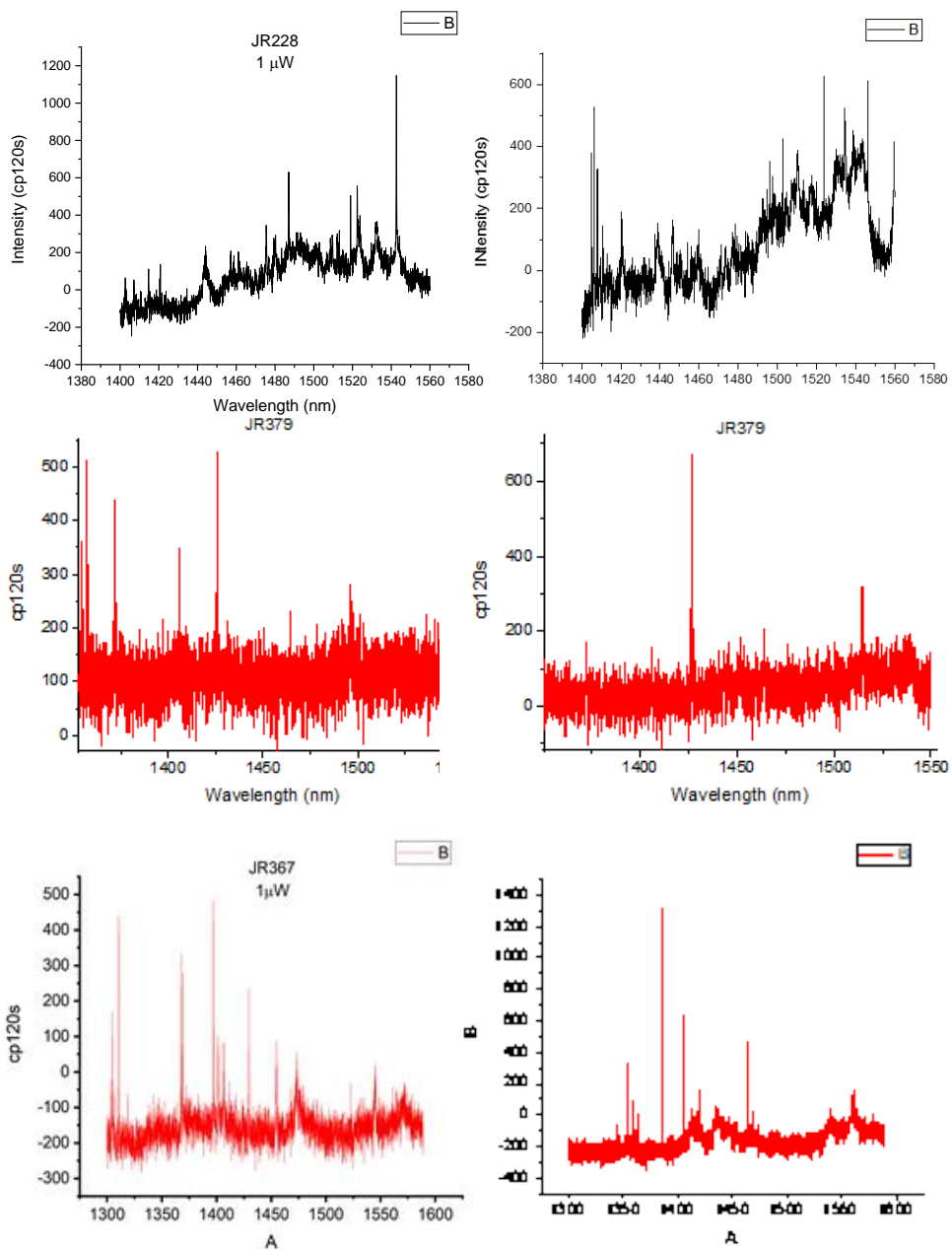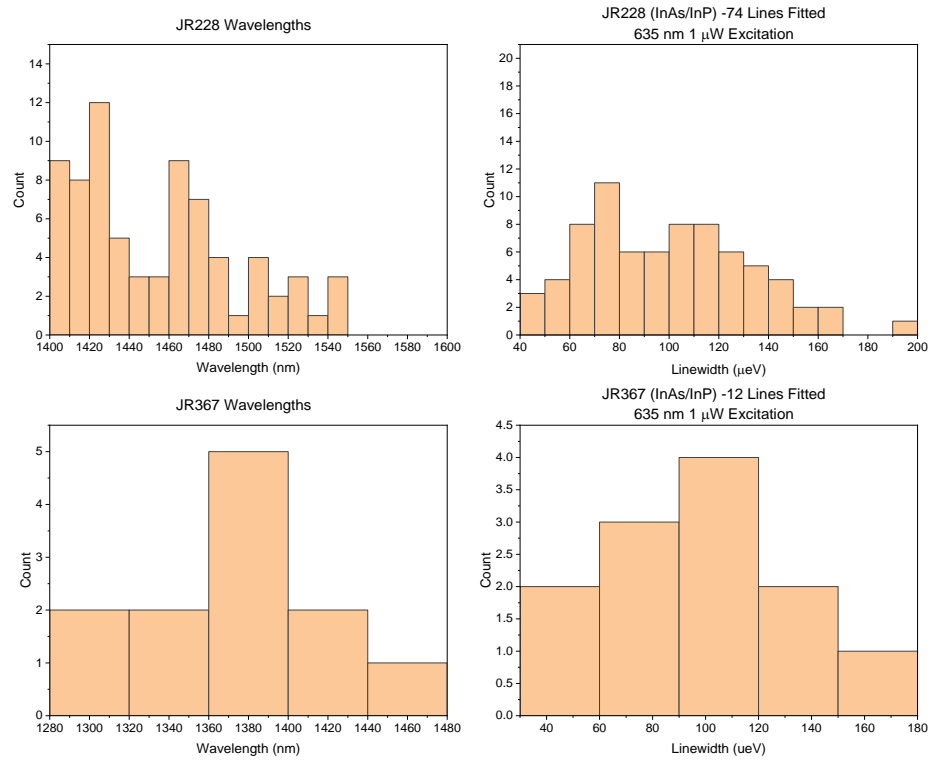
Figure 4-24 Wavelength (left column) and linewidth (right column) comparisons of QDs with 35 s (upper row) and 25 s indium (lower row) deposition times. Emission wavelength was blue shifted at 25 s.

4.2.3   Summary

To summarise, the formation of InAs QDs on planar InP surfaces was investigated using droplet epitaxy with MOVPE. A QD's structural and optical characteristics are significantly affected by modifying the droplet crystallisation temperature and indium deposition time. QDs prepared at temperatures above 500°C are placed in local etch pits whose size is directly proportional to the crystallisation temperature. It was found that the optimum crystallisation temperature was 520°C since only those QDs showed bright single dot emissions in µPL. Their linewidths are mostly distributed close to the spectrometer resolution of 45 µeV, indicating a high degree of coherence. With the narrow linewidth and their 1.55 µm wavelength, this demonstrates high optical quality in the telecom C-band, paving the way for their employment in quantum optics applications. Furthermore, structural and optical studies show a clear correlation between the magnitude of the etching and the optical properties. Owing to etching, low emission intensities of the quasi-wetting layer and the improved QD emission at room temperature for QDs crystallised above 500°C and significant noise

reduction was achieved for QDs grown with 25 s of indium time. This implies local etching improves carrier capture efficiency in QDs. Managing a growth process that combines DE and the etched pits might improve QD optical characteristics, particularly the FSS, a crucial parameter influencing the degree of entanglement in single photon pairs. As a result, this research marks a critical step forward in MOVPE's ability to develop high-quality InAs/InP QDs in etched pits using DE.

5 Indium droplets & InAs QDs on Patterned InP

5.1 Indium droplets on Patterned InP

Self-assembled QDs are distributed randomly on a planar substrate, which leads to low device yield. For application in photonic devices (such as single photon sources), site-controlled QD growth is required. This can be realised by pre-patterning the substrate with nanoholes, which provides a preferential nucleation position for the QDs. In this thesis, we do not seek to control dot formation itself, as has been demonstrated by a large number of authors using the SK method of dot formation and the effect of nanoholes on preferential nucleation of dots in these nanoholes. Instead, we take the approach of site-controlling the precursor droplets, which are then crystalised into quantum dots whilst maintaining their site-control. In this way, we eliminate (to first order) the role of strain in the site control process.

Although there are a number of studies in the literature about site control of gallium droplets on GaAs by MBE [104], site control of indium droplets on InP by MOVPE has not yet been investigated. Having established a method to control droplet size and density on planar substrates in the previous section, we now move on to the work on patterned substrates and achieving site control of droplets and QDs, which is the main aim of this thesis. The following experiments were performed to test if the movement of droplets were affected by using a patterned substrate. Two patterning methods were used: photolithography and electron-beam lithography (EBL). Initial growth of the site-controlled droplets was attempted using photolithography-defined holes while EBL was used to study the impact of nanohole diameter and pitch on droplet localisation. Throughout the experiments, some technical problems arose and were addressed accordingly. In particular, growing a good quality void-free buffer layer with processed nanoholes was a difficult job. This caused significant delays following the initial demonstration of site-controlled droplets on substrates without buffer layer. In order to

solve the problem, a robust *ex situ* surface cleaning technique was developed and several growth parameters tested. Finally, the placement and size of the droplets were found to be influenced by patterning the substrate prior to growth.

5.1.1   Photolithography-defined patterned templates

To site control the droplets, 1 ☐m-wide hole arrays were first of all fabricated via optical lithography to establish whether a patterned substrate would lead to localisation of the droplets in the holes. The holes were fabricated in the manner described in Chapters 3.1 and 3.2 and cleaned by following the procedure described in Chapter 3.3. A list of samples to be discussed in this chapter and their growth parameters are shown in Appendix B.

Buffer growth

Figure 5-1 (a) shows an AFM image of a fabricated 1 ☐m-hole array with 2.5 µm centre-to-centre spacing. The epi-ready fabricated samples were placed in the MOVPE growth chamber. The growth sequence described in Chapter 3.4 was followed. Throughout the experiments, growths of droplets and QDs were performed using the Aixtron MOVPE reactor with its 3x2" wafer capability. A planar InP substate, a so-called 'witness wafer', was always included in the additional susceptor pocket for comparison. For the first growth experiment on the patterned substrate, after the oxide desorption, indium was deposited at 400°C directly, without any buffer layer growth. This was to match the size and density of droplets to those of the photolithography-defined pattern. Figure 5-1 shows AFM images of the substrate before and after the growth. Any residue left on the surface was not detected by the AFM but the substrate surface had a relatively high RMS of 2.5 nm before growth. Because of the rough surface, diffusion of indium atoms was reduced; there was a random distribution of different. The rough surface comes from the ICP dry etching which causes surface damage from ion bombardment. To reduce the roughness, we introduced a 50 nm buffer layer grown after the oxide desorption to provide a better surface morphology and to give better mobility to the deposited indium atoms. As well as its effect on surface roughness, growing a buffer layer is important to move the QDs away from the fabrication interface which inevitably has defects which degrade the optical property of QDs by acting as a recombination centre. By growing a thick buffer, single QD emission with narrow linewidth broadening can be achieved.
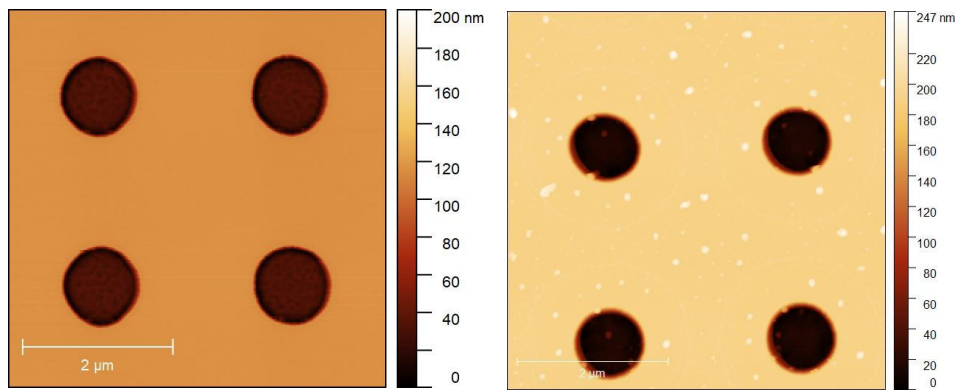
Figure 5-1 AFM images of 1 □m holes before (left)/after (right) indium deposition without buffer

One issue with the growth of buffers in fabricated holes is the nonuniform growth and the formation of voids. This problem is even worse in nanometre-sized holes, but we first of all investigate it with micron-scale holes prepared by photolithography. To achieve a void-free buffer, the cleaning procedure described in Chapter 3.4 is very crucial. Even a slight deviation in the cleaning procedure can lead to unsuccessful buffer growth. Figure 5-2 shows an example. The regrowth of the InP buffer was unsuccessful and produced a large number of voids around the rim of the holes. It should also be noted that, within the pits, buffer growth was enhanced along one crystallographic direction [0-1-1].
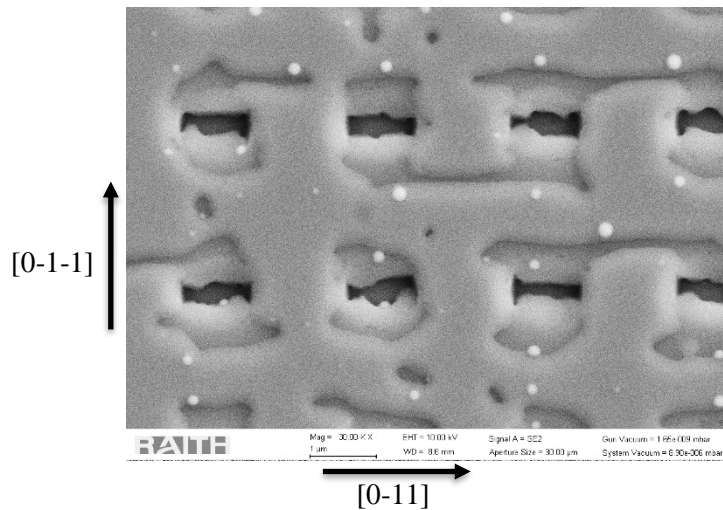

Figure 5-2 Unsuccessful buffer growth due to the surface roughness due to the absence of acid cleaning

These experiments were performed before the acid cleaning step was introduced into the fabrication process. We thus identified the need for an additional acid dip step to reduce

surface roughness. For the follow-up experiments, a solution of 4:1:100 $H_2SO_4/H_2O_2/H_2O$ was used to remove the native oxide layer and smooth out the surface damage caused by ICP dry etching. By performing the acid dip, a dramatic decrease in the RMS of the surface was observed, going from 2.5 nm to 0.790 nm.

To screen the wafers for cleanliness, they were analysed with surface SIMS to detect any hydrocarbons left behind after the fabrication. An acid dip was performed immediately prior to their loading into the growth chamber. JR218 was the first successful instance of buffer growth without any voids. This led to a further improvement in the RMS roughness from 0.790 nm to 0.260 nm. Figure 5-3 shows AFM images of a 4x4 hole array before and after application of a 50 nm InP buffer and indium deposition. A line profile was extracted from one of the holes indicated in Figure 5-3 and shown in Figure 5-4 for comparison. The buffer was grown uniformly without the creation of any voids. There was no change in the hole depth, meaning the same amount of buffer was grown both inside and outside of the hole. However, due to anisotropic growth on different crystallographic planes, there was a change in shape from a cylinder shape to a conical shape with a slightly widened opening.
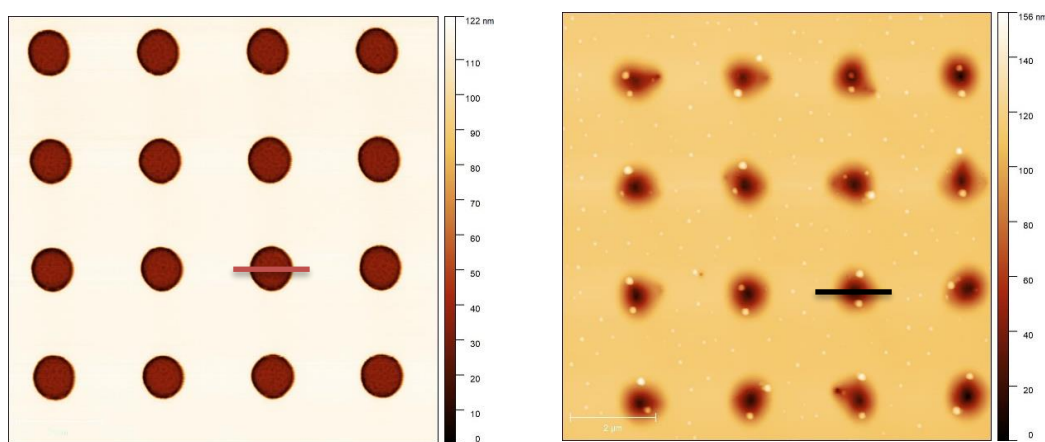
Figure 5-3 AFM images of JR218 before (left) and after (right) growth. The buffer was successfully grown on acid-cleaned substrate and droplets preferentially form around the holes.

In addition, although localisation of droplets was observed, it was not perfect and there were still some smaller droplets present between the holes. It is possible that, due to the long interval between hole fabrication and growth, a thick oxide layer grown during the interval makes oxide desorption hard to remove completely which in turn reduces diffusion and reduces the chance of reaching the holes. By reducing the interval without any change in the growth parameter, perfect localisation of droplets was achieved in the next sample (JR229).

Generally, there was an average of two droplets nucleated in a single hole. It was found that the droplets inside the holes had a comparable size to those on the planar substrate, whereas droplets outside were much smaller. There are two explanations for the greater size of the droplets in the direct vicinity of the holes. Firstly, the etched pit provides high-index surfaces with a large step density where phosphorous atoms are weakly bonded and easily desorbed during indium deposition. This increased the volume of indium deposited and so large indium droplets can form on the slopes of the holes.
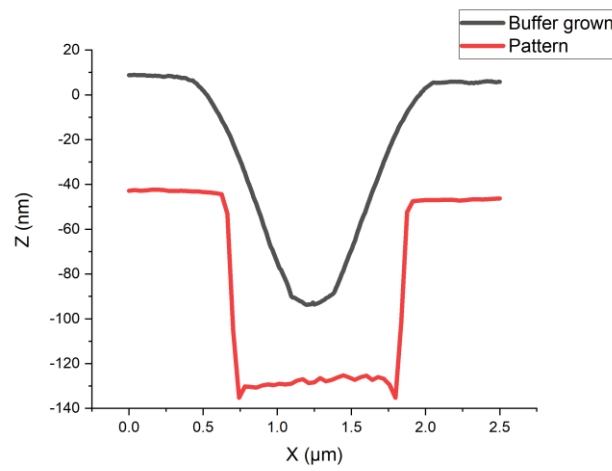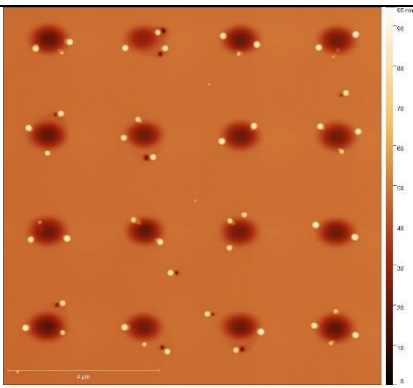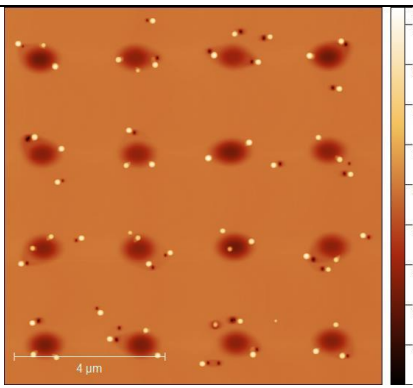
Figure 5-4 Profile of the hole before (red) and after (black) the buffer was grown

Another explanation can be derived from the idea of a capture zone. This term refers to the region of the surface from which islands absorb migrating atoms or molecules. The capture zone region cannot be precisely calculated as the droplets grown at 400°C exhibit Ostwald ripening, and the capture zone is quantified through the number of nearby neighbours as well as through island size. However, from AFM images, it is obvious that droplets do not form directly within the holes, hence it is assumed that the droplets formed around the edges of the holes have a significantly larger capture zone than the ones formed in between, resulting in the greater size of these droplets.

Table 5-1 Comparison of two different V/III ratios

	JR 229 (V/III Ratio: 300)	JR 235 (V/III Ratio: 180)
AFM 10x10um^2		
RMS	450 pm	307 pm
Density	$4.5*10^7$ cm^{-2}	$5*10^7$ cm^{-2}
Size	Height: ~(45±5) nm, Width: ~(220±10) nm	Height: ~(45±5) nm, Width: ~(230±10) nm

To explore this further, we looked at the V/III as one of the growth parameters that can control surface mobility. On patterned substrates, the ratio can also alter the shape of holes by controlling the diffusion of Group III species [105]. By using a large V/III ratio, the diffusion of Group III species is suppressed and, in turn, diffusion along the {111} plane is impeded. Therefore, the effects of the V/III ratio on surface morphology and droplet properties were investigated using two different ratio values, 300 and 180. The growth rate was not affected by changing the V/III ratio as the V/III ratio was controlled by modifying the Group V (arsenic) flow. JR229 and JR235 were both 'buffer + indium droplet' samples grown under identical conditions, except for the V/III ratio. However, they showed a slight difference in surface morphology. Both showed self-created pits outside of the patterned holes, and the number of the pits was reduced by using a large V/III ratio. At the same time, by using a large V/III ratio, the holes were more circular, and less elongation in the [0-1-1] direction was observed even though the RMS surface roughness was slightly higher. Based on this, a V/III ratio of 300 was used for the follow-up experiments. Elongation of the hole will be discussed in detail in the next section.

Hole elongation

It was found that the holes became elongated in one direction after the anisotropic acid cleaning step. Oxide desorption and buffer growth enhanced this elongation. The elongation was reduced by using a large V/III ratio. Figure 5-5 shows the hole profile along two

crystallographic directions which are perpendicular to each other. After the buffer growth, the holes of JR229 (V/III: 300) had dimensions of (990±10) nm in the [0-11] direction and (1330±10) nm in the [0-1-1] direction, while the holes of JR235 had dimensions of (940±10) nm and (1360±10) nm in those same directions. Anisotropic diffusion of indium atoms on InP was already reported in the literature [106]. In the paper, disk shape of quantum rings are observed to be elongated in [0-11] direction. What is highly noteworthy of this work is the formation of two droplets aligned along the [0-11] crystallographic direction. This behaviour might be explained by the preferential migration of material (indium) in the [0-11] direction. In Figure 5-2, it can be clearly seen that buffer growth was enhanced along the [0-1-1] direction elongating the hole in this direction. Hence, the two edges of the elongation became the site of preferential nucleation of the droplets. Figure 5-6 shows SEM images of JR229 and JR235. The two droplets within a hole are aligned in this elongated direction.
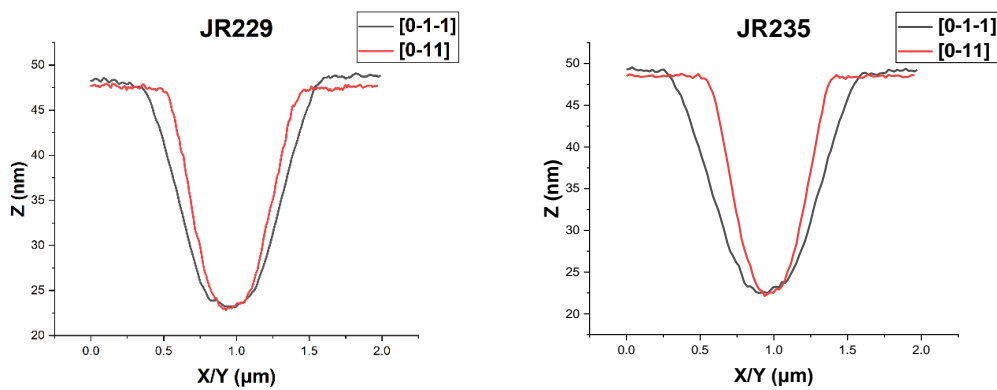
Figure 5-5 Hole profile along the [0-1-1] (black) and [0-11] (red) crystallographic directions when the V/III ratio is 300 (left) and 180 (right). Anisotropic growth at low V/III ratio.
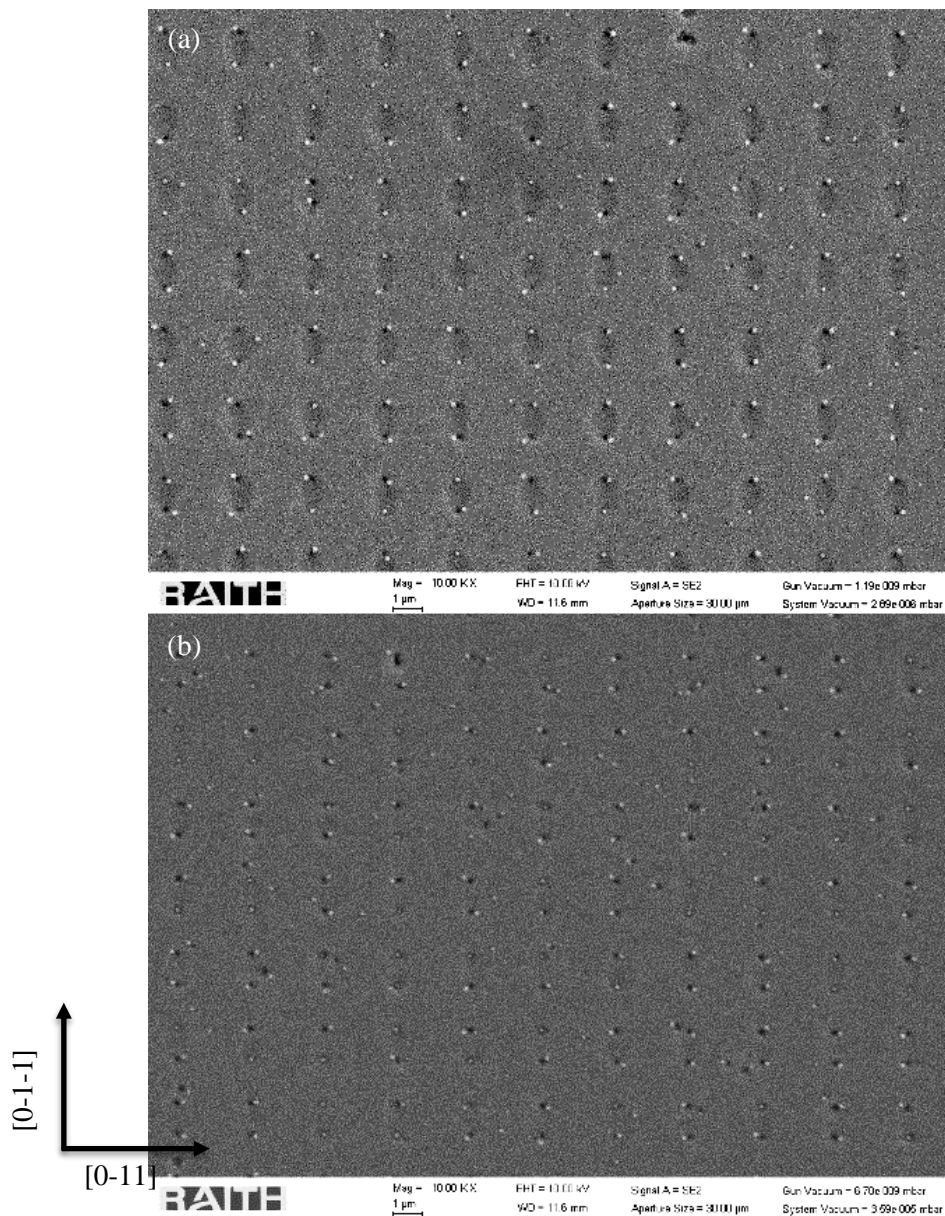
Figure 5-6 SEM images of (a) JR229 (b) JR235. Elongation of the hole in [0-1-1] direction due to the anisotropic growth.

Droplet localisation

The phenomenon that drives the nucleation of the indium droplets within the holes can be explained by the combined effects of capillary condensation and indium adatom diffusion. The nucleation of indium droplets within a hole is driven by a more efficient decrease in the activation energy for droplet nucleation in the presence of conical cavities compared to the planar substrate. The hole provides the indium adatom with the requisite energy advantage needed for nucleation within the holes. In addition, it should be noted that extrinsic nucleation

80

sites can be created during the EBL patterning and etching processes. Small morphological defects at the edge or within the holes might also reduce the activation energy for nucleation.

Also, droplets favour the edge of the holes as formation sites. The AFM images in Table 5-1 show that the droplets nucleate around the edge of the holes but not at the bottom of the holes. The nanohole geometry provides the indium adatom system with the requisite energy advantage for nucleation at the edge of the holes. This behaviour is observed in all of our patterned samples, including the EBL patterned samples, regardless of the nanohole size and pitch. This behaviour contrasts sharply with that of S-K QDs, which nucleate immediately inside the hole due to strain effects. To figure out why the droplets are nucleating around the edges and not directly in the patterned holes, the surface energy of three regions were investigated: the planar area between the holes (config. a), the edge of the holes (config. b), and bottom of the holes (config. c).
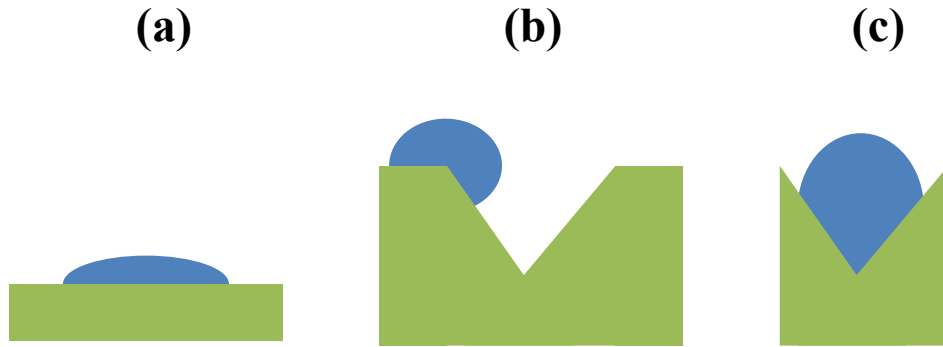
Figure 5-7 The configurations of the droplets: (a) on planar surface, (b) at the edge of the hole, and (c) at the bottom of the hole

To justify nucleation at the edges, the surface energy at the edge of the holes should be lower than that at the planar surface or at the bottom of the hole. When three phases (solid, liquid, and gas) are incorporated, general calculation of the system's energy can be expressed as:

$$E_{system} = \gamma_{l,g}S_{l,g} + \gamma_{s,l}S_{s,l} - \gamma_{s,g}S_{s,l} \tag{5.1}$$

Where γ is the surface tension per unit area in meV/nm^2 and S is the contact area between the two phases. On the other hand, Young's equation defines the relationship between the contact angle, the surface, and interface tension between the three phases.

$$\gamma_{s,g} = \gamma_{s,l} + \gamma_{l,g} \cos(\theta) \tag{5.2}$$

Subsequently, by substituting Eq. 5.2 into Eq. 5.1, Eq. 5.1 can be expressed as:

$$E_{system} = \gamma_{l,g}S_{l,g} + \left(\gamma_{s,g} - \gamma_{l,g}\cos(\theta)\right) * S_{s,l} - \gamma_{s,g}S_{s,l} = \gamma_{l,g}S_{l,g} - \gamma_{l,g}\cos(\theta) * S_{s,l} \tag{5.3}$$

This equation calculates the contact angle of a liquid droplet on a solid surface based on the three surface energies involved. Therefore, the energy of the system can be calculated when $\gamma_{l,g}$, $\gamma_{s,g}$, $\cos(\theta)$, and contact area are known. Such energies for configurations a and b were calculated and compared. The surface tension values can be found in the literature while information on the contact angles and contact surfaces can be extracted from the AFM images taken in this work. The droplet system seems to minimise the energy when the droplets are deposited around the edges, which is observed most of the time. It is predicted that, around the edges, the contact surface between the droplet and the surface is maximised and the contact angle is minimised.

At 400°C, indium melt surface tension is 0.55 J/m^2 according to [107], while for the surface of InP it is approximately 0.75 J/m^2 according to [108]. On a planar surface, the average measured values are 23°, 3.13*10^{-14} m^2, and 2.12*10^{-14} m^2 for θ, $S_{l,g}$ $S_{s,l}$ respectively. On a patterned substrate, the average of measured values are 35°, 3.07*10^{-14} m^2, and 2.66*10^{-14} m^2 for θ, $S_{l,g}$, and $S_{s,l}$ respectively. By substituting the values, the energy of each configuration was obtained as 6.49 * 10^{-15} J/m^2 for a planar surface and 4.9 * 10^{-15} J/m^2 for a patterned surface. The calculation confirmed the hypothesis that the edge of the hole provides a preferential nucleation point by providing a low surface energy.

Compared to the planar substrate, the decrease in surface energy at the edge of the hole explains why droplets favourably form there. However, it is not yet clear why the droplets does not form at the bottom of the holes (config. c). One possible reason is that the indium diffusion is greater in the hole than on the planar surface pushing them outwards. Or the surface damage produced during the fabrication process stops droplets nucleating directly inside.

In summary, the placement and size of the droplets have been found to be influenced by patterning on the substrate prior to growth. For this work, nanohole arrays patterned by

photolithography served as an excellent template for droplet and QD creation. In summary, when a patterned substrate is used as a template for growth, the spatial arrangement of droplets deviates from randomness. This was achieved by modifying the surface energy and giving the droplets a preferential nucleation point.

5.1.2   EBL-defined patterned InP

Site-control of indium droplets

For site-controlled QDs, the occupancy percentage, the number of QDs which nucleate in a single hole, and the positioning accuracy within the hole are all key parameters. Having established a method to localise droplets in photolithography-defined micro-holes, we then introduced EBL to define holes with smaller sizes to allow for increased density but also to address questions around the location of droplet formation and the issue of double occupancy seen in the photolithography work. Thus we aimed to achieve a high percentage of single occupancy with high positioning accuracy (small displacement). For photolithography-defined holes, due to the dimensions of the holes, multiple droplets can form in a single hole. EBL has almost no limitation (~10 nm) and different nanohole dimensions and pitches of interest can be patterned. Four different nanohole sizes (500, 250, 100, 50 nm) and five different pitches (0.5, 1, 1.5, 2.5, 4 μm) were tested to study the impact on droplet mobility and localisation. Moreover, in the previous section, droplets were deposited at 400°C for the initial droplet localisation experiment and to match the droplet size to the hole dimensions. However, droplets grown at 320°C were the only ones suitable for QD crystallisation (from experimental observation) so droplets were deposited at 320°C and their localisation in nanoscale holes was investigated.

Figure 5-8 shows the AFM images of the first '20 nm buffer + indium droplet' deposition experiment. Unfortunately, the re-growth buffer issue becomes even worse here than in photolithography-defined holes. For larger nanoholes, the buffer only grows in between the holes and nothing was grown inside the nanoholes, as evidenced by some of the holes being randomly in-filled. With 50 nm nanoholes the arrays are in fact completely lost due to the planarisation.
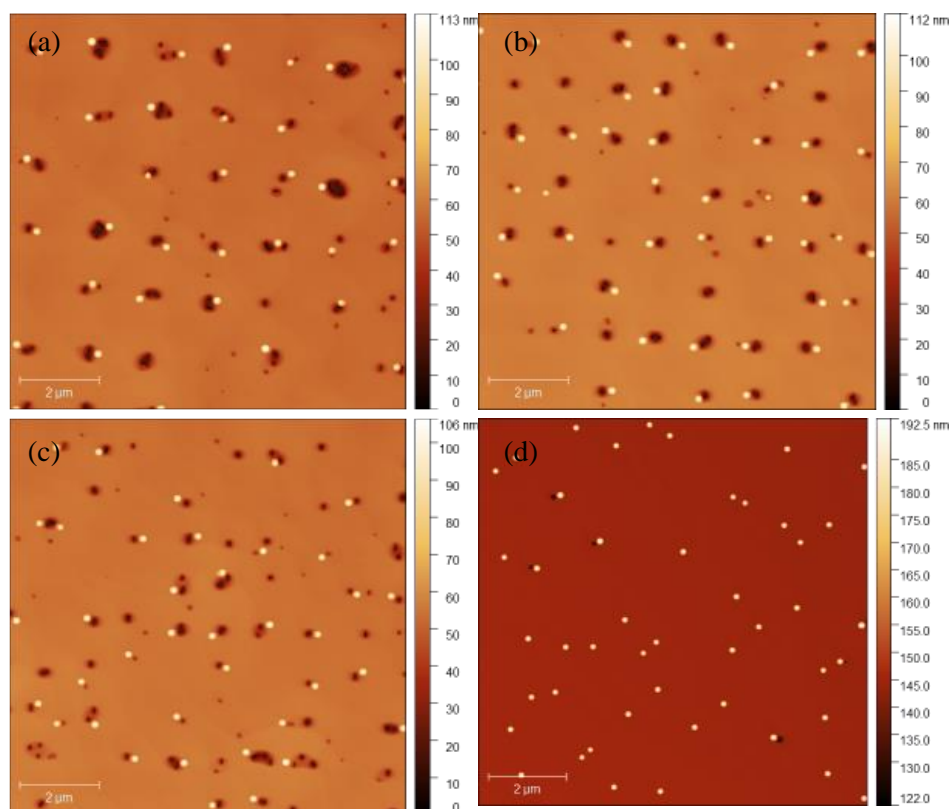
Figure 5-8 AFM images of the first '20 nm buffer + indium droplet' deposition experiment on the EBL patterned nanohole arrays, with nanohole sizes of (a) 500 nm (b) 250 nm (c) 100 nm (d) 50 nm. The buffer was not grown inside the nanoholes due to high growth rate.

Before optimising the buffer growth, indium droplets were deposited without a buffer layer to investigate the localisation in these nanoscale holes. Similar to the observations on photolithography-defined holes, the droplets were nucleated in the vicinity of the nanoholes. However, the nucleation was rather random in terms of direction due to the absence of the anisotropic slope of the side walls. A high percentage of single occupancy was however achieved. It was found that the dimensions and pitches of the nanoholes had an impact on droplet size and density. By reducing the nanohole dimensions, droplet size was decreased from 250 to 200 nm in width and from 50 to 45 nm in height. On the other hand, droplet size was also affected by varying the nanohole pitch. 100% droplet occupancy was achieved by matching the nanohole density to the droplet density (as obtained from planar samples). The droplet size reached its maximum when the pitch was 2.5 µm, where droplet density and nanohole density nearly matches. However, regardless of nanohole size and pitch, the droplet density was maintained at ~3*10^7 cm^{-2}. Therefore, the occupancy level was maintained at ~70% for different hole sizes with the same pitch of 1.5 µm. These results were very encouraging for the goal of site-control of droplets in holes with a reasonable pitch (where, for instance, micro-

PL experiments can be conducted on single dots) and for good occupancy and size for QD crystallisation.

Nanohole Size
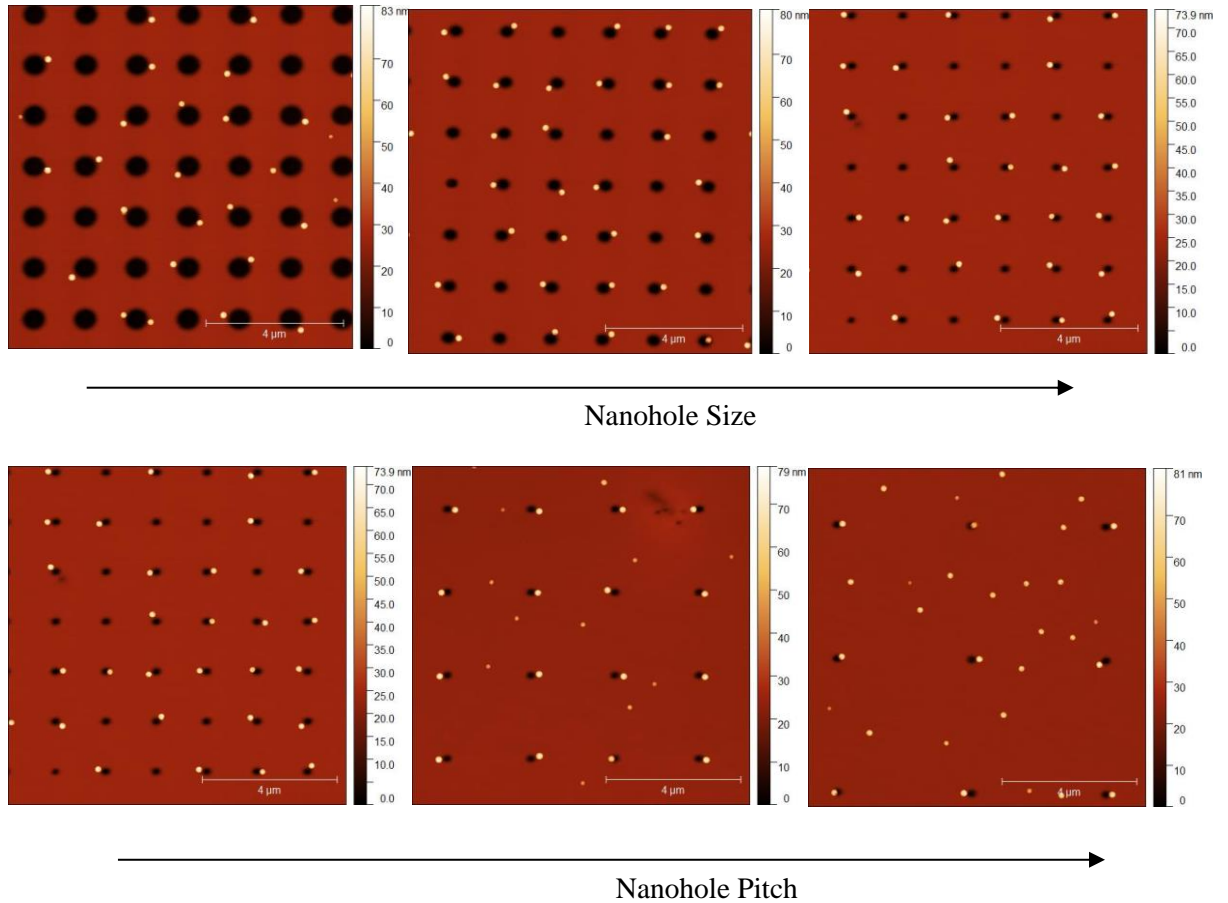
Nanohole Pitch

Figure 5-9 Droplet localisation on EBL-defined nanoholes of different sizes (top) and pitches (bottom). The droplet density is not affected by the nanohole size or pitch. 100% occupancy is reached when nanohole density is the same as the droplet density.

Buffer optimisation

Re-growth of the buffer is important to move the QDs sufficiently away from the fabrication interface, which acts as a charge trap and leads to non-radiative recombination. It was a challenge to control the amount of material grown in the nanohole. Ideally, the buffer should be uniform across the wafer and the nanoholes should be partially in-filled without degradation or complete loss of the array. Hence, we investigated growth parameters such as growth rate, nominal buffer thickness, and V/III ratio to solve the buffer issue presented in Figure 5-8. The problem was that no in-filling occurred and the nanohole depth became the original depth (25 nm) plus the buffer thickness (20 nm). To solve that problem, firstly, the growth rate was

reduced by half, from 2.3 µm/hr to 1.2 µm/hr, to grow the buffer uniformly and improve the buffer quality. The aim here was to increase the adatom diffusion length so that growth occurred further down the nanohole side walls. In addition, the buffer thickness was reduced from 20 nm to 10 nm to prevent the complete planarisation of the 50 nm nanoholes. As a result, the buffer was grown uniformly but another problem arose. It completely planarised the array of even large nanoholes, even though the original hole depth was 25 nm and the target buffer thickness was 10 nm. AFM images of this are not included in the thesis but are very similar to Figure 5-10. That means the material grows much faster in nanoholes resulting in complete planarisation. A high density of step edges introduced within the nanoholes increases the adatom migration and enhances preferential nucleation inside. This is a dramatic effect. To find out the ratio of the growth rate of the nanohole and the planar surface, the 'nominal' buffer thickness was reduced to 3 nm. The planarisation issue was still seen even with the 'nominal' buffer thickness of 3 nm. Nominal buffer thickness is the value obtained from the calibration of planar growth rates. Figure 5-10 shows AFM images of a complete planarisation of the nanohole array with a nominal 3 nm buffer layer. It leaves a shadow of a nanohole array ~1 nm in depth. It was found that there is a very different growth rate inside and outside of the nanoholes and that we could not rely on calibration of the growth rates from the planar substrates to form buffers in nanoholes. Considering the original depth of 25 nm, it was assumed that around 24 nm of buffer was grown within the nanoholes, compared with the nominal growth of 3 nm.
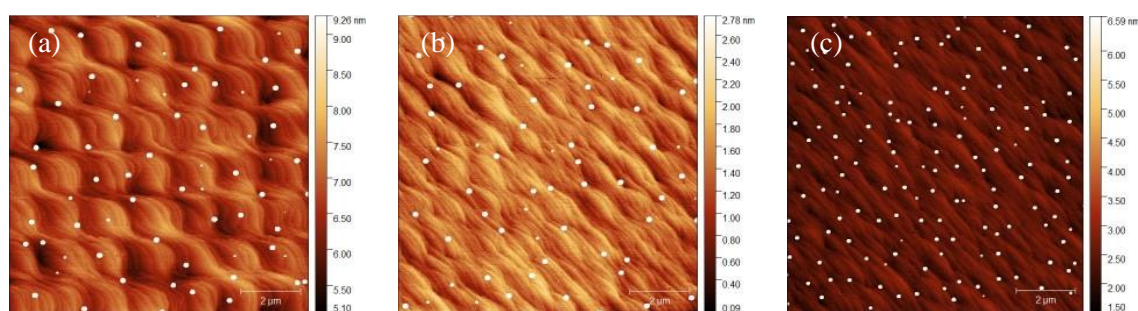
Figure 5-10 Complete planarisation of the nanohole array with only a 3 nm buffer layer. The pitches are (a) 1.5 µm (b) 1 µm (c) 0.5 µm. The scan size is 10 x 10 µm for all.

To prevent complete planarisation, the buffer thickness was then further reduced down to a nominal 1 nm. To reduce complications, droplet deposition was removed and only 1 nm of buffer was grown. It was observed that a fast growth rate on the sidewall of the nanoholes in the [0-1-1] direction was causing the in-filling. However, the buffer was not grown uniformly;

a random number of nanoholes were partially in-filled while no in-filling occurred in the remainder. The enhanced growth rate in [0-1-1] direction was already observed in photolithography-defined holes (Figure 5-2).
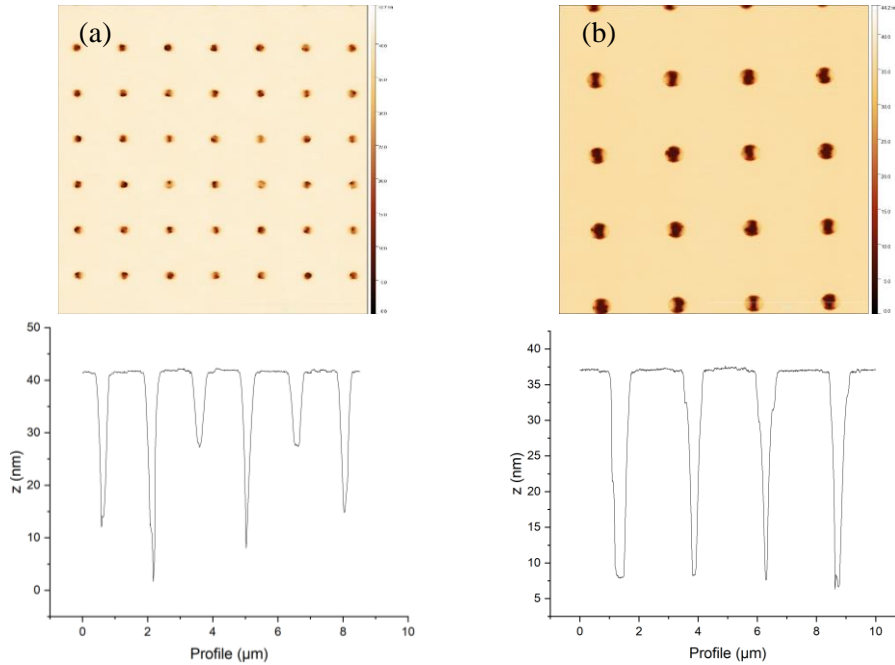
Figure 5-11 AFM images (top) and line profiles (bottom) of 1 nm buffer grown nanohole arrays of nanohole size (a) 100 nm (b) 500 nm. Scan size 10 x 10 μm

Figure 5-12 Nanohole profile before (black) and after (red) 1 nm of buffer in [0-1-1] direction

Hedlund et al. [109] investigated the growth parameters for the formation of photonic-crystal (PC) voids on InP material systems. They controlled the degree of in-filling of the airhole by varying the growth rate, the V/III ratio, and the growth temperature and demonstrated its shape alternation from complete in-filling to perfect encapsulation. According to their paper [109], the degree of in-filling increases when using a 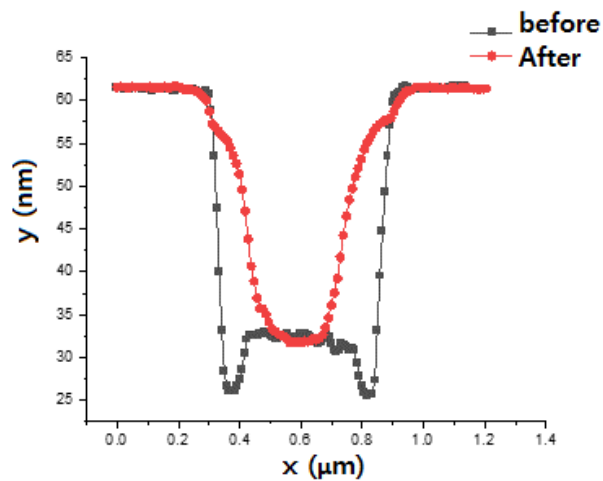high growth temperature and a low growth rate and low V/III ratio. To grow a uniform buffer layer, anisotropic diffusion of indium atom should be suppressed. This can be achieved by using a large V/III ratio. Armed with this information, the V/III ratio was increased to 500 to reduce the number of nanoholes that would be in-filled, by reducing the adatom diffusion length. With a V/III ratio of 500, lateral growth on the side wall became uniform and was supressed further by reducing the adatom diffusion length. The fast growth rate in the [0-1-1] direction was used to practically in-fill the nanoholes. Finally, the nanoholes were partially in-filled and became shallower after the buffer growth. After the growth, 10-15 nm of hole depth was achieved for most of the nanoholes, meaning 10-15 nm was grown within the nanohole.
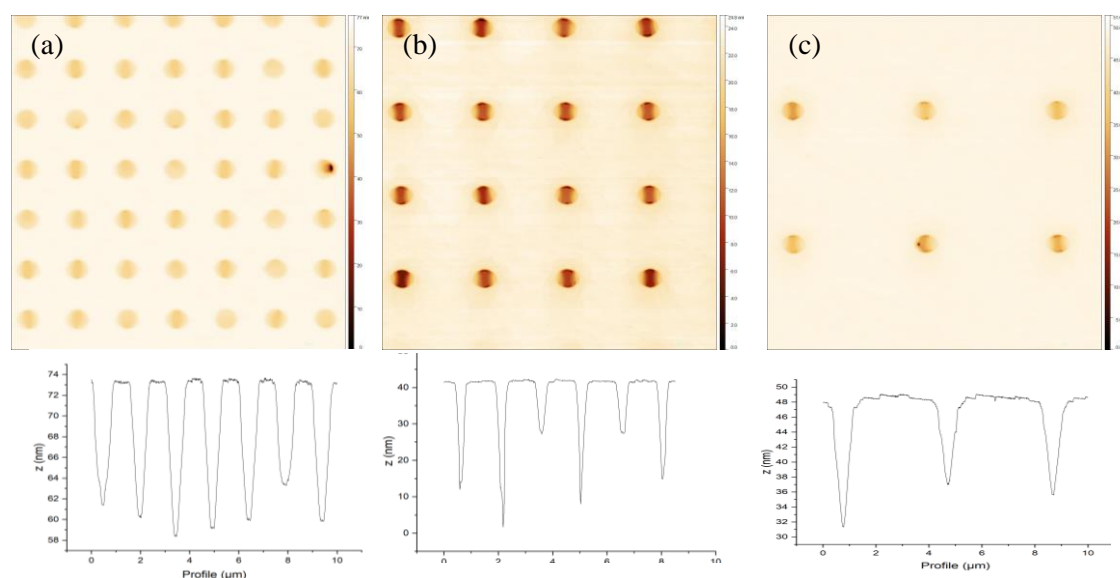
Figure 5-13 AFM images (top) and line profiles (bottom) of 2 nm buffer grown nanohole arrays, with pitches of (a) 1.5 μm (b) 2.5 μm (c) 4.5 μm Uniform buffer growth with a V/III ratio of 500. Scan size 10 x 10 μm

Site-controlled indium droplets with optimised buffer

Finally the droplets were re-introduced and grown at 320°C, a temperature suitable for crystalisation. An average of 4-5 droplets were formed in a single hole in this case. Significantly, no droplet formation occurred in between the holes. AFM images of this are

shown below. Finally, the first objective of the thesis, the localisation of precursor droplets, was achieved. So, the next step is to crystalise them into quantum dots whilst maintaining their site-control.
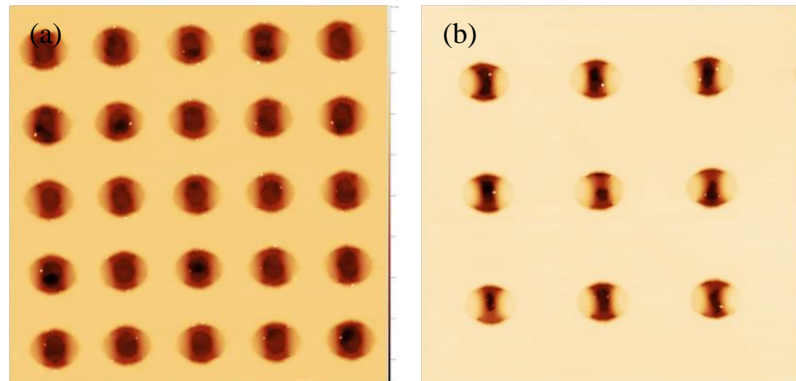
Figure 5-14 AFM images of the first '2 nm buffer (V/III ratio: 500) + In droplet (320°C)' deposition experiment. The pitches are (a) 1 μm and (b) 1.5 μm. Scan size 5 x 5 μm for both.

InAs QD crystallisation

Having produced site-controlled droplets, we were finally ready to convert these site-controlled droplets into quantum dots. This is a new methodology for producing site-controlled QDs. The droplets are crystallised under identical conditions as the planar substrate. Surprisingly, during the crystallsation process, an excess of material caused enlargement of the feature and created defects rather than QDs (Figure 5-15). This is mainly due to the formation of multiple droplets in a single hole and excessive indium material "floating" on the surface. In addition, it is believed that the material excess comes from the exchange of P/As. When the InP surface is exposed to an As ambient, the P atoms on the InP surface are easily exchanged with As atoms because In-As bonds (48 kcal/mol) are slightly more stable than In-P bonds (47.3 kcal/mol). Especially, the exchange is enhanced on the high-index surface with its large step density where phosphorous atoms are weakly bonded. It has been demonstrated that the As/P exchange process may be accelerated at high temperatures and under a high As flow. The As/P exchange roughens the interface, broadens the PL emission, and shifts the emission wavelength of the QDs to beyond 1.6 µm at room temperature.

.
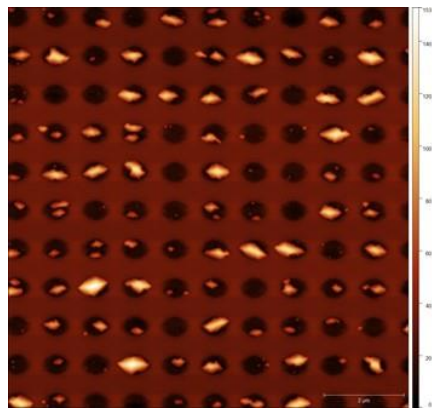
Figure 5-15 Formation of defects during crystallisation due to excessive material on a 500nm nanohole array with a pitch of 1 μm. Scan size 10 x 10 μm.

The amount of As/P exchange can be reduced by reducing the nanohole size. The number of defects has been reduced on the smaller nanoholes. Even though the defects are present, the buffer growth was performed uniformly and ~80% of the nanoholes showed double occupancy with QDs preferentially nucleated in the [0-1-1] direction. This confirms that the formation of defects is due to the As/P exchange with the buffer grown inside the nanohole.
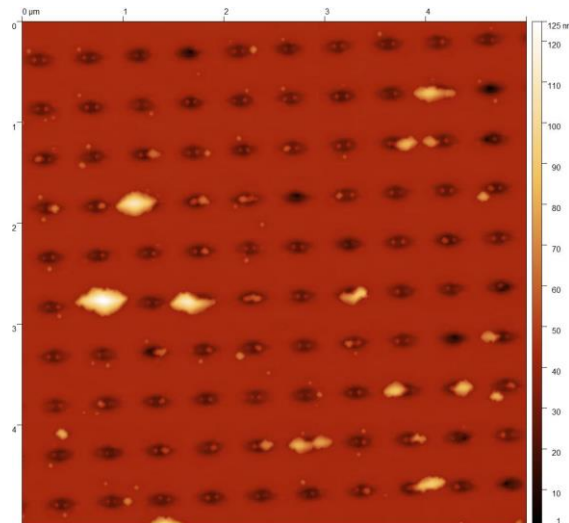
Figure 5-16 InAs crystallisation on a 100 nm nanohole array with a pitch of 1 μm. Scan size 5 x 5 μm.

Figure 5-17 shows a 3D AFM image of a single nanohole where two QDs are nucleated. The QDs are 50 nm in width and 10 nm in height, which is of a comparable size to those on the planar substrates.
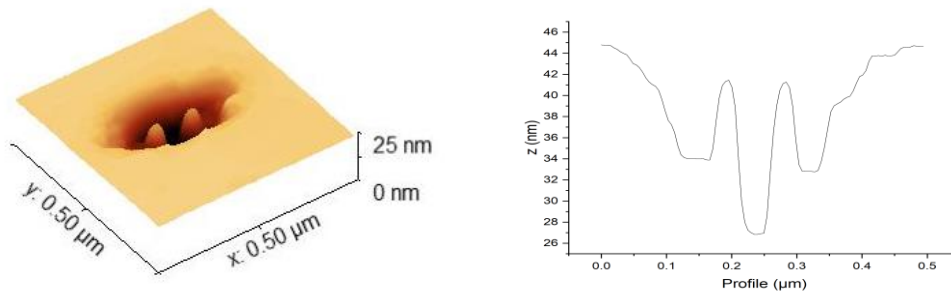
Figure 5-17 3D image (left) and the line profile (right) of single nanohole with two QDs formed within

Finally, these dots were capped for optical characterisation. A broad emission was seen from the QDs λ≈1600-2300 nm but any single dot emission was not detected (Figure 5-18). Nevertheless, this weak ensemble PL emission clearly shows the dots had formed but they were not of the quality to show single line emission. It is believed that the capping process itself also requires further optimisation.
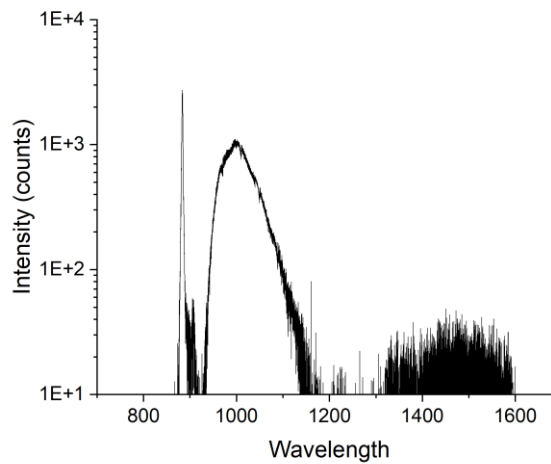
Figure 5-18 Ensemble PL measurement of site-controlled QDs using an excitation power of 100μW and cryostat temperature of 5K

Summary

In summary, QD site-control by a new method of site-control of precursor droplets was achieved in this work. The precursor droplets were localised first and then they were crystallised into QDs without losing their site-control. It was a challenging to obtain a sufficient buffer not to degrade the optical properties of QDs or lose the array, which is the preferential nucleation points for droplets and QDs. This was successfully achieved by

impeding the diffusion of indium by using a large V/III ratio. Finally, the optical characterisation of the site-controlled QDs were attempted. The PL data showed the evidence that dots have formed but to improve the optical properties, and in particular see evidence of site-control of high quality optically active QDs requires further experiments and research.

6 Conclusions

This thesis demonstrated the growth of InAs/InP quantum dots, and their structural and optical characteristics, via droplet epitaxy using MOVPE. The deterministic positioning of QDs through the epitaxy of droplets, followed by their crystallisation into dots in *ex situ* fabricated nanohole arrays was the main focus of the work.

The formation of indium droplets on InP surfaces was extensively studied and optimised to enable site control. The influence of the deposition conditions – including temperature, indium flow rate and flow time, as well as growth interrupt – were all seen to have had a strong influence on both the density and size of the indium droplets formed. By controlling the various parameters separately, a degree of independent control over size and density was possible. This is important for matching these conditions to the density of the nanohole arrays for site control, as well as for ultimately controlling the size of the QDs formed, which determines their emission wavelength.

Following droplet optimisation, the droplets were converted into QDs via crystallisation under the flow of arsine in an MOVPE reactor. It was found that the most important factor during the transformation of indium droplets into InAs QDs was the crystallisation temperature. Photoluminescence investigation revealed that the QDs which crystallised at 520°C had the highest optical quality, where bright, narrow, single emission lines could be seen with low temperature micro-PL. Unlike with the S-K growth of dots, the DE technique also leads to the formation of a local etch pit as well as a thin InAsP layer, the so-called 2D quasi-wetting later, around the dots. It was found that there was a relation between this local etching in the QD's vicinity and the optical properties, which could also be monitored and optimised by evaluating the emission from the quasi-wetting layer. As the etching magnitude increased, the emission of the 2D layer was blue-shifted and eventually quenched and the QD emission gained intensity

at the same time. This likely arose from more efficient carrier recombination into the QDs as the etched pit size increased and the total area of the 2D layer decreased.

After establishing the optimised conditions for InAs QDs to be grown via DE, site control of the droplets and QDs were investigated. Site control is a non-trivial task in which the parameters controlling the localisation of droplets in nanoholes are largely unknown and any effect of the crystallisation process on the subsequent localisation of QDs in the nanoholes was also unknown (including the possibility that crystallisation would destroy the localisation of droplets). In addition, it is well-known that producing site-controlled optically active QDs requires considerable development to ensure that any *ex situ* fabrication of localisation sites (especially etched nanoholes) is clean of any impurities or etch-induced surface damage; all of which can lead to a degradation of a QD's optical properties. This cleaning was also then combined with the development of a high-quality epitaxial buffer layer between the etched surfaces and the subsequently formed QDs. This latter task in particular proved to be very challenging in this project.

Nanohole arrays were fabricated using EBL and ICP etching and served as the preferential nucleation sites for droplets, and subsequently, QDs. Extensive optimisation of the surface cleaning process following nanohole fabrication successfully generated low impurity levels (as evidenced by surface SIMS) and a low post-fabrication RMS surface roughness; both reproducibly obtained and found to be critical for high quality dot formation. The growth of the InP buffer was also investigated to provide a sufficient distance for dot formation from the fabrication interface and to provide partial in-fill of nanoholes without degradation or complete loss of the array. It was found that the growth rate within the nanoholes was over an order of magnitude less than the 'nominal' thickness of the InP buffer grown on a planar substrate. The buffer growth was anisotropic within the nanoholes. Although such effects have been seen in the literature, optimising it for DE localisation was challenging but was eventually achieved, primarily by using a high V/III ratio and a reduced growth rate.

Following successful localisation of droplets into the nanohole arrays (in which droplet density was tailored to the array density), crystallisation of droplets into QDs was demonstrated. This was not straightforward as the buffer in the arrays also contributed to the crystallisation process through an As/P exchange process. In the nanoholes, the exchange rate was enhanced due to the high-index surface where phosphorous atoms are more weakly bonded to the substrate than planar surface. Especially, in larger nanoholes, an excess of material caused

enlargement of the crystallised feature and created defects rather than QDs. Therefore, to suppress this problem, nanoholes with a small diameter were used. With this approach, site control of QDs in the nanohole array was achieved. Due to the anisotropic growth of the buffer layer (leading to an asymmetric hole), we found the formation of pairs of QDs in each nanohole aligned along the [0-1-1] direction. The percentage occupancy of QDs within the nanohole array was high. This was an important achievement in itself with regard to the ability to potentially scale this method up. In addition, there were no dots formed between the arrays, which indicates we have a deterministic process for site control that could be relied upon for scale-up of device architectures.

6.1   Suggestions for future work

This thesis has developed and optimised a process for achieving site control of QDs formed through the intermediary step of site control of indium droplets in nanohole arrays. There were many parameters and processes to control in this development, and the end result was the successful demonstration of site-controlled QDs in nanohole arrays. This included an InP buffer layer that is important for high-quality optically emitting QDs for quantum photonics applications. Due to the major difficulties in controlling the buffer layer formation, we were unable to demonstrate optical emission from the site-controlled QDs, which required the use of an InP capping layer. An attempt was made, but it appears that the capping process itself requires further optimisation. Therefore, the most obvious next experimental step is to further optimise this capping layer process and to demonstrate optical emission; characterising the quality and uniformity of single dot emission spectra from the arrays.

In addition, there is still room for improving the buffer layers, which are critical. There are certainly some parameters that have not been investigated in this project such as the growth temperature. It would also be interesting to further study the effect of nanohole depth. Since a resist was used as a soft mask for dry etching in this project, it was only possible to get a nanohole depth up to ~25 nm. Using a hard dielectric mask such as silicon dioxide or silicon nitride would provide more freedom in terms of etching time and allow fabrication of a deeper nanohole by enabling a longer etch. In this project, due to the shallow nanohole depth, growing a thick buffer was limited. This will certainly reduce the buffer issue. Additionally, in the literature, it has been noted that deep nanoholes produced better single occupancy statistics.

All of this optimisation will be necessary to improve the optical properties of site-controlled QDs. Ultimately this would include the optimisation of the optical properties to produce narrow single QD linewidths with high coherence times suitable for on-chip quantum photonics experiments such as multi-photon entanglement. Although the site-controlled yield demonstrated in this thesis was high, further optimisation of this property is required since ultimately 100% occupancy yield is required for the quantum photonics systems of the future. Another interesting avenue of research is the investigation of a stacked QD growth system which may be a route to higher optical quality in quantum dots (with the stacked dot being the highest quality as it is furthest away from the buffer interface). There are numerous studies showing that stacked QDs are beneficial for site-controlled QDs but this has not been widely explored with QDs produced via DE.

Finally, since we have observed the phenomenon of local droplet etching in this work, and found that this etching is important in the dynamics of carrier capture into the QDs (as evidenced by bright emissions of QDs under certain growth conditions). A promising area for future research is the question of the interaction between this local etching and the *ex situ* etching provided by the nanohole itself. Through this effect we may see an improvement in overall QD symmetry and size distribution, both of which are important for commercial photonics devices.

7 References

[1]   G. E. Moore, "Cramming more components onto integrated circuits, Reprinted from Electronics, volume 38, number 8, April 19, 1965, pp.114 ff.," *IEEE Solid-State Circuits Soc. Newsl.*, vol. 11, no. 3, pp. 33–35, Feb. 2009, doi: 10.1109/N-SSC.2006.4785860.

[2]   "Quantum Effects At 7/5nm And Beyond." https://semiengineering.com/quantum-effects-at-7-5nm/ (accessed Nov. 05, 2021).

[3]   R. P. Feynman, "Simulating Physics with Computers," *Feynman Comput.*, pp. 133–153, Nov. 2018, doi: 10.1201/9780429500459-11.

[4]   D. Loss and D. P. Divincenzo, "Quantum computation with quantum dots," 1998.

[5]   C. H. Bennett and G. Brassard, "Quantum cryptography: Public key distribution and coin tossing," *Theor. Comput. Sci.*, vol. 560, no. P1, pp. 7–11, Mar. 2020, doi: 10.1016/j.tcs.2014.05.025.

[6]   K. Takemoto *et al.*, "Quantum key distribution over 120 km using ultrahigh purity single-photon source and superconducting single-photon detectors," *Sci. Reports 2015 51*, vol. 5, no. 1, pp. 1–7, Sep. 2015, doi: 10.1038/srep14383.

[7]   Ł. Dusanowski, M. Syperek, and P. Mrowiński, "Single photon emission at 1.55 μm from charged and neutral exciton confined in a single quantum dash," *Appl. Phys. Lett*, vol. 105, p. 21909, 2014, doi: 10.1063/1.4890603.

[8]   S. Anantathanasarn, R. Nötzel, and P. J. Van Veldhoven, "Wavelength-tunable (region) InAs quantum dots in (100) grown by metal-organic vapor-phase epitaxy ARTICLES YOU MAY BE INTERESTED IN," *J. Appl. Phys*, vol. 98, p. 13503, 2005, doi: 10.1063/1.1938271.

[9]   D. Fuster, K. Abderrafi, B. Alén, Y. González, L. Wewior, and L. González, "InAs nanostructures grown by droplet epitaxy directly on InP(001) substrates," *J. Cryst. Growth*, vol. 434, pp. 81–87, Jan. 2016, doi: 10.1016/j.jcrysgro.2015.11.003.

References

[10] J. Skiba-Szymanska *et al.*, "Universal Growth Scheme for Quantum Dots with Low Fine-Structure Splitting at Various Emission Wavelengths," *Phys. Rev. Appl.*, vol. 8, no. 1, Jul. 2017, doi: 10.1103/PhysRevApplied.8.014013.

[11] T. Müller *et al.*, "A quantum light-emitting diode for the standard telecom window around 1,550 nm," *Nat. Commun.*, vol. 9, no. 1, Dec. 2018, doi: 10.1038/s41467-018-03251-7.

[12] L. Sapienza *et al.*, "Combined atomic force microscopy and photoluminescence imaging to select single InAs/GaAs quantum dots for quantum photonic devices," *Sci. Rep.*, vol. 7, no. 1, pp. 1–8, 2017, doi: 10.1038/s41598-017-06566-5.

[13] C. Schneider *et al.*, "Single photon emission from a site-controlled quantum dot-micropillar cavity system," *Appl. Phys. Lett.*, vol. 94, no. 11, p. 111111, Mar. 2009, doi: 10.1063/1.3097016.

[14] B. Rigal *et al.*, "Site-controlled quantum dots coupled to a photonic crystal molecule," *Appl. Phys. Lett.*, vol. 107, no. 14, p. 141103, Oct. 2015, doi: 10.1063/1.4932228.

[15] P. Bhattacharya, *Semiconductor optoelectronic devices*. Upper Saddle River Prentice Hall, 1997.

[16] S. M. Sze, "High-speed semiconductor devices," p. 643, 1990.

[17] H. Sugawara, M. Ishikawa, and G. Hatakoshi, "High-efficiency InGaAlP/GaAs visible light-emitting diodes," *Appl. Phys. Lett.*, vol. 58, no. 10, p. 1010, Jun. 1998, doi: 10.1063/1.104407.

[18] E. F. Schubert, "Light Emitting Diodes, 2nd Edition," *Springer Verlag Berlin Heidelb. New York Cambridge Univ. Press*, p. 422, 2006.

[19] T. Miya, Y. Terunuma, T. Hosaka, and T. Miyashita, "Ultimate low-loss single-mode fibre at 1.55 μm," *Electron. Lett.*, vol. 15, no. 4, pp. 106–108, Feb. 1979, doi: 10.1049/EL:19790077.

[20] Y. Gou, J. Wang, Y. Cheng, Y. Guo, X. Xiao, and S. Zhou, "A modeling and experimental study on the growth of VCSEL materials using an 8×6 inch planetary MOCVD reactor," *Coatings*, vol. 10, no. 8. 2020, doi: 10.3390/COATINGS10080797.

[21] T. Wu *et al.*, "Mini-LED and Micro-LED: Promising candidates for the next generation display technology," *Applied Sciences (Switzerland)*, vol. 8, no. 9. 2018, doi: 10.3390/app8091557.

[22] D. P. Divincenzo, "The Physical Implementation of Quantum Computation," *Scalable Quantum Comput.*, pp. 1–13, Jan. 2005, doi: 10.1002/3527603182.CH1.

[23] "Scalable Quantum Computers," *Scalable Quantum Comput.*, Dec. 2000, doi: 10.1002/3527603182.

[24] M. Razeghi, *Fundamentals of Solid State Engineering , 3 Edition*, 2nd ed. Springer science & business media, 2009.

[25] W. Liu, W. T. Zheng, and Q. Jiang, "First-principles study of the surface energy and work function of III-V semiconductor compounds," *Physical Review B - Condensed Matter and Materials Physics*, vol. 75, no. 23. 2007, doi: 10.1103/PhysRevB.75.235322.

[26] C. J. K. Richardson, E. Waks, J.-H. Kim, R. P. Leavitt, and T. Cai, "Two-photon interference from a bright single-photon source at telecom wavelengths," *Opt. Vol. 3, Issue 6, pp. 577-584*, vol. 3, no. 6, pp. 577–584, Jun. 2016, doi: 10.1364/OPTICA.3.000577.

[27] X. Liu *et al.*, "Single-photon emission in telecommunication band from an InAs quantum dot grown on InP with molecular-beam epitaxy," *Appl. Phys. Lett.*, vol. 103, no. 6, p. 061114, Aug. 2013, doi: 10.1063/1.4817940.

[28] M. Benyoucef, M. Yacob, J. P. Reithmaier, J. Kettler, and P. Michler, "Telecom-wavelength (1.5 μm) single-photon emission from InP-based quantum dots," *Appl. Phys. Lett.*, vol. 103, no. 16, p. 162101, Oct. 2013, doi: 10.1063/1.4825106.

[29] T. Miyazawa *et al.*, "Single-Photon Generation in the 1.55-μm Optical-Fiber Band from an InAs/InP Quantum Dot," *Jpn. J. Appl. Phys.*, vol. 44, no. 5L, p. L620, May 2005, doi: 10.1143/JJAP.44.L620.

[30] G. P. Agrawal, *Fiber-Optic Communications Systems, Third Edition.*, vol. 6. 2002.

[31] S. Electric, "InP Sub n-type," 2021. https://global-sei.com/sc/products_e/inp/n.html.

[32] D. Dieter, M. Grundmann, and N. N. Ledentsov, *Quantum dots heterostructures*. Chichester: John Wiley & Sons: John Wiley & Sons, 1999.

[33] R. A. Hogg and Zhang Ziyang, "Quantum dot technologies," in *The physics and engineering of compact quantum do-based lasers for biophotonics*, E. U. Rafailov, Ed. Weinheim, Germany: John Wiley & Sons, 2013, pp. 7–42.

[34] R. C. C. Leon *et al.*, "Coherent spin control of s-, p-, d- and f-electrons in a silicon quantum dot," *Nat. Commun. 2020 111*, vol. 11, no. 1, pp. 1–7, Feb. 2020, doi: 10.1038/s41467-019-14053-w.

[35] P. V. Kamat, "Quantum dot solar cells. The next big thing in photovoltaics," *J. Phys. Chem. Lett.*, vol. 4, no. 6, pp. 908–918, 2013, doi: 10.1021/jz400052e.

[36] L. Sun *et al.*, "Bright infrared quantum-dot light-emitting diodes through inter-dot spacing control," *Nat. Nanotechnol.*, vol. 7, no. 6, pp. 369–373, 2012, doi: 10.1038/nnano.2012.63.

[37] A. Y. Liu *et al.*, "Electrically pumped continuous-wave 1.3 µm quantum-dot lasers epitaxially grown on on-axis (001) GaP/Si," *Opt. Lett.*, vol. 42, no. 2, pp. 338–341, 2017, doi: 10.1364/OL.42.000338.

[38] H. J. Kimble, "The quantum internet," *Nature*, vol. 453, no. 7198, pp. 1023–1030, 2008, doi: 10.1038/nature07127.

[39] H.-S. Yeo, K. Lee, J.-H. Cho, S.-H. Park, and Y.-H. Cho, "Control of the 3-Fold Symmetric Shape of Group III-Nitride Quantum Dots: Suppression of Fine-Structure Splitting," *Nano Lett.*, vol. 20, no. 12, pp. 8461–8468, Dec. 2020, doi: 10.1021/ACS.NANOLETT.0C02236.

[40] M. Zieliński, "Vanishing fine structure splitting in highly asymmetric InAs/InP quantum dots without wetting layer," *Sci. Reports 2020 101*, vol. 10, no. 1, pp. 1–13, Aug. 2020, doi: 10.1038/s41598-020-70156-1.

[41] P. Lodahl, S. Mahmoodian, and S. Stobbe, "Interfacing single photons and single quantum dots with photonic nanostructures," *Reviews of Modern Physics*, vol. 87, no. 2. pp. 347–400, 2015, doi: 10.1103/RevModPhys.87.347.

[42] I. N. Stranski and L. Krastanow, "Zur Theorie der orientierten Ausscheidung von Ionenkristallen aufeinander," *Monatshefte für Chemie und verwandte Teile anderer Wissenschaften 1971 711*, vol. 71, no. 1, pp. 351–364, Dec. 1937, doi: 10.1007/BF01798103.

[43] H. Luth, *Surfaces and interfaces of solid materials*. Springer science & business media, 2013.

[44] R. J. Warburton, "Self-assembled semiconductor quantum dots," *Contemp. Phys.*, vol. 43, no. 5, pp. 351–364, 2002, doi: 10.1080/0010751021012384.

[45] D. J. P. Ellis, R. M. Stevenson, R. J. Young, A. J. Shields, P. Atkinson, and D. A. Ritchie, "Control of fine-structure splitting of individual InAs quantum dots by rapid thermal annealing," *Appl. Phys. Lett.*, vol. 90, no. 1, p. 011907, Jan. 2007, doi: 10.1063/1.2430489.

[46] J. Zhang *et al.*, "High yield and ultrafast sources of electrically triggered entangled-photon pairs based on strain-tunable quantum dots," *Nat. Commun. 2015 61*, vol. 6, no. 1, pp. 1–8, Dec. 2015, doi: 10.1038/ncomms10067.

[47] G. Juska, V. Dimastrodonato, L. O. Mereni, A. Gocalinska, and E. Pelucchi, "Towards quantum-dot arrays of entangled photon emitters," *Nat. PHOTONICS |*, vol. 7, 2013, doi: 10.1038/NPHOTON.2013.128.

[48]   X. Liu *et al.*, "Vanishing fine-structure splittings in telecommunication-wavelength quantum dots grown on (111)A surfaces by droplet epitaxy," *RAPID Commun. Phys. Rev. B*, vol. 90, p. 81301, 2014, doi: 10.1103/PhysRevB.90.081301.

[49]   S. Hasan, O. Richard, C. Merckling, and W. Vandervorst, "Encapsulation study of MOVPE grown InAs QDs by InP towards 1550nm emission," *J. Cryst. Growth*, vol. 557, p. 126010, 2021.

[50]   J. M. García, L. González, M. U. González, J. P. Silveira, Y. González, and F. Briones, "InAs/InP(0 0 1) quantum wire formation due to anisotropic stress relaxation: In situ stress measurements," *Journal of Crystal Growth*, vol. 227–228. pp. 975–979, 2001, doi: 10.1016/S0022-0248(01)00962-9.

[51]   M. Syperek *et al.*, "Single photon emission at 1.55 μm from charged and neutral exciton confined in a single quantum dash," *Appl. Phys. Lett.*, vol. 105, no. 2, Jul. 2014, doi: 10.1063/1.4890603.

[52]   L. He, M. Gong, C. F. Li, G. C. Guo, and A. Zunger, "Highly reduced fine-structure splitting in InAs/InP quantum dots offering an efficient on-demand entangled 1.55-μm photon emitter," *Physical Review Letters*, vol. 101, no. 15. 2008, doi: 10.1103/PhysRevLett.101.157405.

[53]   N. Koguchi, S. Takahashi, and T. Chikyow, "New Mbe Growth Method for Insb Quantum-Well Boxes," *J. Cryst. Growth*, vol. 111, no. 1–4, pp. 688–692, 1991, doi: 10.1016/0022-0248(91)91064-H.

[54]   K. Nobuyuki and I. Keiko, "Growth of GaAs Epitaxial Microcrystals on an S-Terminated GaAs Substrate by Successive Irradiation of Ga and As Molecular Beams," *Jpn. J. Appl. Phys.*, vol. 32, no. 5R, p. 2052, 1993.

[55]   B. Sergio, B. Francesco Basso, T. Artur, B. Emiliano, F. Alexey, and S. Stefano, "High–temperature droplet epitaxy of symmetric GaAs/AlGaAs quantum dots," *Sci. Rep.*, vol. 10, no. 1, pp. 1–10, 2020.

[56]   Á. Nemcsics, L. Tóth, L. Dobos, and A. Stemmann, "Facetting of the self-assembled droplet epitaxial GaAs quantum dot," *Microelectron. Reliab.*, vol. 51, no. 5, pp. 927–930, 2011.

[57]   Z. Gong, Z. C. Niu, S. S. Huang, Z. D. Fang, B. Q. Sun, and J. B. Xia, "Formation of GaAs/AlGaAs and InGaAs/GaAs nanorings by droplet molecular-beam epitaxy," *Appl. Phys. Lett.*, vol. 87, no. 9, p. 093116, 2005.

[58]   P. J. Simmonds and M. L. Lee, "Tensile-strained growth on low-index GaAs," *J. Appl. Phys.*, vol. 112, no. 5, p. 054313, 2012.

[59]   S. Bietti, L. Esposito, A. Fedorov, A. Ballabio, A. Martinelli, and S. Sanguinetti, "Characterization and Effect of Thermal Annealing on InAs Quantum Dots Grown by Droplet Epitaxy on GaAs(111)A Substrates," *Nanoscale Res. Lett.*, vol. 10, no. 1, Dec. 2015, doi: 10.1186/s11671-015-0930-3.

[60]   N. Ha *et al.*, "Droplet epitaxial growth of highly symmetric quantum dots emitting at telecommunication wavelengths on InP(111)A," *Cit. Appl. Phys. Lett. Appl. Phys. Lett. J. Vac. Sci. Technol. B Nanotechnol. Microelectron. Mater. Process. Meas. Phenom. J. Appl. Phys. Appl. Phys. Lett.*, vol. 1041, no. 10, pp. 183113–10801, 2014, doi: 10.1116/1.4972049.

[61]   N. Ha *et al.*, "Droplet epitaxy growth of telecom InAs quantum dots on metamorphic InAlAs/GaAs(111)A," 2015, Accessed: Feb. 06, 2018. [Online]. Available: http://iopscience.iop.org/article/10.7567/JJAP.54.04DH07/pdf.

[62]   W. Katsuyuki, K. Nobuyuki, and G. Yoshihiko, "Fabrication of GaAs Quantum Dots by Modified Droplet Epitaxy," *Jpn. J. Appl. Phys.*, vol. 39, no. 2A, p. L79, 2000.

[63]   A. Nemcsics, "Quantum Dots Prepared by Droplet Epitaxial Method," in *Quantum Dots - Theory and Applications*, V. Stavrou, Ed. InTech, 2015.

[64]   C. Heyn, A. Stemmann, A. Schramm, H. Welsch, W. Hansen, and Á. Nemcsics, "Regimes of GaAs quantum dot self-assembly by droplet epitaxy," *Physical Review B - Condensed Matter and Materials Physics*, vol. 76, no. 7. 2007, doi: 10.1103/PhysRevB.76.075317.

[65]   R. K. Akchurina *et al.*, "Formation Conditions for InAs/GaAs Quantum Dot Arrays by Droplet Epitaxy under MOVPE Conditions," *Tech. Phys.*, vol. 84, pp. 79–85, 2014.

[66]   Y. Nonogaki, T. Iguchi, S. Fuchi, Y. Fujiwara, and Y. Takeda, "InAs dots grown on InP (001) by droplet hetero-epitaxy using OMVPE," *Mater. Sci. Eng. B51*, pp. 118–121, 1998, [Online]. Available: https://ac.els-cdn.com/S0921510797002420/1-s2.0-S0921510797002420-main.pdf?_tid=4f294070-0b3c-11e8-a495-00000aacb362&acdnat=1517921609_0e85241b008d09592356572311cadd90.

[67]   Y. Nonogaki, T. Iguchi, Y. Fujiwara, and Y. Takeda, "Formation of InAs islands on InP (001) by droplet hetero-epitaxy," *Appl. Surf. Sci.*, vol. 117, no. 118, pp. 665–669, 1997, Accessed: Feb. 06, 2018. [Online]. Available: https://ac.els-cdn.com/S0169433297801614/1-s2.0-S0169433297801614-main.pdf?_tid=2a66ac78-0b3c-11e8-80d6-00000aab0f02&acdnat=1517921547_e50d1b1bd7f7269fd4b705fdaf589ae3.

References

[68]   Y. Nonogaki, T. Iguchi, S. Fuchi, Y. Fujiwara, and Y.Takeda, "Effects of vicinal InP (001) surface on InAs dots grown by droplet hetero-epitaxy," *Mater. Sci. Eng. B*, vol. 58, no. 3, pp. 195–198, 1998.

[69]   J. Sormunen, J. Riikonen, M. Mattila, J. Tiilikainen, Markku Sopanen, and H. Lipsanen, "Transformation of Self-Assembled InAs/InP Quantum Dots into Quantum Rings without Capping," *Nano Lett.*, vol. 5, no. 8, pp. 1541–1543, 2005.

[70]   T. Ujihara, Y. Yoshida, W. S. Lee, and Y. Takeda, "Size uniformity of InAs dots on mesa- structure templates on (001) InP substrates grown by droplet metal-organic vapor phase epitaxy method," *Appl. Phys. Lett.*, vol. 89, no. 8, p. 083110, 2006.

[71]   R. K. Akchurin, I. A. Boginskaya, A. A. Marmalyuk, M. A. Ladugin, and M. A. Surnina, "Development of fundamentals of droplet epitaxy for the formation of quantum dot arrays in the InAs/GaAs system under MOVPE conditions," *Russian Microelectronics*, vol. 41, no. 8. pp. 453–458, 2012, doi: 10.1134/S1063739712080021.

[72]   Z. B. Chen *et al.*, "Elemental diffusion during the droplet epitaxy growth of In(Ga)As/GaAs(001) quantum dots by metal-organic chemical vapor deposition," *Appl. Phys. Lett.*, vol. 104, no. 2, p. 022108, Jan. 2014, doi: 10.1063/1.4859915.

[73]   A. Rosenauer, U. Fischer, D. Gerthsen, and A. Förster, "Composition evaluation of InxGa1−xAs Stranski-Krastanow-island structures by strain state analysis," *Appl. Phys. Lett.*, vol. 71, no. 26, p. 3868, Jun. 1998, doi: 10.1063/1.120528.

[74]   J. Houel *et al.*, "Probing Single-Charge Fluctuations at a GaAs/AlAs Interface Using Laser Spectroscopy on a Nearby InGaAs Quantum Dot," *Phys. Rev. Lett.*, vol. 108, no. 10, p. 107401, Mar. 2012, doi: 10.1103/PhysRevLett.108.107401.

[75]   L. Yang *et al.*, "Optical spectroscopy of site-controlled quantum dots in a Schottky diode," *Cit. Appl. Phys. Lett*, vol. 108, 2016, [Online]. Available: https://doi.org/10.1063/1.4952767.

[76]   M. K. Yakes *et al.*, "Leveraging crystal anisotropy for deterministic growth of inas quantum dots with narrow optical linewidths," *Nano Lett.*, vol. 13, no. 10, pp. 4870–4875, 2013, doi: 10.1021/nl402744s.

[77]   A. Huggenberger *et al.*, "Narrow spectral linewidth from single site-controlled In(Ga)As quantum dots with high uniformity," *Appl. Phys. Lett.*, vol. 98, no. 13, pp. 2009–2012, 2011, doi: 10.1063/1.3568890.

[78]   Y. Nakamura *et al.*, "Vertical alignment of laterally ordered InAs and InGaAs quantum dot arrays on patterned (0 0 1) GaAs substrates," *J. Cryst. Growth*, vol. 242, no. 3–4, pp. 339–344, Jul. 2002, doi: 10.1016/S0022-0248(02)01442-2.

References

[79] A. Maalouf, M. Gadonna, and D. Bosc, "An improvement in standard photolithography resolution based on Kirchhoff diffraction studies," *J. Phys. DApplied Phys.*, vol. 42, no. 1, p. 015106, 2008.

[80] Rohm and Haas Electronic Materials, "Megaposit SPR350 series photoresist." 2007, [Online]. Available: https://ostec-materials.ru/upload/iblock/Dow SPR350_TDS.pdf.

[81] S. O. Martinez-Chapa, A. Salazar, and M. J. Madou, "Two-Photon Polymerization as a Component of Desktop Integrated Manufacturing Platforms," *Three-Dimensional Microfabr. Using Two-phot. Polym. Fundam. Technol. Appl.*, pp. 374–416, Jan. 2016, doi: 10.1016/B978-0-323-35321-2.00019-4.

[82] All resist, "Product information - New developments CSAR 62 • Electra 92 • AR-N 7520 1." 2017, [Online]. Available: https://www.allresist.com/wp-content/uploads/sites/2/2016/12/homepage_allresist_produktinfos_csar_electra_7520_englisch.pdf.

[83] K. Nojiri, "Dry Etching Damage," *Dry Etch. Technol. Semicond.*, pp. 73–89, 2015, doi: 10.1007/978-3-319-10295-5_5.

[84] S. Guilet, S. Bouchoule, C. Jany, C. S. Corr, and P. Chabert, "Optimization of a Cl2–H2 inductively coupled plasma etching process adapted to nonthermalized InP wafers for the realization of deep ridge heterostructures."

[85] P. Strasser, R. Wüest, F. Robin, D. Erni, and H. Jäckel, "Detailed analysis of the influence of an inductively coupled plasma reactive-ion etching process on the hole depth and shape of photonic crystals in InP∕InGaAsP," *J. Vac. Sci. Technol. B Microelectron. Nanom. Struct. Process. Meas. Phenom.*, vol. 25, no. 2, p. 387, Mar. 2007, doi: 10.1116/1.2712198.

[86] J. S. Parker, E. J. Norberg, R. S. Guzzon, S. C. Nicholes, and L. A. Coldren, "High verticality InP/InGaAsP etching in Cl2/H2/Ar inductively coupled plasma for photonic integrated circuits," *J. Vac. Sci. Technol. B, Nanotechnol. Microelectron. Mater. Process. Meas. Phenom.*, vol. 29, no. 1, p. 011016, Jan. 2011, doi: 10.1116/1.3522659.

[87] K. Kennedy, K. M. Groom, and R. A. Hogg, "Fabrication of v-groove gratings in InP by inductively coupled plasma etching with SiCl4/Ar," *Semicond. Sci. Technol.*, vol. 21, no. 1, p. L1, Nov. 2005, doi: 10.1088/0268-1242/21/1/L01.

[88] P. Atkinson, O. G. Schmidt, S. P. Bremner, and D. A. Ritchie, "Formation and ordering of epitaxial quantum dots," *Comptes Rendus Physique*, vol. 9, no. 8. pp. 788–803, 2008, doi: 10.1016/j.crhy.2008.10.014.

References

[89] P. Atkinson *et al.*, "Site-control of InAs quantum dots using Ex-situ electron-beam lithographic patterning of GaAs substrates," *Jpn. J. Appl. Phys.*, vol. 45, no. 4 R, pp. 2519–2521, 2006, doi: 10.1143/JJAP.45.2519.

[90] H. Z. Song *et al.*, "Site-controlled quantum dots fabricated using an atomic-force microscope assisted technique," *Nanoscale Res. Lett.*, vol. 1, no. 2, pp. 160–166, 2006.

[91] G. B. Stringfellow, *Organometallic vapor-phase epitaxy: theory and pracitice*. Elsevier, 1999.

[92] A. C. Jones and M. L. Hitchman, "Overview of Chemical Vapour Deposition," *Chem. Vap. Depos. Precursors, Process. Appl.*, pp. 1–36, 2009, doi: 10.1039/9781847558794.

[93] G. B. Nair and S. J. Dhoble, *The Fundamentals and Applications of Light-Emitting Diodes: The Revolution the lighting industry*. Woodhead Publishing, 2020.

[94] X. Guoa *et al.*, "The effect of growth temperature on InAs quantum dots grown by," vol. 8308, no. Tianhe Li, pp. 1–7.

[95] A. Ludwig *et al.*, "Ultra-low charge and spin noise in self-assembled quantum dots," *J. Cryst. Growth*, vol. 477, pp. 193–196, 2017, doi: 10.1016/j.jcrysgro.2017.05.008.

[96] N. I. Buchan, C. A. Larsen, and G. B. Stringfellow, "Mass spectrometric studies of trimethylindium pyrolysis," *Journal of Crystal Growth*, vol. 92, no. 3–4. pp. 591–604, 1988, doi: 10.1016/0022-0248(88)90044-9.

[97] U. Konig, W. Keck, and A. Kriks, "CONTACT ANGLES IN THE LIQUID PHASE EPITAXY OF InP, GaInAs AND GaInAsP," 1984.

[98] J. H. Lee, Z. MWang, and G. J. Salamo, "Observation of change in critical thickness of In droplet formation on GaAs(100)," *J. Phys. Condens. Matter*, vol. 19, no. 17, p. 176223, 2007, doi: 10.1088/0953-8984/19/17/176223.

[99] Z. M. Wang, B. L. Liang, K. A. Sablon, and G. J. Salamo, "Nanoholes fabricated by self-assembled gallium nanodrill on GaAs(100)," *Appl. Phys. Lett.*, vol. 90, no. 11, p. 113120, Mar. 2007, doi: 10.1063/1.2713745.

[100] M. Anderson *et al.*, "Quantum teleportation using highly coherent emission from telecom C-band quantum dots," *npj Quantum Inf. 2020 61*, vol. 6, no. 1, pp. 1–7, Jan. 2020, doi: 10.1038/s41534-020-0249-5.

[101] E. M. Sala, M. Godsland, A. Trapalis, and J. Heffernan, "Effect of Cap Thickness on InAs/InP Quantum Dots Grown by Droplet Epitaxy in Metal–Organic Vapor Phase Epitaxy," *Phys. Status Solidi - Rapid Res. Lett.*, vol. 15, no. 9, pp. 1–6, 2021, doi: 10.1002/pssr.202100283.

[102] S. Hasan *et al.*, "InAlGaAs encapsulation of MOVPE-grown InAs quantum dots on InP(0 0 1) substrate," 2019, doi: 10.1016/j.jcrysgro.2019.125342.

References

[103] R. A. Masut, M. A. Sacilotti, A. P. Roth, D. Digby, and F. Williams, "InP (and GaAs) substrate stabilization by the presence of GaAs (and InP) in a metal-organic vapour-phase epitaxy system1."

[104] E. M. Sala, M. Bollani, S. Bietti, A. Fedorov, L. Esposito, and S. Sanguinetti, "Ordered array of Ga droplets on GaAs(001) by local anodic oxidation," *J. Vac. Sci. Technol. B, Nanotechnol. Microelectron. Mater. Process. Meas. Phenom.*, vol. 32, no. 6, p. 061206, 2014, doi: 10.1116/1.4901017.

[105] A. F. McKenzie *et al.*, "Void engineering in epitaxially regrown GaAs-based photonic crystal surface emitting lasers by grating profile design," *Appl. Phys. Lett.*, vol. 118, no. 2, Jan. 2021, doi: 10.1063/5.0035038.

[106] T. Noda, T. Mano, M. Jo, T. Kawazu, and H. Sakak, "Self-assembly of InAs ring complexes on InP substrates by droplet epitaxy," *J. Appl. Phys.*, vol. 112, p. 063510, 2012.

[107] D. Pasquariello, M. Camacho, K. Hjort, L. Dó Zsa B, and B. Szentpáli, "Evaluation of InP-to-silicon heterobonding," 2001. [Online]. Available: www.elsevier.com/locate/mseb.

[108] V. P. Chentsov, V. G. Shevchenko, A. G. Mozgovoi, and M. A. Pokrasin, "Density and surface tension of heavy liquid-metal coolants: Gallium and indium," *Inorg. Mater. Appl. Res.*, vol. 2, no. 5, pp. 468–473, Dec. 2010, doi: 10.1134/S2075113311050108.

[109] C. Reuterskiöld Hedlund, J. Martins De Pina, A. Kalapala, Z. Liu, W. Zhou, and M. Hammar, "Buried InP/Airhole Photonic-Crystal Surface-Emitting Lasers," *Phys. Status Solidi Appl. Mater. Sci.*, 2020, doi: 10.1002/pssa.202000416.

Appendix A

Table A.1 A list of indium droplet samples (on planar substrate)

Sample no.	Temp. (°C)	TMIn supply time (s)	TMIn flow (SCCM)	GRI (s)
JR136	430	35	20	30
JR137	380	35	20	30
JR138	350	35	20	30
JR141	300	35	20	30
JR146	350	30	20	30
JR148	350	40	20	30
JR151	325	35	20	30
JR152	350	45	20	30
JR158	350	35	65	30
JR159	350	35	110	30
JR346	350	5	20	30
JR347	350	10	20	30
JR348	350	20	20	30
JR350	350	25	20	30
JR352	350	22.5	20	30
JR353	350	35	20	60
JR354	350	35	20	90
JR355	350	35	10	30
JR358	350	21.5	20	30
JR359	350	20.8	20	30
JR360	350	22	20	30

Appendix B

Table B.1 A list of site-controlled droplet / QD samples on photolithography-defined patterned substrate

Sample No.	Hole depth (nm)	Buffer thickness (nm)	Growth rate (μm/h)	V/III ratio	Temp. (°C)	TMIn supply time (s)	TMIn flow (SCCM)
JR209	160	0	2.3	180	430	35	20
JR212	160	50	2.3	180	430	35	20
JR213	160	50	2.3	300	430	35	20
JR218	80	50	2.3	300	430	35	20
JR226 (ACID)	80	50	2.3	300	430	35	20
JR226 (NO ACID)	80	50	2.3	300	430	35	20
JR229	80	50	2.3	300	430	35	20
JR235	80	50	2.3	180	430	35	20
JR240	80	50	2.3	180	350	35	20
JR243	80	50	2.3	180	430->350	35	20
JR245	80	50	2.3	400	430	35	20
JR249	80	50	2.3	300	430	35	20

JR251		80	50	2.3	90	430	35	20

Table B.2 A list of site-controlled droplet / QD samples on EBL-defined patterned substrate

Sample No.	Droplet/dot	Buffer thickness (nm)	Growth rate (µm/h)	V/III ratio	Temp. (°C)	TMIn supply time (s)	TMIn flow (SCCM)	GRI (s)
JR266	Droplet	20	2.3	300	430	35	20	30
JR270	Droplet	20	2.3	300	350	35	20	30
JR279	Droplet	10	1.2	180	430	35	20	30
JR284	Droplet	10	0.6	180	430	35	20	30
JR308	Droplet	10	1.2	300	430	35	20	30
JR311	Droplet	3	1.2	300	430	35	20	30
JR340	Droplet	0	1.2	300	430	35	20	30
JR342 (HF)	Droplet	0	1.2	300	430	35	20	30
JR343	Dot	0	1.2	300	430	35	20	60
JR344	Dot	0	1.2	300	350	35	20	60
JR362	Droplet	0	1.2	300	350	35	20	30
JR363	Droplet	1	1.2	300	350	35	20	30
JR418	Dot	1	0.6	300	350	25	20	30
JR425	N/A	1	1.2	300	N/A	N/A	N/A	N/A

JR427	N/A	1	1.2	500	-	-	-	-
JR440	N/A	2	1.2	500	-	-	-	-
JR441	Droplets	2	1.2	500	350	25	20	30
JR441	Dots	2	1.2	500	350	25	20	60